MARMARA UNIVERSITY
INSTITUTE FOR GRADUATE STUDIES IN PURE AND APPLIED SCIENCES

DEVELOPMENT OF BIOCOMPATIBLE AND FLEXIBLE POLYMERS FOR DLP PROCESSING AND IMPROVEMENT OF MECHANICAL PROPERTIES

EMRAH UYSAL

Ph.D. THESIS

Department of Mechanical Engineering

Thesis Supervisor

Prof. Dr. Bülent EKİCİ

Thesis Co-Supervisor

Assoc. Prof. Dr. Mustafa ÇAKIR

ISTANBUL, 2021

MARMARA UNIVERSITY
INSTITUTE FOR GRADUATE STUDIES
IN PURE AND APPLIED SCIENCES

DEVELOPMENT OF BIOCOMPATIBLE AND FLEXIBLE POLYMERS FOR DLP PROCESSING AND IMPROVEMENT OF MECHANICAL PROPERTIES

EMRAH UYSAL

(724611701)

Ph.D. THESIS

Department of Mechanical Engineering

Thesis Supervisor

Prof. Dr. Bülent EKİCİ

Thesis Co-Supervisor

Assoc. Prof. Dr. Mustafa ÇAKIR

ISTANBUL, 2021

ACKNOWLEDGEMENTS

First, I would like to thank my advisor Prof. Dr. Bülent EKİCİ for his support and valuable guidance. Thank you for being always available when I have questions. He sometimes became like a friend beyond an advisor.

When I started this thesis study, I knew as much as a mechanical engineer knew mettalurgy and materials. Therefore, I had so many questions about polymer materials. I am very grateful to my co-advisor, Assoc. Prof. Dr. Mustafa ÇAKIR, for his endless support and his answers to my unending questions about the polymers part of this study.

My lovely wife, Fatma UYSAL and my dear son Uras Yiğit UYSAL, they always became my life source when I felt that my energy was exhausted in some moments to conduct this thesis study. Also, I would like to thank my father and mother Mustafa and Emine UYSAL for their unmatched support, my brother and wife Hüseyin and Melek UYSAL, and my dearest nephew Efe UYSAL for always making me feel their presence by my side. Finally, I am grateful to my wife's family who have always supported me, and to all my friends in Nallıhan who have always been there for me since my childhood.

I would like to thank Boran BERBEROĞLU for both his friendship and support about my thesis study from the beginning to the end. Also, I want to thank Emre KÜÇÜKİSLAMOĞLU, Hakan DİLBAZ and Sercan METİN for their friendship and support about design and manufacturing of SLA printer. Besides, I would thank Kerim ÖZBEYAZ and Ömer DUMLUPINAR for their guidance and supports at dissertation writing and submission process and other roommates at Marmara University Mechanical Engineering Department (room MC568) for their friendship. Finally I want to thank Assoc. Prof. Dr. Turgay KIVAK, Dr. Ümit AĞBULUT and other collogues from Düzce University.

I want to thank Prof. Dr. D. Serap KURUCA and Işık KORKUT and their teammates at İstanbul University for their support at the biocompatibility tests.

CONTENT

ACKNOWLEDGEMENTS ii

CONTENT iii

ABSTRACT vii

ÖZET viii

CLAIM OF ORIGINALITY ix

SYMBOLS x

ABBREVIATIONS xi

LIST OF FIGURES xvi

LIST OF TABLES xix

1 INTRODUCTION 1

1.1 Literature Review of Rapid Prototyping Methods 1

1.1.1 Stereolithography SLA and Digital Light Processing DLP 3

1.1.2 Polyjet 6

1.1.3 Fused deposition modeling (FDM) 7

1.1.4 Laminated object manufacturing (LOM) 8

1.1.5 Selective laser sintering (SLS) 9

1.1.6 Electron beam melting (EBM) 10

1.1.7 Laser engineered net shaping (LENS) 11

1.1.8 3DP 11

1.1.9 Prometal 12

1.2 Photoresins for Vat Polymerization (VP) 14

1.2.1 Background 14

1.2.2 Photoinitiators 16

1.2.3 Acrylate and methacrylate monomers 19

1.2.4 Elastomers 21
1.2.5 Photopolymer based composites 22
1.2.6 Biocompatible and photocurable polymer resins 25
2 MATERIALS AND METHODS 29
2.1 Review of Existing DLP Device 31
2.2 Design of the New DLP Printer 32
2.3 Manufacturing and Programming of the DLP Printer 34
2.3.1 Manufacturing process 34
2.3.2 Circuit board of the device 36
2.3.3 Configuration and programming 38
2.3.4 Printer software for computer controlling 39
2.4 Synthesizing of the Photocurable Resin 43
2.4.1 Identifying and supplying materials 43
2.4.2 Synthesizing the resin 44
2.5 Test Piece Printing and Revision of the Printer 44
2.5.1 Dimensional and surface control of the test specimens 46
2.6 Nanocomposite Production and Examination Process 47
2.6.1 Synthesizing graphene oxide and preparing UV curable resin 47
2.6.2 Surface modification of the graphene oxide nano particles 48
2.6.3 3D printing process 49
2.6.4 Mechanical and morphological investigations 50
2.7 Synthesizing and Testing of the Biocompatible and Flexible Photopolymer 51
2.7.1 Synthesizing of Krasol nn22 52
2.7.2 Synthesizing of Desmodure H 53
2.7.3 Synthesizing of AF-PDMS 53

2.7.4 DLP printing of the AF-PDMS test specimens 55
2.7.5 Mechanical tests of the AF-PDMS 55
2.7.6 Thermal test and FT-IR analysis of the AF-PDMS 55
2.8 Biocompatibilitiy Tests 56
2.8.1 MTT cytotoxicity assay 56
2.8.2 SEM protocol 57
3 RESULTS AND DISCUSSION 59
3.1 Dimensional and Surface Roughness Results of Test Specimens 59
3.2 Mechanical and Morphological Test Results of Nanocomposite 61
3.2.1 Tensile test results 62
3.2.2 Impact and hardness tests results 64
3.2.3 FT-IR analysis 66
3.2.4 SEM examinations 68
3.3 Results of the AF-PDMS 70
3.3.1 Tensile test results 70
3.3.2 Shore a hardness test results 74
3.3.3 Abrasion test results 74
3.3.4 Density measurements 75
3.3.5 Thermal characterizations 76
3.3.6 FT-IR analysis 77
3.4 Results of the Biocompatibility Test 78
3.4.1 Cytotoxicity test results 78
3.4.2 SEM examinations of the seeded cells 78
4 CONCLUSIONS AND RECOMMENDATIONS FOR FUTURE WORKS 85
4.1 Conclusions 85
4.2 Recommendations for future works 87

REFERENCES 89

APPENDICES 105

ABSTRACT

DEVELOPMENT OF BIOCOMPATIBLE AND FLEXIBLE POLYMERS FOR DLP PROCESSING AND IMPROVEMENT OF MECHANICAL PROPERTIES

This thesis aims to synthesize polymer-based resin that can be printed in our own SLA type 3D printer and to prepare the synthesized resin as flexible and biocompatible. For this purpose, the thesis is divided into three stages. First, the design and production of the SLA type 3D printer was made and its calibration was carried out. In the second stage, polymer resin components that will be printed on the printer and curable with UV light have been identified and synthesized. After experiments with the synthesized resin, nano composite production was made. Finally, the biocompatible and flexible resin was synthesized and the biocompatibility of the produced material was investigated.

A DLP projector was used as a UV light source at the production of the printer. Since the resin to be used is expensive and it is foreseen that it can be synthesized in low quantities, the printer was revised and reached its final form. BisGMA epoxy acrylate was chosen as the structure for the resin and HDDA was used as the reactive solvent. Long researches have been made for the photoinitiator, which is one of the most critical points of the thesis work and provides the curing of the resin, and it has been determined that Irgacure 819® is compatible with the UV source used. With the completion of resin curing studies, nano composite synthesis and production studies were started. Graphene oxide nano materials were added to the resin in significant wt%, samples were produced, and scientific publication were made by examining their mechanical and morphological properties.

For the production of biocompatible and flexible materials, 3 different trials were conducted in resin synthesis studies. The resin obtained in the last experiment was found to be suitable for production in the device and the samples were printed. After examining the mechanical and morphological properties, it was determined that they were flexible. Finally, biocompatibility studies were completed in İstanbul Faculty of Medicine, Department of Physiology at İstanbul University, and it was determined that the material produced is biocompatible.

Keywords: Photopolymerization, DLP, 3D printer, PDMS, Biocompatible polymers, Flexible polymers

ÖZET

DLP PROSESİ İÇİN BİYOUYUMLU VE ESNEK POLİMERLERİN GELİŞTİRİLMESİ VE MEKANİK ÖZELLİKLERİNİN İYİLEŞTİRİLMESİ

Bu tez çalışması kendi üretimimiz olan SLA tipi 3B yazıcıda üretimi yapılabilecek polimer bazlı reçinenin sentezlenmesini ve sentezlenen reçinenin esnek ve biyouyumlu hale getirilmesini amaçlar. Bu amaç doğrultusunda tez 3 aşamaya ayrılmaktadır. İlk olarak SLA tip 3B yazıcının tasarımı ve üretimi yapılmıştır ve kalibrasyonu gerçekleştirilmiştir. İkinci aşamada ise yazıcıda basılacak ve UV ışıkla kürleşebilecek polimer reçine bileşenlerinin tespit edilerek sentezi yapılmıştır. Sentezlenen reçine ile denemeler yapıldıktan sonra nano kompozit üretimi yapılmıştır. Son olarak ise biyouyumlu ve esnek yapıya sahip reçinenin sentezi yapılmış ve üretilen malzemenin biyouyumlulukları incelenmiştir.

Yazıcının üretiminde UV ışık kaynağı olarak DLP tipi projektör kullanılmıştır. Kullanılacak reçinenin pahalı olması ve düşük miktarlarda sentezlenebileceği öngörülerek yazıcı revize edilmiş ve son haline ulaşmıştır. Reçine için yapı olarak BisGma epoksi akrilat seçilmiştir ve reaktif çözücü olarak HDDA kullanılmıştır. Tez çalışmasının en kritik noktalarından biri olan ve reçinenin kürleşmesini sağlayan foto başlatıcı için uzun araştırmalar yapılmış ve sonunda Irgacure 819'un kullanılan UV kaynağına uyumlu olan başlatıcı olduğu tespit edilmiştir. Reçine kürleştirme çalışmalarının tamamlanması ile nano kompozit sentezi ve üretimi çalışmalarına başlanmıştır. Grafen oksit nano malzemeleri reçine içerisine belirli oranlarda eklenerek numuneler üretilmiş, mekanik ve morfolojik özellikleri incelenerek bilimsel yayın çalışması yapılmıştır.

Biyo uyumlu ve esnek malzeme üretimi için reçine sentezi çalışmalarında 3 farklı deneme yapılmıştır. Son denemede elde edilen reçine cihazda üretilmeye uygun olduğu görülmüştür ve numuneler üretilmiştir. Üretilen numunelerin mekanik ve morfolojik özellikleri incelendikten sonra esnek yapıda olduğu tespit edilmiştir. Son olarak ise biyo uyumluluk çalışmaları İstanbul Üniversitesi, İstanbul Tıp Fakültesi, Fizyoloji Anabilim Dalında tamamlanarak üretilen malzemenin biyouyumlu olduğu tespit edilmiştir.

Anahtar kelimeler: Fotopolimerleşme, DLP, 3B yazıcı, PDMS, Biyouyumlu polimerler, Esnek polimerler

CLAIM OF ORIGINALITY

In the in-depth literature review, many studies were found on both three-dimensional printers and the production of biocompatible materials. However, there are many studies on implant production via additive manufacturing method. It has been determined that mostly multiplied cell cultures are used as raw material for implants to replace soft tissue. In addition, by placing biodegradable scaffolds on the area to be implanted, cell proliferation and tissue formation have also been frequently applied.

Flexible implant production with photopolymer has not been found in the open literature. At this point, the thesis study aimed to produce flexible implants that will replace with soft tissue, with polymer-based raw materials and DLP type printer. The aim here is to produce the soft tissue implant much faster and cheaper than the existing methods. Accordingly, the thesis study was carried out in three stages. In the first stage, the design, components production, assembly, programming and calibration of the 3D printer, which works with the DLP type and VP principle, was carried out. The manufactured printer is a unique design that can be easily revised when needed. In the second stage, photopolymer was synthesized as suitable with DLP printer, and the prepared resin was also original and produced in our laboratory. At this stage, nanocomposite production was also made and the suitability of the device for scientific studies was confirmed and this study was published in the international SCI journal.

In the last, third stage, biocompatible and flexible samples were produced. The mechanical, thermal and morphological properties of the samples were examined and biocompatibility tests were carried out. It has been determined that the products, produced with the originally synthesized resin in our laboratory, can replace soft tissue with their biocompatible and flexible structures. By changing the mixing ratios in its content, it is possible to produce samples with the desired flexibility depending on the characteristics of the region to be applied.

SYMBOLS

Cd	: Curing depth
Dp	: Penetration depth
Ɛ	: Strain
ζ	: Molar extinction coefficient
E_c	: Critical exposure
E_0	: Exposure dose on the surface
E_x	: Excess energy
I	: Photoinitiator concentration
$n \rightarrow \pi^*$	: The absorption with a longer wavelength
r	: Stoichiometric ratio
R_a	: Average roughness
R_z	: Maximum roughness depth
σ	: Stress
Wt%	: Percentage of the weight

ABBREVIATIONS

3D : Three Dimensional

3DP : Three Dimensional Printing

3T3 : 3-day transfer, inoculum 3×10^5 cells

ABS : Acrylonitrile butadiene styrene

AF-PDMS : Acrylate Functional Polydimethyl siloxane

AM : Additive Manufacturing

ANSI : American National Standart Institute

ASTM : American Society for Testing and Materials

ATCC : American Type Culture Collection

AUD **:** Aliphatic urethane diacrylate

BAPO : Phenylbis (2,4,6 trimethyl benzoyl) phosphine oxide

BASF : Badische Anilin- & Soda-Fabrik

BHI : Bis (2-(methacryloyloxyethyl) itaconate

Bis-GMA : Bisphenol A glycerolate (1-glycerol/phenol) diacrylate

BPA : Bisphenol A

C : Carbon

C_2H_5OH : Ethanol

CAD : Computer Aided Design

CAE : Computer Aided Engineering

CH_2 : Methylene

CH_3 : Methyl

CLIP : Continuous Liquid Interface Production

CNC : Computer Numeric Control

CO : Carbon monoxide

CO_2 : Carbon dioxide

DCPDA : Dicyclopentadiene acrylate

DGEBA : Bisphenol A diglycidyl ether

DIN : German Institute for Standardization

DIW : Direct Ink Writing

DLP : Digital Light Processing

DMD : Digital Micromirror Device

DMEM : Dulbecco's modified Eagle medium

DPGDA : Dipropylene glycol diacrylate

DSC : Differantial Scanning Calorimetry

EAA : Epoxy aliphatic acrylate

EBM : Electron Beam Melting

ECO : Economic

EDTA : Ethylenediaminetetraacetic acid

EPV : Elastomeric polyurethane

FBS : Fetal bovine serum

FDM : Fused Deposition Modeling

FT-IR : Fourier-Transform Infrared Spectroscopy

G-code : Geometric Code

GO : Graphene Oxide

H_2SO_4 : Sulfuric acid

H_3PO_4 : Phosphoric acid

HCL : Hydrochloric acid

HDDA : Hexanediol diacrylate

HDTV : High Definiation Television

HEA : Hydroxyethyl acrylate

HEMA : Hydroxyethyl methacrylate

HIPS : High Impact Polystyrene

HT-PDMS : Hydroxyl terminated polydimethyl siloxane

$KMnO_4$: Potassium manganate

KW : Kilowatt

LCD : Liquid Crystal Display

LED : Light Emitting Diode

LENS : Laser Engineered Net Shaping

LOM : Laminated Object Manufacturing

MEHQ : Methyl Ethyl Hydroquinone

MEMO : 3-(methacryloyloxy) propyl trimethoxysilane

MIT : Massachussetts Institute of Technology

MJ : MultiJet

MPa : Megapascal

MPS : Marcapton-functionalized polysiloxane

MTT : 3-(4,5-dimethylthiazol-2-yl)-2,5-diphenyl tetrazolium bromide

NADH : Nicotinamide adenine dinucleotide

NADHP : Nicotinamide adenine dinucleotide phosphate

NTSC : National Television Standards Committee

NVP : N-vinylpyrnolidone

O : Oxygen

OH : Hydroxide

OYP : Teaching Staff Training Program

PA12 : Polyamide 12

PAL : Phase Alternate Line

PEEK : Polyether Ether Ketone

PC : Polycarbonate

PCL : Poly(D,L-lactide-co-ε-caprolactone

PDMS : Polydimethyl Siloxane

PEG : Poly(ethylene glycol)

PETA : Pentaerythriol tetraacrylate

PH :Power of hydrogen

PLA : Polyactic Asid

PLA-PUA : Polylactic acid-polyurethane oligomer

PPGIV : Poly(1, 3-propanediol-co-glyceryl) itaconate-co-vanillate

PPP : Photopolymer Printing

PPSF : Polyphensulfone

PVC : Polyvinyl Chloride

P-VIP : Professional Video Projection

RCA : Radio Corporation of America

RGB : Red, Green, Blue

RP : Rapid Prototyping

SCI : Science Citation Index

SECAM : Sequential Color and Memory

SEM : Scanning Electron Microscopy

Si : Silicon

SLA : Stereolithography

SLS : Selevtive Laser Sintering

STL : Standart Tessellation Language

Sur-Mod : Surface Modified

T-12 : Dibutyltindiluent

TAEI : Tris[2-[acryloyl)ethyl] isocyanurate

TEA : Triethylamine

TEGDMA : Triethylene glycol dimethacrylate

THC : Tris(2-(methacryloyloxyethyl) citrate

THF : Tetrahidrofuran

TPO : Diphenyl 2,4,6 trimethyl-benzoyl phosphine oxide

TTA : Triplet-triplet annihilation photon

TTMA : Propane trimethacrylate

UV : Ultraviolet

VP : Vat Polymerization

XGA : Extended Graphics Array

LIST OF FIGURES

Figure 1.1 Product development cycle [4]..... 2

Figure 1.2 Additive manufacturing processes [7]..... 3

Figure 1.3 Schemes of two types of stereolithography setups. Left: a bottom-up system with scanning laser. Right: a top-down setup with digital light projection (DLP) [8]..... 5

Figure 1.4 Schematic of a CLIP 'bottom-up' DLP device [10]. 5

Figure 1.5 Polyjet method with two inkjets [10]..... 6

Figure 1.6 Schematic demonstration of Fused Deposition Modeling (FDM) [10] 8

Figure 1.7 Illustration of Laminated Object Manufacturing (LOM) [22] 9

Figure 1.8 Schematic illustration of Selective Laser Sintering (SLS) [10] 10

Figure 1.9 Principle of Laser Engineered Net Shaping (LENS) [31]..... 11

Figure 1.10 Photocleavage of Darocur 1173 17

Figure 1.11 Radical photoinitiators of Type I that commonly cited in stereolithography studies. 17

Figure 1.12 Radical reaction of Type II photoinitiators [15]..... 18

Figure 1.13 Acrylate and methacrylate monomers for rapid prototyping [15]..... 20

Figure 1.14 Approximate elastic modulus (Young's modulus) of selected engineering and biocompatible materials [106]. 27

Figure 2.1 Flow chart of the method in the thesis 30

Figure 2.2 Existing DLP printer 32

Figure 2.3 New design of the DLP printer 33

Figure 2.4 Printer manufactured within the scope of the thesis 36

Figure 2.5 Arduino Mega board system integrated with Ramps 1.4..... 37

Figure 2.6 Arduino 0023 software..... 38

Figure 2.7 Configuration of the arduino..... 39

Figure 2.8 Demonstration of the 3D view menu 40

Figure 2.9 Demonstration of the slice view menü 40

Figure 2.10 Demonstration of the GCode view option 41

Figure 2.11 Demonstration of the control menu 41

Figure 2.12 Demonstration of the configure machine option 42

Figure 2.13 Demonstration of the configure slicing profile option 42

Figure 2.14 Molecular formula of the Bis-GMA (Cas no 4687-94-9) 44

Figure 2.15 Molecular formula of HDDA (Cas no 13048-33-4) 44

Figure 2.16 Molecular formula of IRGACURE 819 (Cas no 162881-26-7) 44

Figure 2.17 Revised DLP printer 46

Figure 2.18 Flow chart of graphene oxide synthesizing via Tour method 48

Figure 2.19 Schematic view of surface modification for GO 49

Figure 2.20 Printed tensile and impact tests specimens 50

Figure 2.21 Tensile test specimen dimensions (ASTM D638-02a type-IV) 51

Figure 2.22 Synthesizing reactions of Krasol nn22 52

Figure 2.23 Synthesizing reactions of Desmodure H. 53

Figure 2.24 Synthesizing reactions of AF-PDMS 54

Figure 2.25 Prepared samples for cytotoxicity measurement 57

Figure 2.26 The process of seeding cells on samples for SEM images 58

Figure 3.1 Dimensions of the tensile specimens after production 60

Figure 3.2 Roughness measurement results from the lateral surfaces of impact samples 61

Figure 3.3 The result of the roughness measurement obtained from the upper surface 61

Figure 3.4 Comparison of the tensile test results for surface modified and non-modified GO 63

Figure 3.5 Izod impact test results for non-modified and surface modified GO. 65

Figure 3.6 Shore D hardness test results for non-modified and surface-modified GO . 66

Figure 3.7 Non-modified graphene oxide 67

Figure 3.8 Surface modified graphene oxide 67

Figure 3.9 FT-IR spectrums of the cured polymers 68

Figure 3.10 SEM images of fracture surfaces for surface modified GO contained nano composites (a) 1000X zoomed images of 0.05% sur-mod GO contained samples (b) 5000X zoomed images of 0.05% sur-mod contained samples (c) 1000X zoomed images of 0.15% sur-mod GO contained 69

Figure 3.11 Demonstration of grain distributions (a) and size (b) of graphene oxide nano particles with SEM shots. 70

Figure 3.12 Results of the maximum stress vs AF-PDMS content 71

Figure 3.13 Results of the maximum strain vs AF-PDMS content 72

Figure 3.14 Results of the Young's Modulus vs AF-PDMS content 73

Figure 3.15 Results demonstration on approximate elastic modulus (Young's modulus) of selected engineering and biocompatible materials 73

Figure 3.16 Results of the Shore A hardness test 74

Figure 3.17 Results of the abrasion test 75

Figure 3.18 Results of the density measurements 76

Figure 3.19 Results of the DSC test 77

Figure 3.20 FT-IR spectroscopy for AF-PDMS vs Tegomer® RC-1002 77

Figure 3.22 Cytotoxicity test results 78

Figure 3.23 SEM images of cell seeded samples: Pure BisGMA 79

Figure 3.24 SEM images of cell seeded samples: 20 wt% AF-PDMS content 80

Figure 3.25 SEM images of cell seeded samples: 40 wt% AF-PDMS content 81

Figure 3.26 SEM images of cell seeded samples: 60 wt% AF-PDMS content 82

Figure 3.27 SEM images of cell seeded samples: 80 wt% AF-PDMS content 83

Figure 3.28 SEM images of cell seeded samples: Pure AF-PDMS 84

LIST OF TABLES

Table 1.1 Categorized rapid prototyping techniques for polymer materials with advantages and disadvantages [15]..... 13

Table 1.2 Polymer composites printed via DLP process for mechanical applications.. 24

Table 2.1 Properties of DLP projection device..... 35

Table 3.1 The results of the tensile test..... 64

1 INTRODUCTION

Although it took time for the additive manufacturing method to become widespread after its discovery, it has become a technology that enters the houses today. The method, which can be used in every sector where manufacturing is required, has recently been tried in many areas from implant, home and car construction to the food sector. It is a method that free-form fabrication of models from CAD data and reflects the imagination to production in a single process. It allows many materials, especially polymers, to be used as raw materials. Additive manufacturing, which has methods that we can gather under three major headings, continues to be the most popular production method of the last period with the discoveries made every day. The major methods are; Fused Deposition Modeling (FDM), Stereolithograpy (SLA) and Selective Laser Sintering (SLS).

1.1 Literature Review of Rapid Prototyping Methods

The rapid prototyping method, which was developed in the 1980s to produce models and prototype parts, was invented to facilitate engineers and designers to produce what they had in mind. It is also used for the printing of final parts in addition to the production of models and prototypes. The concept of 3D printing was first discovered by Chuck Hull in 1984 when he was working on curing desktop coatings with ultraviolet (UV) light [1]. In 1986, Hull established the 3D Systems company and produced the first rapid prototyping machine, which he called stereolithography (SLA). Scott Crump developed the Fused Deposition Modeling (FDM) device in 1988 and commercialized it with Stratasys in 1990 [2]. Objet Geometries, which invented Photopolymer Printing (PPP) in 1998, developed Polyjet [3]. Now there are many different companies with dozens of different prototyping techniques available, including these technologies. Ordinary printers used to print on paper work on the right-to-left x-axis and bottom-up y-axis. In addition to 3D printers, a bottom-to-top z-axis has been added. Among the biggest advantages of the technique, compared to classical production methods, are the savings in time and cost, the contribution to the product development cycle thanks to the increase in the interaction of the designers, the printing of almost any design that can be very difficult to produce [4]. However, it has not fully taken its place in the production sector today. On the other hand, it has started to be used frequently by scientists, medical

doctors, designers, jewelers, students, academics and artists [5, 6]. Thanks to rapid prototyping, researchers can easily and quickly create models to put theory into practice, and medical practitioners can improve diagnosis and procedure by creating a model of the area requiring treatment. Jewelers make molds for their products. Artists and designers make it easier for them to improve their creativity by using this method.

Product development steps with rapid prototyping are given in Figure 1.1. As can be seen, thanks to the method, the model can be created faster and the number of tests can be increased thanks to the production of more models. Rapid prototyping technologies are no longer just used to create models. It is possible to manufacture final products with the advantage of plastic materials [5]. Although the method has other names nowadays, such as 3D printing, they are all based on rapid prototyping [2-6].

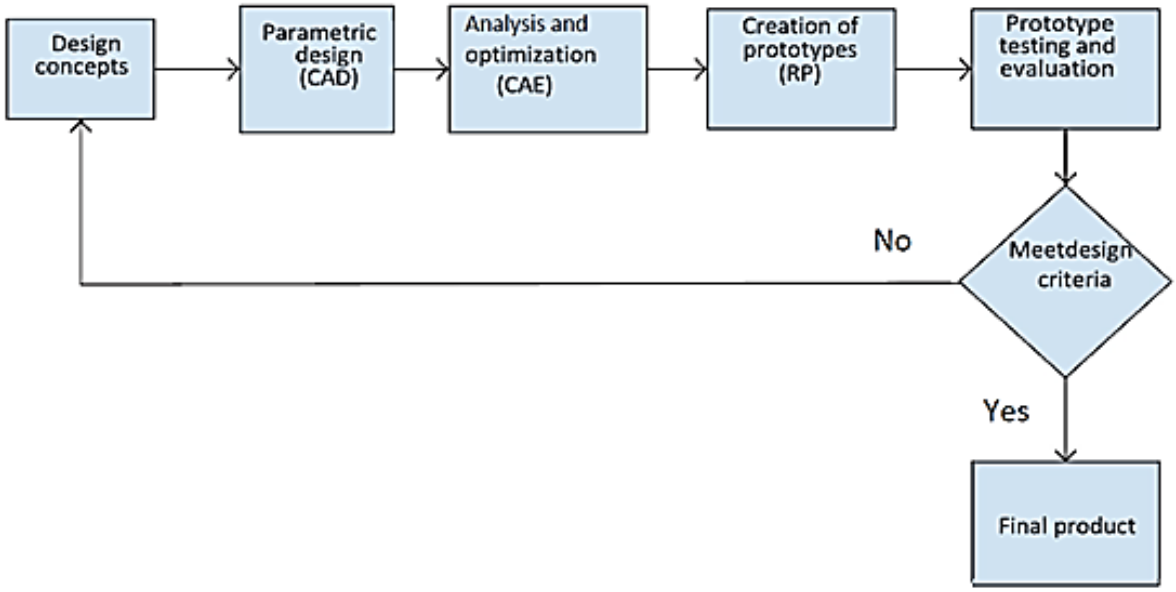


Figure 1.1 Product development cycle [4].

In the criteria used in the diagram given in Figure 1.2, these processes are classified as solid based, liquid-based and powder-based [7]. The processes considered are stereolithography (SLA), polyjet, fused deposition modeling (FDM), laminated object manufacturing (LOM), prometal, 3D printing (3DP), electron beam melting (EBM), laminated engineered net shaping (LENS), and selective laser sintering (SLS). Liquid and powder-based methods are preferred more frequently than solid-based processes such as LOM in current uses, and it is anticipated that they will be developed more in the future.

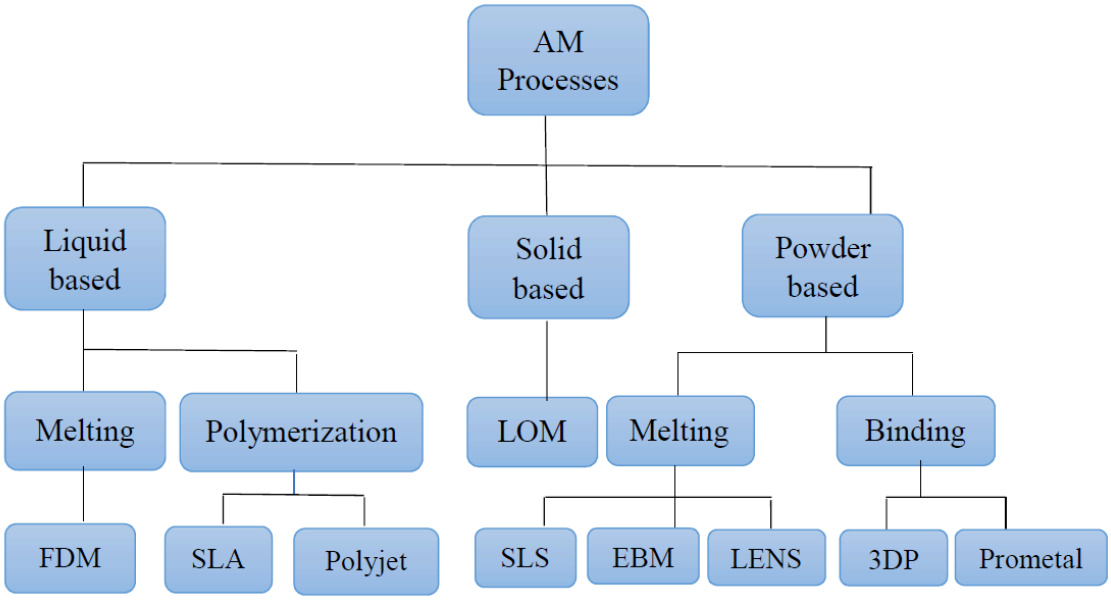


Figure 1.2 Additive manufacturing processes [7].

1.1.1 Stereolithography SLA and Digital Light Processing DLP

Developed by 3d systems Inc, SLA (also known as Vat Polymerization VP) is one of the first and most widely used methods of rapid prototyping, so the two methods are used synonymously. The process is liquid based. The liquid resin starts to cure by contacting with ultraviolet (UV) light and the scanned area solidifies. The method starts with the creation of the model in CAD software. Then the model file is converted to Standard Tessellation Language (.stl) format using the same software. Before the model is sent to the device, settings such as layer thicknesses, curing time and lifting distances are made through the software used in prototyping. After the file is sent to the device, the UV source scans the geometry to be cured onto the resin surface and solidification occurs. When the layer is completed, the platform goes down, takes resin on it for the next layer, and is scanned with UV again and merges with the previous layer. Prototyping is completed by repeating this process until all layers are completed and the model is created. In another method, the production direction is top-down and digital light processing (DLP) projection is used as the UV light source. The remaining operations are the same as the bottom-up method with laser scanner [8]. Top-down version is used in this thesis study with DLP light source. As a more recent version of the method, the microstereolithography process was developed. The layer thickness of this process can go down to 10 µm [9]. In the SLA method, the resolution of the z-axis is determined by

the depth of curing, photoinitiator properties, exposure conditions (wavelength, power and time) and substances such as paint, pigment and nanomaterials used in the resin [10]. In addition, the use of UV absorber ensures the curing of transparent materials. The photo-induced layer thickness varies between approximately 50-200 μm. Layer thicknesses are determined by the balance between curing time and resolution. With microSLA and a UV laser source, resolution of about 5 μm in the x/y plane and 10 μm in the z axis can be achieved [11].

Like SLA, DLP (Digital Light Processing) selectively crosslinks photoresin layers via UV light to create patterns (Figure 1.3). Differently, each layer is revealed in a single operation, thanks to a masked light source, instead of being scanned point by point [12]. The method is very similar to conventional lithography and is also called dynamic mask lithography The geometry of each layer is projected onto the resin surface in black and white. Overhead projectors and digital micromirror devices use such dual models [13, 14]. Since layer scanning is performed by projecting a single image, the production process is faster compared to the SLA method. For the same reason, whether the layer surface is too wide or too narrow, it does not affect the production time. Thus, cm/h, that is, the layer height reached per unit time, represents the speed of the DLP process. In addition, since the resin layer polymerized in the DLP process is located at the bottom of the chamber and does not come into direct contact with air, it is less affected by oxygen inhibition compared to SLA [15]. The light sources used have rapidly evolved from conventional lamps to modern diodes (LEDs) with a wavelength ranging from deep UV to visible. The horizontal resolution of the DLP system is usually in the range of 10-50 μm, depending on the optics used to project the patterns onto the resin and the number of pixels provided by the DMD. The vertical resolution, represented by the thinnest layer thickness that can be formed, depends on the photoinitiator properties and the curing height achieved by the depth of effect of light [15]. Vertical resolution can also be adjusted with light absorbing additives such as nephthol-based paints, which also prevent fringes and distortions that may occur due to refraction and scattering in light. Apart from pure photopolymers, metal-added and ceramic-added polymer mixtures can also be cured by the DLP method. [16]. In particle additive mixtures, metal and ceramic materials do not react as they are not sensitive to light, while polymer resin photo cures and becomes a binder.

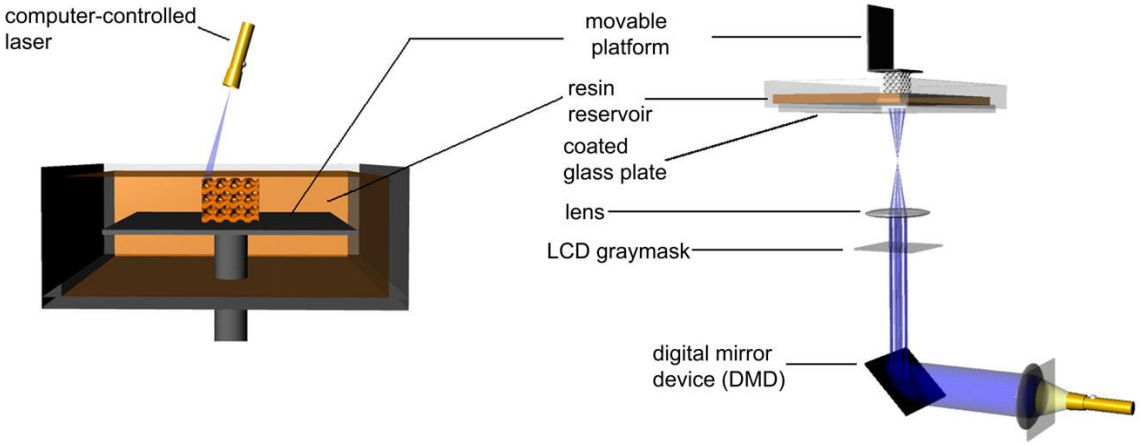


Figure 1.3 Schemes of two types of stereolithography setups. Left: a bottom-up system with scanning laser. Right: a top-down setup with digital light projection (DLP) [8]

In the uv-based new generation method called CLIP, it creates a controlled oxygen-inhibited dead zone and performed continuous curing from bottom to top Figure 1.4. While UV light is sent to the whole area, curing is prevented by the oxygen sent between the beam and the resin, and only the desired geometry is printed. The advantage over the classical SLA-DLP method is that it saves a lot of time as a continuous print is created.

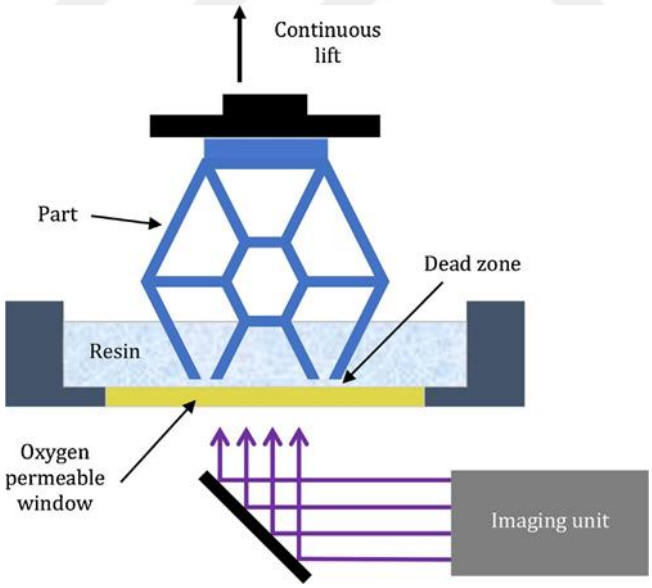


Figure 1.4 Schematic of a CLIP 'bottom-up' DLP device [10].

In the SLA and DLP methods, fast curing acrylate monomers are preferred instead of similar methacrylates due to viscosity limitations, and this creates limits on mechanical strength values. Methacrylates provide better biocompatibility in addition to higher

strength than acrylate polymers. However, each layer is connected to the previous layer with photopolymerization, resulting in good strength and minimum anisotropy in parts produced with SLA and DLP.

1.1.2 Polyjet

The method uses inkjet technology to produce a three-dimensional model. The inkjet head spreads the layer of the model on the table by spraying photopolymer with movement in the x and y axes. Then, by irradiating with UV light, the emitted polymer is cured and the layer is completed. The production is completed by combining the layers with repeated processes. With this method, a layer thickness of 16 µm can be obtained and thus high resolution part production can be achieved. However, parts produced by this method have lower strength compared to SLA. A polymer as gel-type is used for support in the production of parts with protruding geometries in the process, and these supports are cleaned with a water jet after the process is finished. It is possible to produce parts with multiple colors using Polyjet [17, 18]. Polyjet method is demonstrated at Figure 1.5.

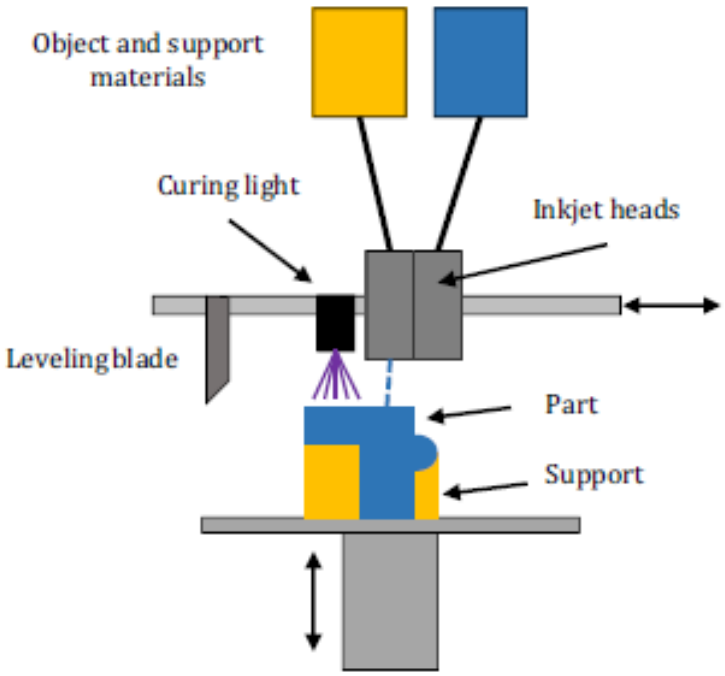


Figure 1.5 Polyjet method with two inkjets [10]

1.1.3 Fused deposition modeling (FDM)

Fused Deposition Modeling (FDM) is a method in which the head fed with a thin polymer filament melts the polymer at a diameter of around 0.25-0.50 mm and extrudes it. The model is created by adding the extruded polymer layer by layer. The materials used in the process are acrylonitrile butadiene styrene (ABS), polycarbonate (PC), polyphensulfone (PPSF), PC-ABS combination and a medical grade material as PC-ISO. The main advantages of this method can be given as no need for resin curing, no need for a final chemical treatment, and lower cost of equipment and manufactured parts [5, 6, 19, 20]. The disadvantage is that due to the low resolution in the z-axis, it requires post-processing of the parts for which smooth surface is desired. It is also a slow process, large and complex structures can take days to print. To save time, some models have two modes. These are the full intensive mode and the infrequent mode, which saves time but clearly degrades the mechanical properties [21]. This method, which is used for hobby purposes at home, is often preferred by designers. In recent years, large structures such as houses and cars have been produced with the help of gigantic printers. The schematic representation of the FDM method is given in Figure 1.6.

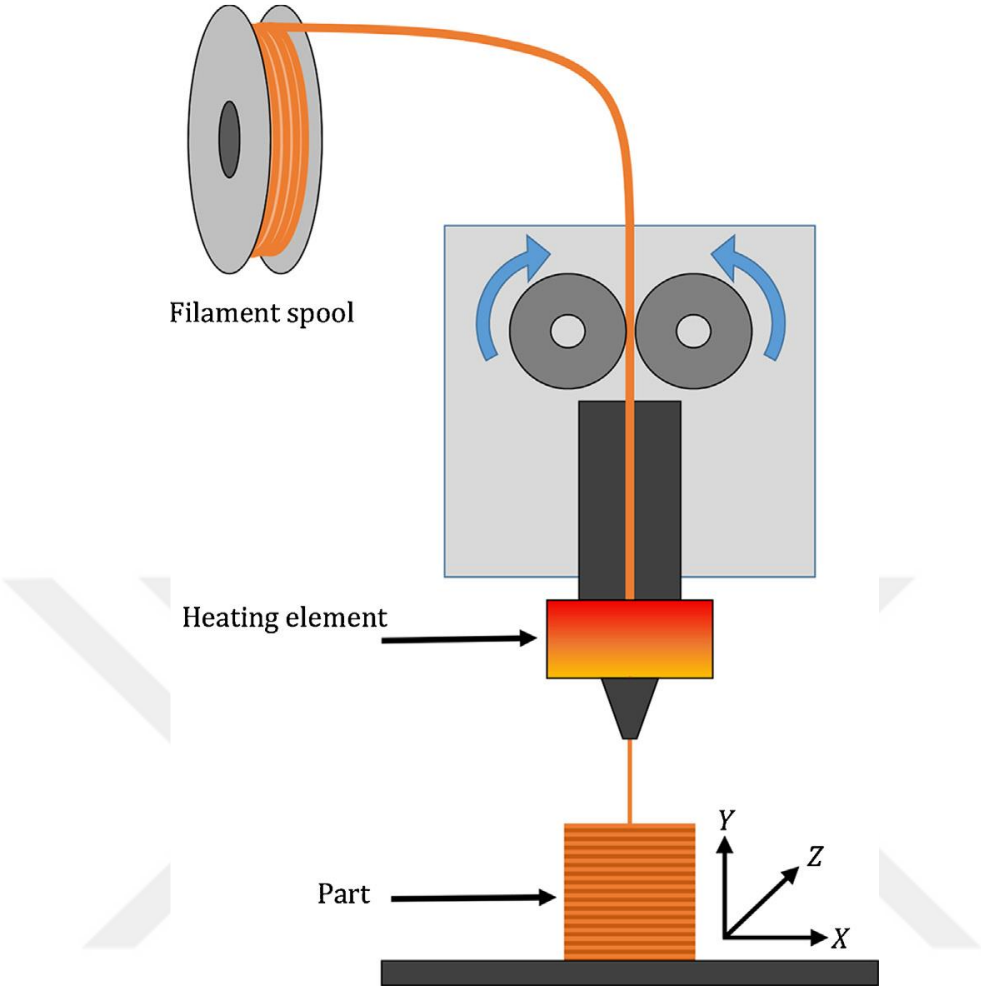


Figure 1.6 Schematic demonstration of Fused Deposition Modeling (FDM) [10]

1.1.4 Laminated object manufacturing (LOM)

Laminated Object Manufacturing (LOM) is a method that combines addition and subtraction to create layers. In this process, sheet form material comes to the device. The layers are joined using a thermal adhesive coating in addition to pressure and temperature. Using the data of the .stl file obtained from the CAD program, the carbon dioxide laser cuts each layer according to the desired geometry. The advantages of this method are no need for additional processing and support structure, no deformation and phase change at the process, low cost and large parts can be produced. The disadvantages are that after the sheet materials are cut, waste pieces are formed, the surface quality is low, the machinability and mechanical properties of the material depend on the production direction, and the production of complex internal cavities are very difficult [3]. Schematic demonstration of the LOM process is given in Figure 1.7.

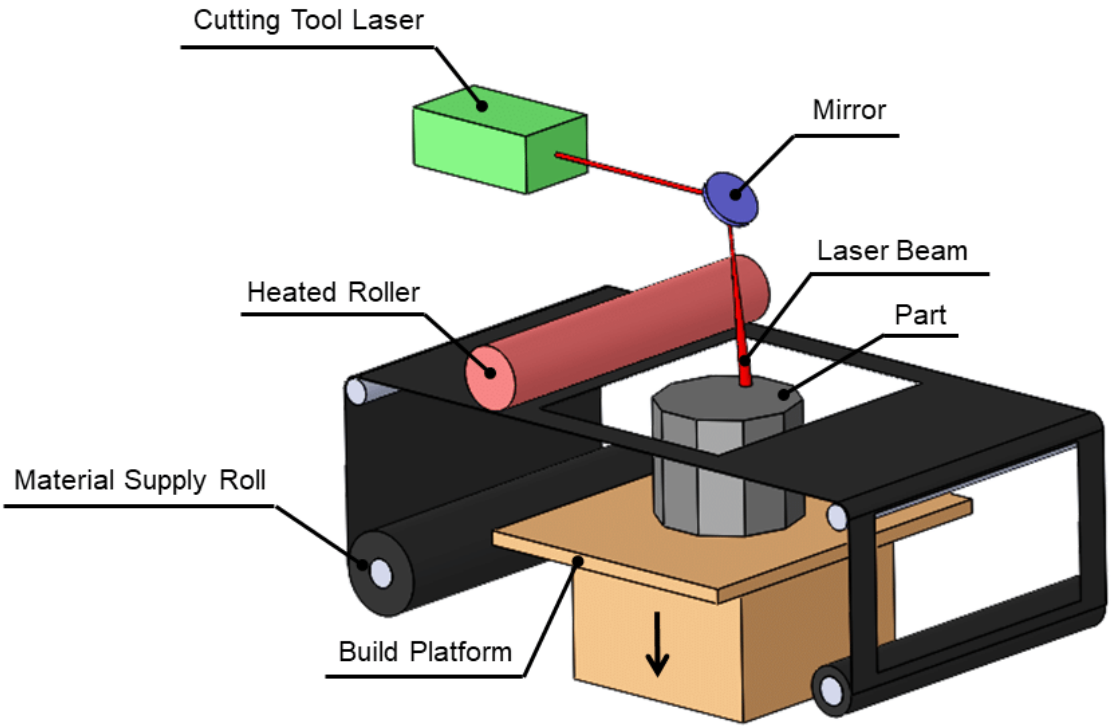


Figure 1.7 Illustration of Laminated Object Manufacturing (LOM) [22]

1.1.5 Selective laser sintering (SLS)

In the Selective Laser Sintering (SLS) method, which was introduced shortly after the SLA method, only semi-crystalline, particulate thermoplastic polymers were used as construction material at the beginning. The technique carries out production using a dual energy source. First, the powder bed is heated to a value above the recrystallization temperature of the material before the sintering process. The pre-heating process is carried out to prevent deterioration caused by large thermal differences that occur with high temperatures coming from the laser head during sintering [10]. The heated particles are spread on the platform to be treated with the help of a roller as much as the layer thickness. The carbon dioxide laser head combines the powder in the scanned regions by sintering according to the geometry sent with the CAD data. With this repetitive process, the layers are combined and the model is created (Figure 1.8). This process allows for a wide variety of materials. These are plastics, metals, metal combinations, metal and polymer combinations, metal and ceramic combinations etc [9, 23, 24]. Some kind of binder is necessary for metals. These may be a polymer binder removed by post-production heating, or a mixture of metal binders with different melting temperatures [25]. The main

advantages of the method are that it allows the use of a wide range of materials and that the unused powder can be recycled after production. The disadvantages are that the accuracy of the model depends on the size of the material particles, since the process occurs over the melting temperature, the material must be protected from oxidation by using an inert gas atmosphere.

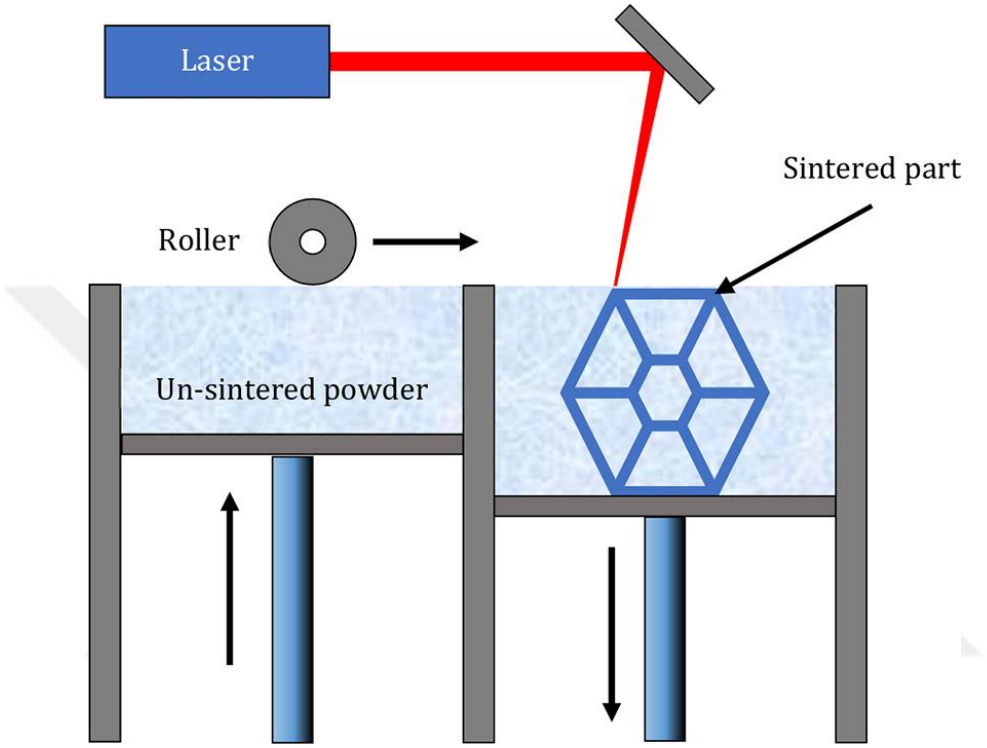


Figure 1.8 Schematic illustration of Selective Laser Sintering (SLS) [10]

1.1.6 Electron beam melting (EBM)

Electron Beam Melting (EBM) is similar in principle to SLS. Although this process is relatively new, it is rapidly spreading. Differently, a high voltage electron laser beam operating between 30-60 KV is used to melt the powder. The method developed to produce metal parts is carried out in a high vacuum chamber to prevent oxidation. EBM can also process many types of prealloyed metals. One of the planned future uses of this process is being able to manufacture in outer space, as it is operated in a vacuum chamber [26, 27].

1.1.7 Laser engineered net shaping (LENS)

In this 3D manufacturing process, the part is produced by melting the metal powder injected into a specific location with a high-power laser beam. Solidification occurs after the model has cooled. The process is carried out in a vacuum chamber under an argon atmosphere. The method allows the use of many metals and their combinations, such as stainless steel, nickel-based alloys, titanium alloys, tool steel, copper alloys. Besides it is used for repairing parts that are impossible or expensive for other methods. One of the problems in this process is that in the repair of parts that require high precision, such as turbine blades, it can cause residual stresses due to uneven heating and cooling [9, 20, 28–30]. Figure 1.9 shows the production of parts by the LENS method.

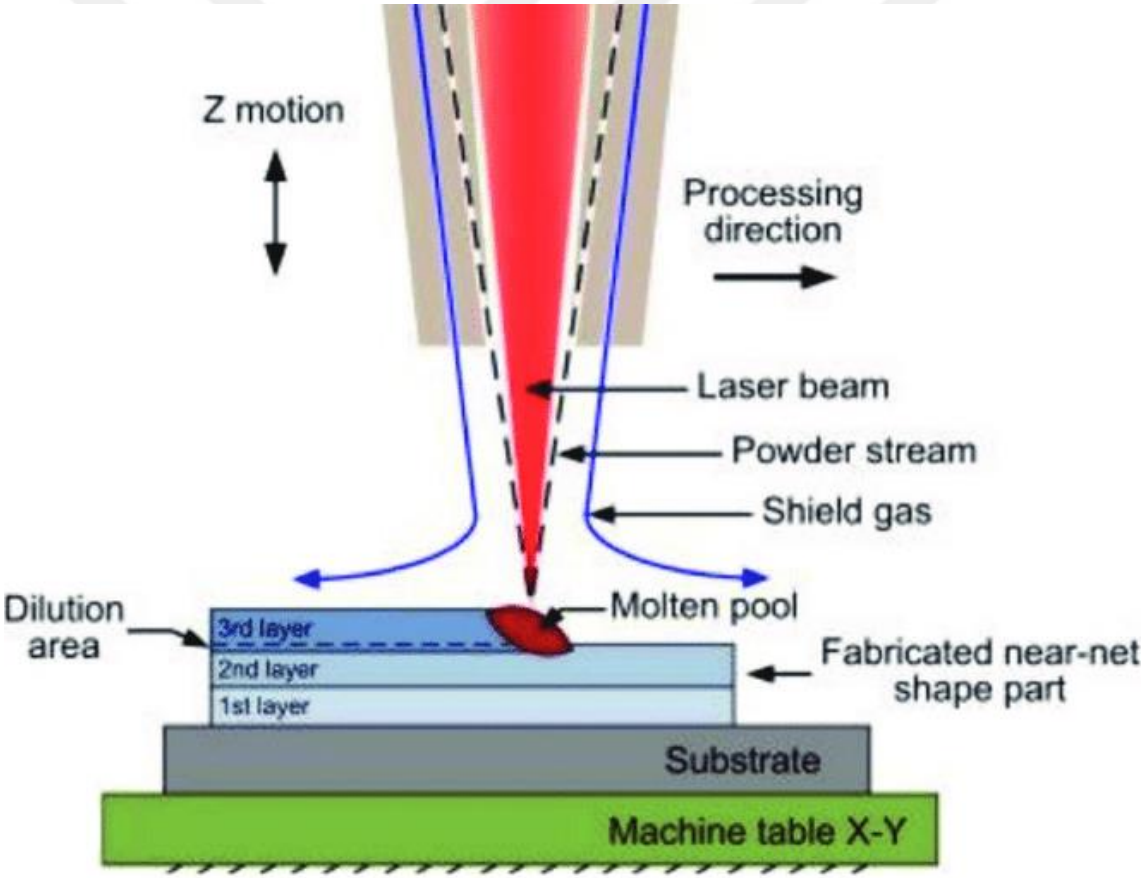


Figure 1.9 Principle of Laser Engineered Net Shaping (LENS) [31]

1.1.8 3DP

The 3DP method is an MIT-licensed process in which a water-based liquid binder is supplied with a jet onto a starch-based powder to print the part. The powder particles lie

in a powder bed and they are glued together when the binder is jetted. This process is named 3DP because of its similarity with the inkjet method used to print in two-dimensions on paper. 3DP can handle a high variety of polymers [9, 20].

1.1.9 Prometal

Prometal is a three-dimensional printing process used to produce injection tools and molds. It is a powder-based process using stainless steel. The printing process occurs by spraying a liquid binder on the steel powder through jets. The powder is located in a powder bed that is controlled by build pistons that lowers the bed when each layer is finished and a feed piston that supply the material for each layer. At the end of the process, the remaining dust must be removed. Mold production does not require post-processing. If a functional part is being produced, additional processes such as sintering, penetration and finishing are required [7, 20]. In the sintering process, the part is heated at 350 ^{0}F for 24 hours in order to harden the binder that combines with the 60% porous steel. In the infiltration process, the part is infused with 60% stainless steel and 40% bronze alloy by heating it to over 2000 ^{0}F [32]. The same process, but with different sintering temperatures and times, has been used with other materials, such as a tungsten carbide powder sintered with a zirconium copper alloy for the manufacture of rocket nozzles; these parts have better properties than CNC machined parts of the same material.

Table 1.1 Categorized rapid prototyping techniques for polymer materials with advantages and disadvantages [15].

Categorized techniques	***Typical and largest build volume***	***Typical feature resolution***	***Typical materials***	***Advantages***	***disadvantages***
Vat polymerization exposure from top (Prodways)	250x250x250mm^3 800x330x400 mm^3 (Prodways)	50-100 µm	Acrylates/epoxides	Exellent surface quality and precision	Limited mechanical properties
CLIP exposure from bottom	150x80x300 mm^3 100x100x100 mm^3 300x300x300 mm^3 (DigitalWax 30X)	75 µm 25-100 µm	Acrylates Acrylates/epoxides	High build speed Low initial vat colume Better surface quality	Low-viscosity resins required Limitied mechanical properties
Multiphoton lithography	5x5x1 mm^3 100x100x3 mm^3	0.1-5 µm	Acrylates	Very high resolution	Low build speed Limited materials
Powder Bed Fusion polymer SLS	250x250x250 mm3 1400x1400x500 mm3 (Huake 3D HKS1400)	50-100 µm	PA12-PEEK	Best mechanical properties Less anisotropy	Rough surfaces Poor reusability of unsintered powder
Material and Binder Jetting polyjet	300x200x150 mm3 1000x800x500 mm3	25 µm	Acrylates	Fast Allows multimaterilas AM	Low viskosity ink required
Aerosol jet printing	200x300x200 mm3 (Aerosol Jet 5X)	10 µm	Conductive inks/dielectrics	High resolution Low temprature process	Low viskosity ink required
3D printing (binder jetting)	200x250x200 mm3	100 µm	Starch PLA Ceramics	Fast Allows multimaterials AM Low temprature	Limited strength of parts Rough surfaces
Sheet Lamination laminated object manufacturing	170x220x145 mm3	200-300 µm	PVC Paper	Compact desktop 3D printer	Limited materials Low resolution High anisotropy
Material Extrusion FDM	200x200x200 mm3 1005x1005x1005 mm3 (BigRep One)	100-150 µm	ABS, PLA, PC, HIPS	Inexpensive machines and materials	Rough surfaces High temprature process
3D dispensing	150x150x140 mm3	100 µm to 1 cm	Thermo-plastics, composites, photoresins, hydrogels, biomaterials	Broad range of materials	Rough surfaces Narrow viscosity process window

1.2 Photoresins for Vat Polymerization (VP)

In the VP technique, polymer-based resins in liquid form with low viscosity are used as raw materials. Although the content of the resins may differ according to the intended use, their common feature should be photocurable. This means that it can solidify by reacting with the UV light provided by the laser or DLP source. Many types of resins such as biocompatible, rigid, high strength, flexible and composite are used for production by VP method. In this cheapter, the structures, types and usage areas of photocurable resins are examined.

1.2.1 Background

Photosensitive resins, which are activated by irradiation and form cross-linked chemicals and thus undergo solidification that cannot be re-dissolved, are mostly used in Vat Polymerization (VP) and MultiJet (MJ) techniques. They usually contain photoinitiators, monomers, oligomers and additives (such as absorbent, sensitizer, solvent, dye). Single-photon photopolymerization (SLA, DLP) can occur via a free radical or ionic (usually cationic) reaction. The way in which the reaction will occur is determined by the reactive species of the photoinitiator used [33]. Monomers are single-chain small molecules and have one or more functional groups that determine the curing rate, crosslink density, and properties of the produced part (such as mechanical and morphological). Since monomers are acrylate-based, they are widely used with their high reactivity and generally have a vinyl functional group for free radical photopolymerization [34, 35]. Urethane acrylate, bisphenol A (BPA) acrylate and poly(ethylene glycol)(PEG) acrylate are examples of vinyl monomers that enter into free radical polymerization. The most commonly used for cationic photopolymerization are epoxy monomers and vinyl ether functional groups. Cycloaliphatic epoxides are widely used in today's industry and have the fastest polymerization rate among epoxides [36]. Oligomers are also known as prepolymers and form the main body of polymer chains. Because they are larger molecules with bulkier groups, they are much more viscous and have higher functionality than monomers. With this functionality, in addition to crosslink density and curing speed, they also greatly affect final product properties such as toughness, strength, surface quality [33]. Since each oligomer can provide different properties, combinations are generally used.

Additives are used to increase the efficiency and performance of the resin. Inhibitors and retarders are used to control the depth of penetration and curing time, as well as to prevent the negative effects of reflected light. Generally used inhibitors and retardants are sterically hindered phenols, quinones and oxygens [37]. Sensitizers used to induce the formation of active products from photoinitiators are chemicals that can absorb radiation of wavelength well. Solvents, which act as diluents to control the viscosity of the resin, also help transfer the heat resulting from polymerization.

The first photocurable polymers used for VP were originally designed for a different purpose. He cited an earlier patent for details using a resin from Lactite in Hull's 1984 patent, where he first described SLA [1, 38]. The resin, which was made to produce a UV-curable adhesive, consisted of urethane dimethacrylate containing a small part of acrylic acid, benzophenone as a photoinitiator, and methyl ethyl hydroquinone (MEHQ)/trialyl phosphate used to prevent premature polymerization. Hull used a 350 W mercury short arc lamp focused through a 1 mm fiber optic beam, which emits 1 W/cm^2 of radiation onto the curing surface. In subsequent patents, the He-Cd laser became the main light source for SLA, which is significantly more efficient on resins that absorb light at only 325 nm [39]. To support the rapid prototyping method, formulators are trying to synthesize resins that require lower doses of energy to achieve gelation, in order to print faster. For SLA, the critical exposure Ec value, measured in mJ/cm2 and enabling gelation, can be defined as follows;

$$E_c = E_0 \exp\left(-\frac{C_d}{D_p}\right) \tag{1.1}$$

Here, E_0 represents the dose on the surface, C_d represents the curing depth and D_p, which is defined below, represents the penetration depth.

$$D_p = 1/(2.3\varepsilon[I]) \tag{1.2}$$

This equation assumes that the absorption of light at the wavelength used depends only on the photoinitiator concentration [I] and the molar extinction coefficient [ε] [40].

While E_c is an important value, its strength and modulus in the polymer gel state are too low to withstand construction and development processes [41]. Flory's equation predicts that gelation occurs at lower conversions as the functionality of the monomer increases; such as 33% for diacrylate, 20% for triacrylate and 14% for tetraacrylate [42]. To

compensate, Jacobs identified the excess energy (Ex) required to crosslink the polymer to a degree that would provide sufficient green strength. "Green" here refers to the initial photopolymerized curing, as opposed to post-production additional thermal curing so commonly used in AM.

$$E_x = E_c(D_p/C_d)\left(\exp\left(\frac{C_d}{D_p} - 1\right) - 1\right) \quad (1.3)$$

Excess energy is directly proportional to the critical exposure and inversely proportional to the cure depth. This means that by increasing the energy dosage or reducing the curing depth, green strength can be increased. UV and visible absorbers can be added to improve solubility and increase strength by obtaining thinner layers, but this results in a longer printing time [15].

Another important consideration for any photopolymer used in AM is the layer thickness and the depth of recoating that takes place before curing. The recoating is dependent on both the printing method and the resin properties. The flow of resin over the solidified portion is critical for this situation. Therefore, high molecular weight acrylates commonly used for AM should be diluted using lower molecular weight acrylates

1.2.2 Photoinitiators

Since radical generation, initiation, and propagation are relatively fast systems, they are widely used in rapid prototyping. The first step in crosslinking a photoresin is the absorption of light, and photoinitiators that convert photolytic energy into reactive species initiate polymerization. Radical photoinitiators are generally classified as Norrish type I and type II [43]. Type I photoinitiators are monomolecular and clave into radical fragments when exposed to UV light of appropriate wavelength. Benzyl ketals are common type I initiators with very low energy n → π* transitions (350-360 nm wavelength). The photocleavage mechanism of Darocur 1173, one of the common type I photoinitiators, is given in Figure 1.10. The excited singlet state formed at the beginning can give an excited triplet by direct division or by inter-system transition.

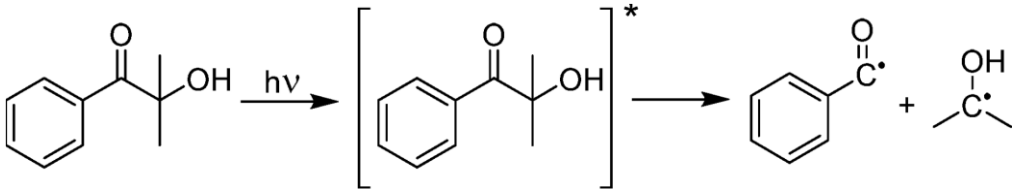


Figure 1.10 Photocleavage of Darocur 1173

In terms of energy, triplet and singlet are similar, but because they have a longer life, radical production with triplet is common [44]. Some of the widely used benzyl ketal initiators are Irgacure 184, Irgacure 561 and Irgacure 369 that undergo similar photocleavage reactions (Figure 1.11). Acyl phosphine oxides, such as TPO and BAPO, are from another class of Type I radical initiator and are preferred for use in AM devices with higher wavelength lamps such as DLP [45]. The phosphorus atom adjacent to the carbonyl atom lowers the energy level of the π* state and shifts the maximum n → π* transition to 400 nm. In fact, these and new generation germanium initiators such as Ivocerin allow the curing of highly filled systems since the heteroatom is divided from the carbonyl group [46].

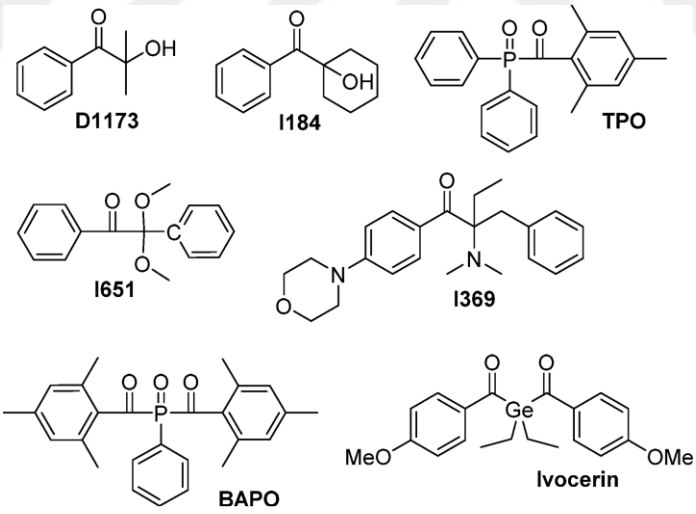


Figure 1.11 Radical photoinitiators of Type I that commonly cited in stereolithography studies.

Type II photoinitiators are two-component systems that composed from a co-initiator (or synergist) and a light-absorbing molecule (or sensitizer), as shown in Figure 1.12. To generate the initiator radical upon contact with light, the co-initiator transfers a hydrogen atom to the sensitiser. The most commonly used Type II photoinitiators are tertiary amines containing at least one alkyl [47, 48]. To enter the reaction, electron transfer takes

place to the excited ketone from the amine. Back electron transfer can be thought as a competitive reaction. The next step after proton transfer to the initiator radical anion from the amine radical cation is the rate limiting factor. Even though Type II initiators such as benzophenone and isopropylthioxantone are widely involved in SLA studies, the use of amine synergists is not preferred. [15]. One of the reasons for this is that mixtures of radical and cationic-based systems form many of the recently used SLA resins and second amines can be inhibited. Benzi-N-N-dimethylamine, which is used in an amount too low (0.01% wt) to be used as a synergist and classified as a cationic stabilizer in many studies, is a very effective hydrogene donor. [49]. By directly transferring hydrogen from monomers and solvents, Type II sensitizers can partake to polymerization, while Type II systems are more efficient with synergists. [50]. Hydrogen transfer can occur between many monomers. These include those including propylene glycol and ethylene glycol, and alkyl ketones adjacent to oxygen [51]. It is advantageous to use oligoether and oligoester carylate monomers with abstractable hydrogens, such as amines, that do not inhibit cationic polymerization while curing better in air than similar alkyl monomers.

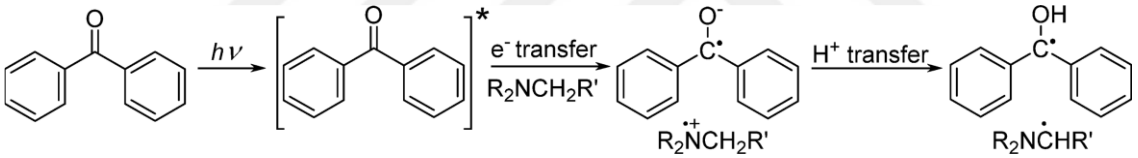


Figure 1.12 Radical reaction of Type II photoinitiators [15]

In terms of performance, the radical photoinitiator depends on the type of light source used. Conventional benzoyl photoinitiators initiate polymerization via UVA and UVB light sources (such as I651, D1173, and I184). Thus, they can produce with He-Cd lasers (325 nm), triple frequency Nd:YAG sources (355 nm) or UVA/UVB based DLP devices [52, 53]. Acyl phosphine oxide photoinitiators are superior for higher wavelength light sources. Bisocylgermanium initiators such as Ivocerin can be used for blue light curing printers [54]. The use of multi-radical photoinitiators in resins for light sources operating at wide ranges of wavelengths is also quite common.

Photopolymer resin studies compiled for mechanical applications and used in the DLP process are given in **A. 1**.

1.2.3 Acrylate and methacrylate monomers

Patents are often used to obtain information on the contents of monomers and resins used in photo-based printers, as most of the resins are commercial and proprietary. Murph et al., in order to obtain a patent in 1988, prepared a resin containing an N vinyl monomer (N-vinylpyrrolidone NVP) added as a reactive solvent and a synthesis prepared by dissolving a high viscosity oligomeric diacrylate in a liquid acrylate or methacrylate [55]. They used a synthesis involving both acrylate and methacrylate, emphasizing that solidification occurs rather slowly when methacrylate alone is used, while pure acrylates cause deterioration in the printed products. They exemplified a resin consisting of a urethane or epoxy-based diacrylate diluted in hexane diol dimethacrylate or trimethylol propane trimethacrylate (TTMA). They exemplified a resin consisting of a urethane or epoxy-based diacrylate diluted in trimethylol propane trimethacrylate (TTMA) or hexane diol dimethacrylate. NVP is fast-curing and provides "green strength", which represents the combined mechanical properties required to ensure conformance during development. Resins based on urethane acrylate and bisphenol A diglycidyl ether (DGEBA) are widely used in SLA studies due to the mechanical strength they provide thanks to the functional groups [56, 57]. Urethane acrylates are synthesized as a result of the reaction of isocyanates with hydroxy acrylates like HEA and HEMA. Here it is often after a polyol formed in a step before a polyol that reacts with an excess of diisocyanate small molecule [58]. A number of urethane acrylate monomers, with degrees of functionality one to six and defined as aliphatic or aromatic, are in commercial use. Structural monomers are generally not fluid enough to be used directly in 3D printers, so they are thinned with reactive diluent of a lower viscosity [59]. Multifunctional solvents like pentaerythritol tetraacrylate (PETA) and dipropylene glycol diacrylate (DPGDA) are often used to facilitate rapid crosslinking of the resin (Figure 1.13).

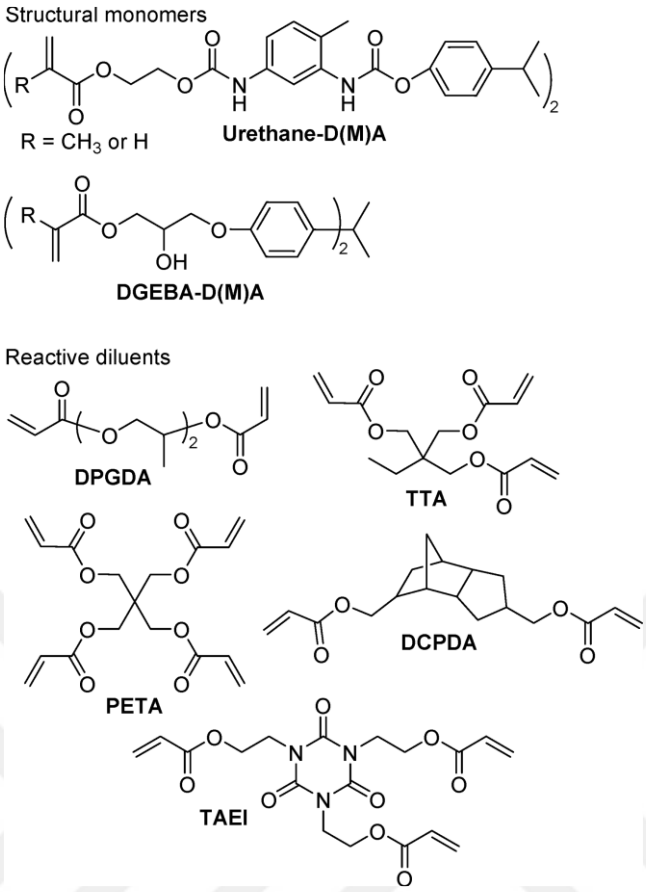


Figure 1.13 Acrylate and methacrylate monomers for rapid prototyping [15]

An acrylate monomer with a liquid, reactive and heterocycle core, such as Tris[2-[acryloyl)ethyl] isocyanurate (TAEI), can also advance the mechanical quality of the product [60]. A few SLA patent studies have used diacrylates with a cycloaliphatic core (such as DCPDA) because they allow a higher final modulus and tend to shrink less. Although they provide many advantages, acrylates, like all other vinyl monomers, are subject to shrinkage occurs along of the polymerization. Rate of shrinkage depends on the molecular structure. For example, bisphenol-based dimethacrylate (Bis-GMA) from cycloaliphatic and aromatic acrylates decreases by 5%, while triethylene glycol dimethacrylate, which is one of the common diluents, decreases by 12% [61]. Pre-arrangement of monomers using methods such as hydrogen bridges can help reduce shrinkage stress. Another method is to convert the polymer mechanism from a chain growth polymerization to a radical step growth mechanism. While inhomogeneous stress occurs as a result of curling and other deformation problems, polymerization shrinkage and related stress cause specific problems in layered production. Hull et al developed

rapid prototyping techniques for vertical structures based on the use of curved and dashed lines that create lower stress than continuous and straight fabrications [62]. The use of higher molecular weight oligomeric acrylates is a commonly preferred chemical methods that allows it to reduce shrinkage and the resulting curling [63]. Although heating the resin during production is not a method that can be used in all conditions, it can compensate for the increased viscosity problem.

1.2.4 Elastomers

Although studies on developing high-performance elastomeric materials using SLA and DLP methods were limited until a decade ago, they have become very common today due to their softness, elasticity, flexibility and high deformation rate [64–67]. Recently, the need for high-performance elastomeric materials has arisen from emerging studies such as soft robots, medical implants and artificial human tissues [68]. The most widely used are silicone-based elastomers due to their biocompatibility, high elasticity and negligible cytotoxicity [69–72]. Commercial examples of these silicone rubbers are Ecoflex (Smooth-on), SE1700 (Dow Corning) and Sylgard (Dow Corning). However, the thermal curing processes of these materials are limited to productions such as cutting, casting, molding and spin-coating. The researchers aimed to facilitate design and production by developing a 3D printing method, a direct ink writing (DIW) printer, and two-part silicone elastomer printing inks consisting of a base and crosslinker with an expensive platinum-based catalyst [73–78]. However, the parts had to be exposed to additional curing for several hours at room temperature after printing [75]. In addition, the resolution of the lateral surface of the part in the DIW process is limited by the diameter of the printing nozzle and the production of complex structures is significantly limited since support structures must be used. There are also studies on the UV curing of silicone elastomers [79, 80]. There are several commercial photocurable elastomers available, such as EPU40 from Carbon, Tangoplus from Stratasys, and Agilus30, developed for use in production with SLA and DLP. However, since these elastomers are based on acrylate and polyurethane, their elongation values are quite low. Tingting Zhao et al. synthesized mercapton-functionalized polysiloxane (MPS) to obtain a silicon elastomer-based photoresin and added vinyl-terminated poly-(dimethylsiloxane) with different molecular weights, as well as different types of filler silica particles and photoinitiator [68]. Then,

the synthesized resins were cured in a high UV DLP printer, resulting in a series of silicone elastomers with modifiable hardness and mechanical properties. In another study, researchers aimed to produce parts with different mechanical properties by changing the mixing ratios of epoxy aliphatic acrylate (EAA) and aliphatic urethane acrylate (AUD). 2% trimethyl benzoyl diphenyl phosphine oxide (TPO) was added to the resin as a photoinitiator since it is suitable for low cost DLP printer and two-photon polymerization. It has been determined that the elastomers produced have an elongation of 1100%, 5 times compared to commercial elastomers and equal to the most flexible silicone rubber [64].

1.2.5 Photopolymer based composites

The expansion of the photosensitive resin market with the increasing use of VP has accelerated the efforts to synthesize new resin varieties. In addition to improving the functionalities and mechanical properties of the manufactured parts such as biocompatibility, magnetism and piezoelectricity, micro or nano filled resins have been developed in order to prevent distortions that occur during the reaction [33, 81]. Polymer composites have excellent mechanical properties and are highly preferred in engineering studies due to the flexibility they offer in design [82]. There are some difficulties encountered during production such as cost, control of fiber direction, determination of matrix and reinforcement ratio. Composites have a wide variety of production techniques such as material lay-up, comparison molding technique, resin transfer molding technique and filament winding. Two-stage processes are used, namely material placement and consolidation or curing. In the second stage, it is very costly to provide the necessary equal pressure distribution and the equipment used. On the other hand, producing composites using 3D printing process has more advanced features compared to traditional methods, while it also provides advantages in terms of cost, time and convenience [83, 84]. In order to provide a workable layer thickness, the additive to be used must contribute minimally to scattering and must be transparent to allow radiation to pass through the depth of the layer. While turbidity due to scattering limits the penetration and curing depth of the resin, in some cases it can increase the length of the interaction path by increasing the probability of the formation of a single photon that initiates the reaction [85]. The effects of the filler on scattering depend on its size and concentration, as well as the difference in refractive index between filler and resin [86]. When metallic particles are

used as filling materials, they make curing difficult as they deprive the resin of incident light due to their high reflective properties [87]. The increase in viscosity inhibits the recoating action of the resin, slows down the diffusion of active centers by reducing molecular mobility, and decreases the polymerization rate. Therefore, the incorporation rate of the filling material should be adjusted very well [88]. Viscosity can be controlled by increasing the processing temperature. Another method to prevent the increase in viscosity due to the addition of filler is the use of nanoparticles as filler material. Due to their high surface area-to-volume ratio, they can improve the mechanical and morphological properties of the part more, although they are used in much lower amounts than micro-fillings [81]. Thanks to their small dimensions, they do not hinder reaching the minimum layer thickness. In a new method used to prevent viscosity increase, nanoparticle production is carried out in-situ [89]. In order to produce a homogeneous distribution without agglomeration, the precipitation rate of the filling materials in the resin should be low, that is, the suspension times should be long [90]. Feng et al. have produced nanocomposites to increase fracture toughness in net-shaped structures by adding graphene as a reinforcement material. Using the DLP method, they studied the effects of graphene on viscosity, recoating, mechanical and thermomechanical properties. The resin contains 58% polylactic acid-polyurethane oligomer (PLA-PUA) as oligomer, 38% triethylene glycol dimethacrylate (TEGDMA) as reactive solvent and 3% phenyl bis(2,4,6-tr-imethyl benzoyl) as initiator. 0.5% wt% nano graphene powder was added to the resin. In the results, it was determined that the flexural modulus increased from 2.65 GPa to 3.06 GPa with an improvement of 14% compared to the pure resin. It was also observed that the fracture toughness increased by 28% compared to the pure resin [91]. In another study, researchers synthesized a photocurable resin by adding 1% bis(2,4,6-trimetilbenzoyl)-phonylphospineoxide (photoinitiator) to the resin consisting of a mixture of bisfenol A glycerolate (1glycenol/phenol) diacrylate (Bis-GMA) (epoxy) and1,6 hexane diol diacrylate (HDDA) (reactive solvent) added in half. The mechanical and morphological properties were investigated by adding surface modified and unmodified graphene oxide (GO) nanoparticles at the rate of 0.05%, 0.1%, 0.15%, 0.2% and 0.25% wt% to the resin. In the results, it was determined that the surface modification significantly improved the mechanical properties [81].

Table 1.2 Polymer composites printed via DLP process for mechanical applications

Base Material	***Additives and Reinforcements***	***Highlights***	***Properties Improved***
UV-curable PLA-PUA resin **[91]**	• Graphene powder	• Light wavelength 405 nm	• İncrease in frlxural modulus up to 14% • Increase in flexural modulus up to 4% • Increased in farcture toughness up to 28%
High temp resin V1 **[168]**	• Multi walled carbon nanotubes (MWCNTs)	• Layer thickness 30 µm • Exposure time 5.12 s • Optimum concentration of MWCNTs 0.05 %wt	• Increase in young's modulus and three point bending strength with CNT reinforcement
Alumina (Al2O3) **[169]**	• Zirconia (ZrO2)	• Light wavelength 405 nm • Sintering temperature 1600 0C • Debinding temperature 600 0C	• Maximum achieved hardness up to 17.43 GPa • Increase in bending strength up to 29% • Increase in fracture toughness up to 24% • Maximum achieved relative density 99.4%
BisGMA **[81]**	• Hexanediol diacrylate (HDDA) as solvent • IRGACURE 819 as photoinitiator • Graphene oxide (GO) nano particles with surface modified and non modified	• Light wavelength 405 nm • Layer thickness 50 µm • Exposure time 7 s for first three layers at bottom, 5 s for remaining layers	• Increase in maximum tensile strength up to 73% between surface modified and non-modified • Increase in Shore D hardness value up to 25%
Preceramic polysilazane (PSZ) **[170]**	• Nanofillers SiO2 and SiC nanofibers	• Printing resolution 40 µm • Layer thickness 100 µm • Pyrolysed temperature 1300 0C • Light wavelength 405 nm • Optimum ramping rate 3 0C min-1	• Increase in flexural strength up to 179% • Maximum elastic modulus 45 GPa
Poly((mercaptopropyl)methyl siloxane) (MPS) **[68]**	• Photoinitiator: ohenyl bis (2,4,6-trimethylbenzoyl) phosphine oxide (PI 819) • Reinforcing fillers: Precipitated silica and fumed silica • Vinyl-terminated poly-(dimethylsiloxane) (VPS) • Silica filler • Silica elastomers	• UV light wavelength 405 nm • Layer thickness 100 µm	• Increase in elongation up to 350% • Increase in tensile strength up to 763% • Maximum achieved elongation at break of 1400%
Polyborosilazane **[171]**	• Si3N4 whisker	• Light wavelength 405 nm • UV dose 528 mW/cm2 • Leyer thickness of 50 µm • Optimum sintering temperature 1200 0C	• Increase in flexural strength up to 219% • Maximum young's modulus 54.1 GPa • Maximum hardness 3.4 GPa

Photopolymer resin studies compiled for composite applications and used in the DLP process are given in Table 1.2.

1.2.6 Biocompatible and photocurable polymer resins

Biocompatible resins have a great potential for biomedical studies with the VP method due to their wide availability, propensity to form porous structures and high resolution. Prosthetic devices, scaffolds for soft or hard tissue construction, and implants are various areas where biocompatible polymers are used. The effects of the resin used on the biocompatibility, biodegradability and mechanical properties of the produced part should be taken into account during the synthesis phase. Biocompatible resins used for implant production should not exhibit cytotoxic and mutagenic properties and should be suitable for cells to adhere, function and multiply [92]. The components that cause the most cytotoxicity are photoinitiators, and their ratio in the resin should be carefully determined so that it does not slow down the curing and is low enough not to impair biocompatibility [93]. In addition to the use of biocompatible reagents, the use of low-component resins such as PEG diacrylate-based inhibitor and solvent-free resin is another solution [94]. One of the versatile polymers used for biomedical applications is polyacrylates with biocompatibility. Maturi et al. developed a new biocompatible resin that is more rigid, has higher mechanical resistance and is less brittle and used it in the DLP process [95]. Blend, poly(1, 3-propanediol-co-glyceryl) itaconate-co-vanillate (PPGIV)(48.5 wt%), bis (2-(methacryloyloxyethyl) itaconate (BHI)(24 wt%), tris(2-(It consists of methacryloyloxyethyl) citrate (THC)(24 wt%), initiators (1.5 wt%) and dyes (0.01 wt%). The resin consists of 96.6% bio-based components. As a result of the mechanical tests, the tensile modulus was 64 MPa, the ultimate tensile strength was 5.4 MPa and the ultimate elongation was 18%. Resins obtained by combining acrylates with urethane units and trimethylolpropene triacrylates offer very good biocompatibility for the production of celular bone replacement materials [96]. Some of the usage areas of such resins are the production of implants with concerted geometric and physical properties such as bone fracture fixation devices, artificial hips, knee pieces, nerve guide channels and prostheses [33]. Chen et al. synthesized internal PCL-based polyurethane acrylates such as m-PUA530, m-PUA800 and mPUA100 for use in DLP printers, and then changed the ratios of poly(ethylene glycol) diacrylate (PEGDA) and propylene glycol (PPG) to obtain 12

resins from them [97]. Then, compression and hardness tests were applied to the samples produced from 12 synthesized resins. acrylates are more toxic than their corresponding methacrylates [98]. Cell viability is affected by functional groups in monomers and is another important consideration in addition to cytotoxicity. In order to reduce the cytotoxicity of the generally used acrylate and methacrylate monomers, it is necessary to maximize the conversion of unreacted groups. Parts manufactured for this purpose must be exposed to supercritical CO2 for additional hardening prior to implantation [99].

Biodegradable polymers are used for temporary scaffolds that act as supports for tissue regeneration and drug delivery systems [100]. Biodegradable polymers are generally composed of ingredients that contain ester-, amide- or carbonate-bonds and can be hydrolyzed along their backbone chains [101].

The issue of vascularized organ development in biomedical studies contains great difficulties in terms of production [102]. Blood vessels are essential for large organs to perform their metabolic functions, and therefore, methods that can create complex vascular systems and innervation should be developed. Zhang et al. investigated the latest developments on blood vessels and functional vascularized tissue in biomedical studies using three-dimensional printing method. Concerning tissue fabrication using the AM technique, further scientific studies are required due to limitations in printing at fine resolutions at miniature scale, and also the inability to provide the mechanical properties available for vascularized tissues [103]. On the other hand, 3D printing of sensitive human parts in tissue engineering, together with versatile bioresin developments, offers significant potential. Bioreactors work together with factors that promote angiogenesis and maturation of biomaterials produced by AM technique with the required properties [104]. The combination of various bioresin and AM techniques yields positive results for the fabrication of human-scale tissue constructs [105].

The mechanical properties of natural human tissues vary according to the anatomical region.

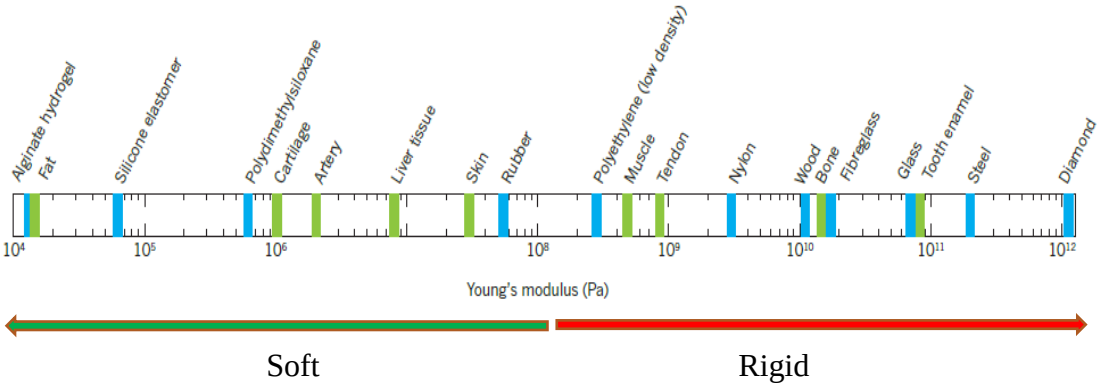


Figure 1.14 Approximate elastic modulus (Young's modulus) of selected engineering and biocompatible materials [106].

For example, the compressive strength ranges from 0.25 to 1 MPa for articular cartilage, while it ranges from 3.5 to 3000 MPa for trabecular bone [107, 108]. Biocompatible resins have a wide range that can enable the production of implants with many different mechanical properties and hardness (Figure 1.14). From this point of view, the mechanical properties of tissue engineering scaffolds and the materials to be used together with it should be adapted to the region where the implantation will be applied [92]. The types of oligomers used and, if more than one oligomer is used, the ratio between the oligomers are the most important factors affecting the mechanical properties. For example, PLA copolymers formed with PEG (PLA-PEG-PLA) are softer due to their low modulus compared to that formed with PCL(poly(D,L-lactide-co-ε-caprolactone)) [109–111]. Mechanical properties of scaffolds vary according to crosslink densities. For example, structures with denser crosslinks have higher toughness and modulus. The crosslink density can be reduced by using higher functionality oligomers or higher amounts of reactive diluents [112, 113]. These structures of scaffolds, which can be produced by AM technique and have variables such as porosity, pore size and pore architecture, also affect the mechanical properties [109, 114]

Due to their remarkable properties such as flexibility, chemical stability and corrosion resistance, elastomers (rubbers) are currently preferred materials for researchers in the biomedical field. Among the many elastomers on the market, polydimethylsiloxane, also known as PDMS, has come to the fore in recent years. This material has a wide range of uses, from mechanics to electronics, including biomedicine. Ease in production, optical transparency, biocompatibility and low cost are other reasons for its extensive use.

Therefore, mechanical sensors, electronic components, electro-chemical sensors, biomedical research and medical implants are the most common PDMS applications [115–119].

Photopolymer resin studies compiled for biomedical applications and used in the DLP process are given in A. 2.

2 MATERIALS AND METHODS

The beginning of this study is the production of a new and original printer in our laboratory, with the desired features, based on the DLP prototype. In this context, examinations were made on the prototype and its disadvantages were determined. After the examination, the design of the device to be produced was made. Using the budget of the allocated OYP program, parts were purchased and the device was manufactured. After the calibrations and programming required for sample production were completed, resin synthesis studies compatible with the DLP projector mounted on the device were carried out. In this part, the most research and time required was the provision of the appropriate photoinitiator. After the resin synthesis was completed and the test samples were printed, nanocomposite production was carried out. Subsequently, trials were conducted for the production of biocompatible and flexible resin suitable for production with printer and printing specimens was carried out with the desired properties. Produced samples were subjected to biocompatibility tests at İstanbul University, Faculty of Medicine, Department of Physiology. The flow chart of the studies carried out within the scope of the thesis is given in Figure 2.1. All studies for the production of biocompatible and flexible samples are described in detail below.

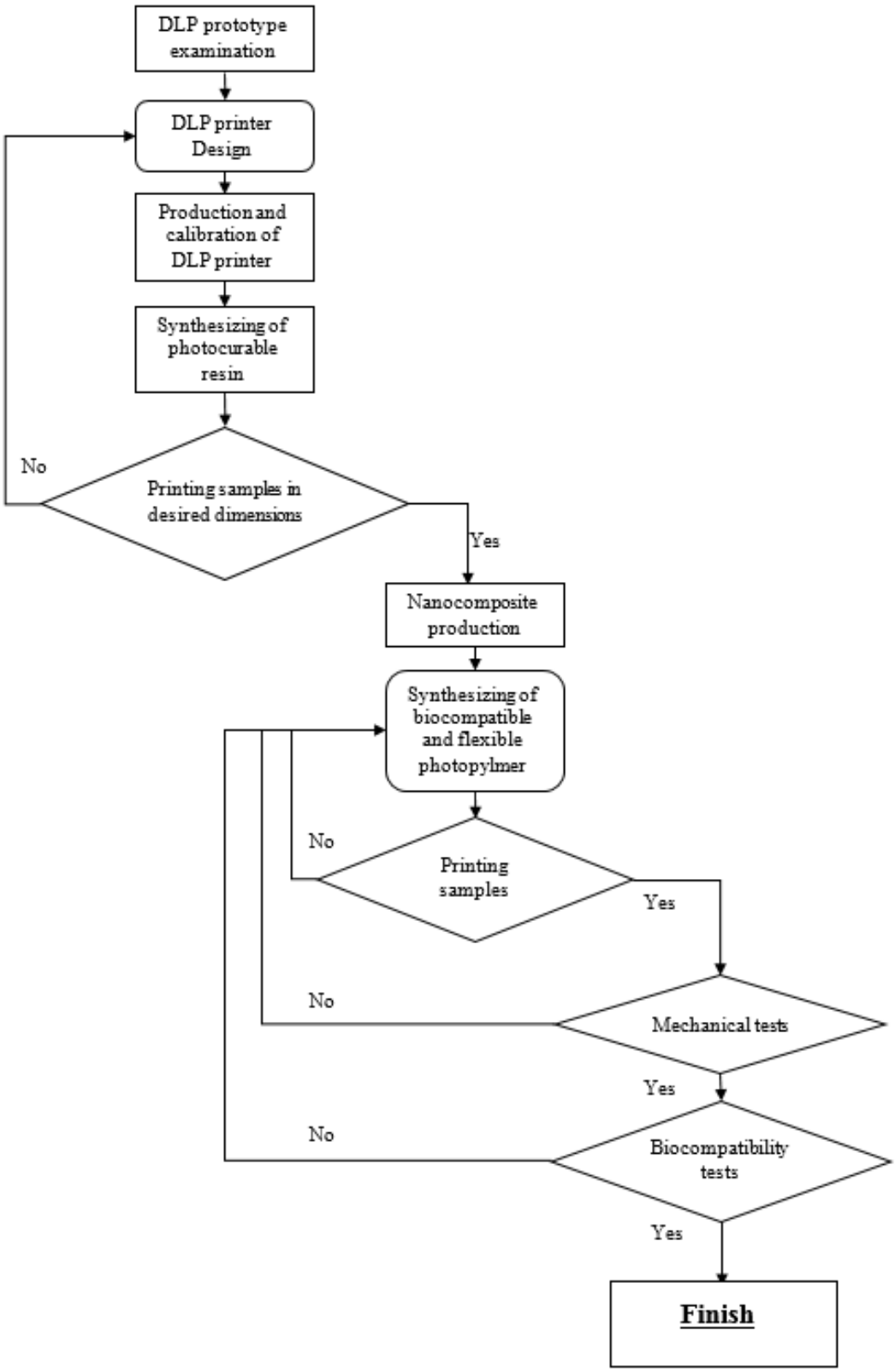


Figure 2.1 Flow chart of the method in the thesis

2.1 Review of Existing DLP Device

Before moving on to the new design, examinations were made on the existing device and its deficiencies were determined. Identified deficiencies are listed below.

- Due to the small size of the table and the chamber (120x150x165), large geometries cannot be printed in a single operation.
- Long pieces cannot be formed due to the short Z axis.
- Adhesion of the printed part with the effect of temperature as a result of contact with the Teflon-backed bottom of the chamber
- Due to the adhesion on the bottom of the chamber, the parts break during printing or fall off the building platform.
- Due to sticking and single bearing design of the z-axis, the load on the ball screw is high.
- Due to the fact that UV light reaches the resin by passing through the Teflon material covering the bottom of the chamber and as results long curing time, energy loss and the light refraction/reflection occurs.

In order to eliminate these disadvantages and shortcomings, a new design has been made instead of the DLP printer shown in Figure 2.3. In this new design, the part creation direction has been changed, the chamber and table dimensions have been enlarged, and the z-axis has been extended.



Figure 2.2 Existing DLP printer

2.2 Design of the New DLP Printer

While designing the new device, the following changes were made in order to eliminate the disadvantages mentioned above (Figure 2.3).

- ✓ By reversing the printing direction, the contact between the chamber and the part was cut off. Thus the adhesion, breaking and ruptures were prevented.
- ✓ By enlarging the chamber and table dimensions (220x230x265), it is possible to print larger parts in a single process.
- ✓ With the renewal of the projector, higher brightness and resolution have been achieved.

- ✓ Vat and platform are replaceable and designed to be easy to assemble. In this way, smaller samples will be prepared without wasting material by placing a smaller platform and vat while preparing new chemical mixtures.
- ✓ The projection is mounted on the channels of the sigma profiles, and the movement feature is provided to provide full focus on smaller tables.
- ✓ By removing the Teflon chamber base, direct contact of the UV light and the resin was ensured. In this way, higher radiation is obtained on the resin and the curing time is reduced.

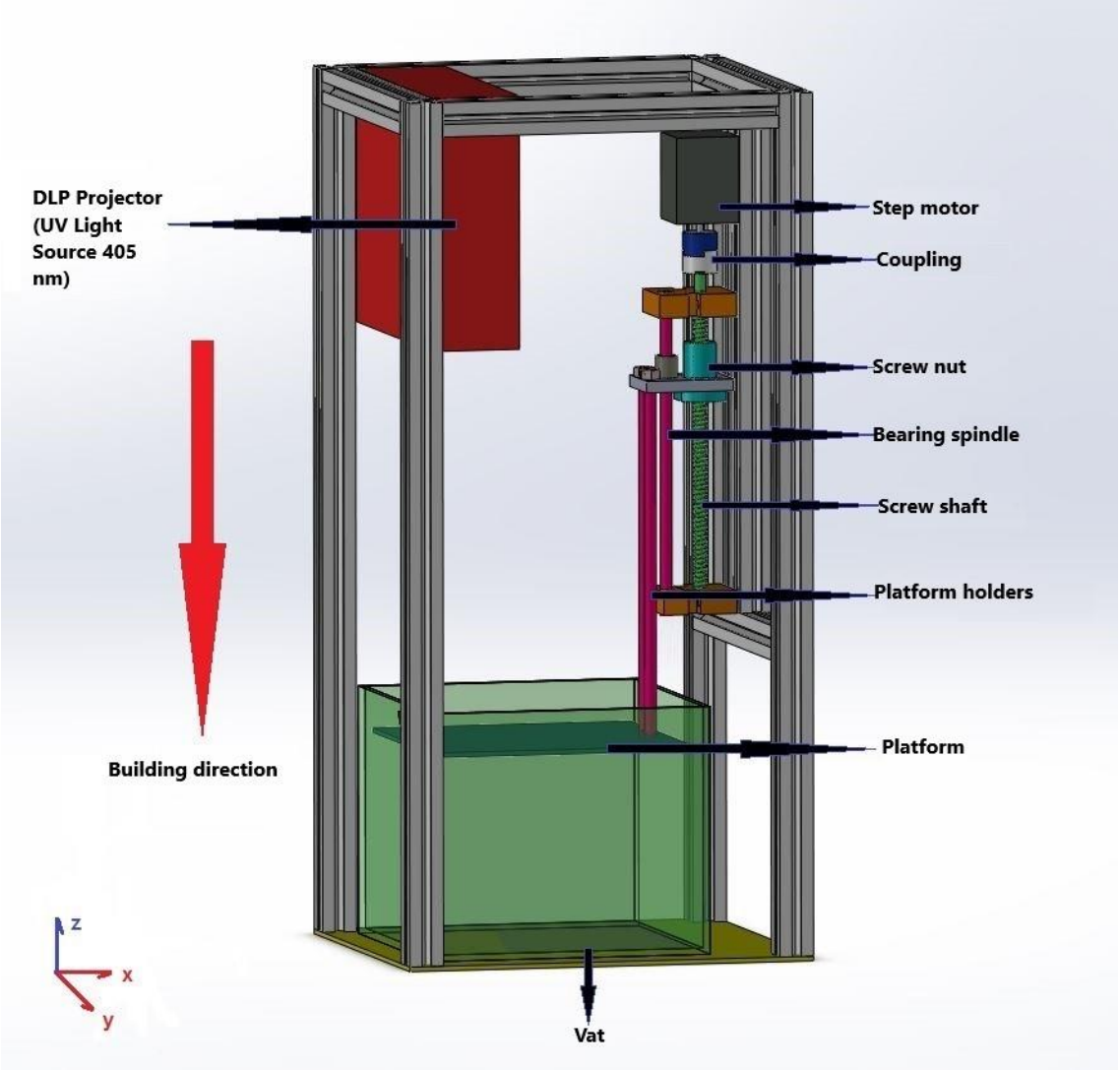


Figure 2.3 New design of the DLP printer

2.3 Manufacturing and Programming of the DLP Printer

The fabrication and assembly of the printer parts was carried out in the Basic Manufacturing Operations Laboratory. Calibration and programming were done in the 3D printers laboratory.

2.3.1 Manufacturing process

After the design was created and the movement in the z-axis was tested, the production of the printer started. The purchases of the necessary parts for the manufacture of the device were allocated from the OYP consumables allowance, and the manufacturing and assembly processes were carried out in the Basic Manufacturing Operations Laboratory of the Mechanical Engineering Department. 30x30 cm sigma profiles were chosen to be used in the main body and carrier frame of the device. For the platform, aluminum 5083 alloy is preferred due to its opacity that will not reflect or disperse the light. Ball screw and nut assembly material is fine machined stainless steel and is selected as standard with coupling, motor and bearings. For the bearing, the wear caused by the friction between the bearing and the shaft is minimized by using chrome-coated steel. The stepper motor was chosen because movement is required at intervals as low as 0.1 mm from the motor to be used for the movement to be given to the Z axis. DLP type projection has been selected and its features are as indicated in Table 2.1.

Since UV-curable resin is used, DLP type projection was chosen as the light source in the production of the device. DLP technology uses UV-A type lamps over 405 nm wavelength instead of LCD or LED lamps for display. In order to get higher efficiency from UV light, the filter on the device has been removed. The removed filter is used to protect the eyes and skin from the harmful effects of UV light. For this reason, precautions should be taken to protect eyes and skin during use of the device.

Table 2.1 Properties of DLP projection device

Trademark	Acer
Model	X1273 1024x768 XGA3000 Ans 13.000:1 3D
Product code	X1273
Native resolution	XGA (1024 x 768)
Brightness	3,000 ANSI Lumens (Standard), 2,400 ANSI Lumens (ECO)
Contrast ratio	13.000:1
Aspect ratio	4:3 (Native), 16:9
Unit weight	2 Kg
Connections	Analog RGB/Component Video (D-sub) x 2
	Composite Video (RCA) x 1
	S-Video (Mini DIN) x 1
	PC Audio (Stereo mini jack) x 2
Video compliance	Video Signal Format;
	NTSC
	PAL
	SECAM
	Video Signal Standard;
	HDTV
Lamp type and lifetime	Osram 190 W User replaceable P-VIP lamp
	5,000 hours (Standard), 6,000 hours (ECO), 10,000 hoours (ExtremeEco)*
Dimensions	264 x 220 x 78 mm (10.4" x 8.7" x 3.1")

The overflow of resin caused by the immersion of the platform and its holders into the chamber during printing is controlled by the opened channel. The printer produced is shown in Figure 2.4.

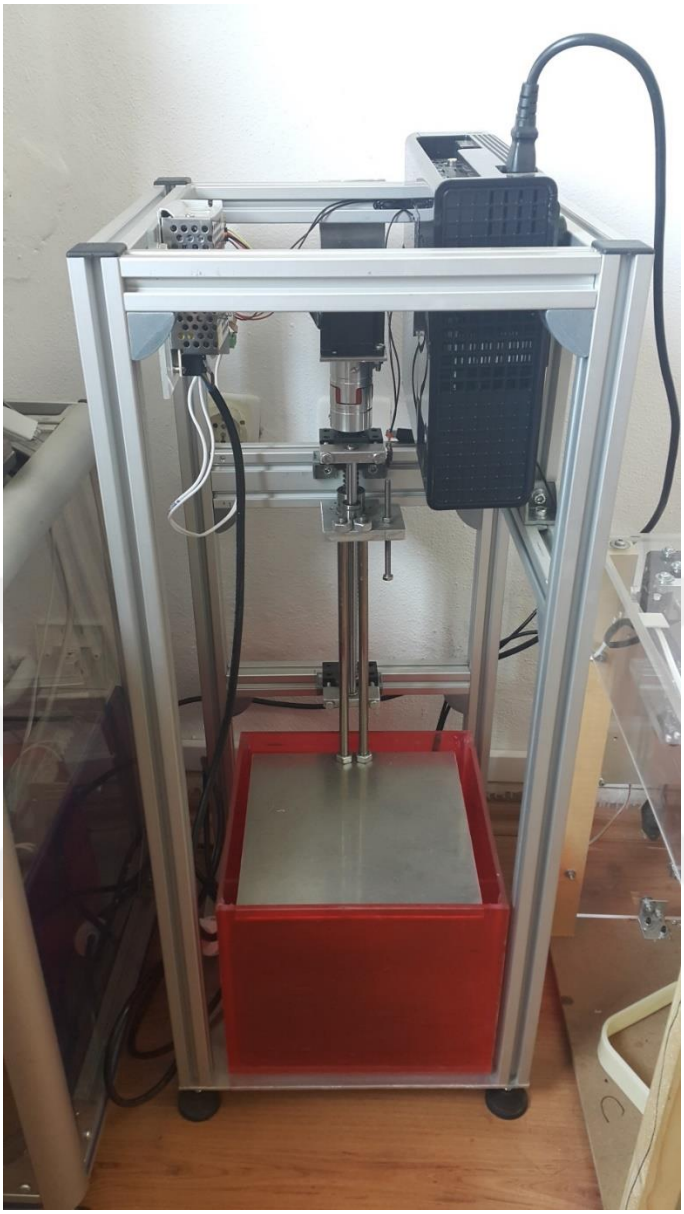


Figure 2.4 Printer manufactured within the scope of the thesis

2.3.2 Circuit board of the device

In order to provide computer control and automation of the device, an all-in-one system was used instead of the motor driver and circuit board used in the previous device. For the control of the motor, Ramps 1.4 circuit board, which also contains the driver and can be integrated with Arduino, was chosen (Figure 2.5).

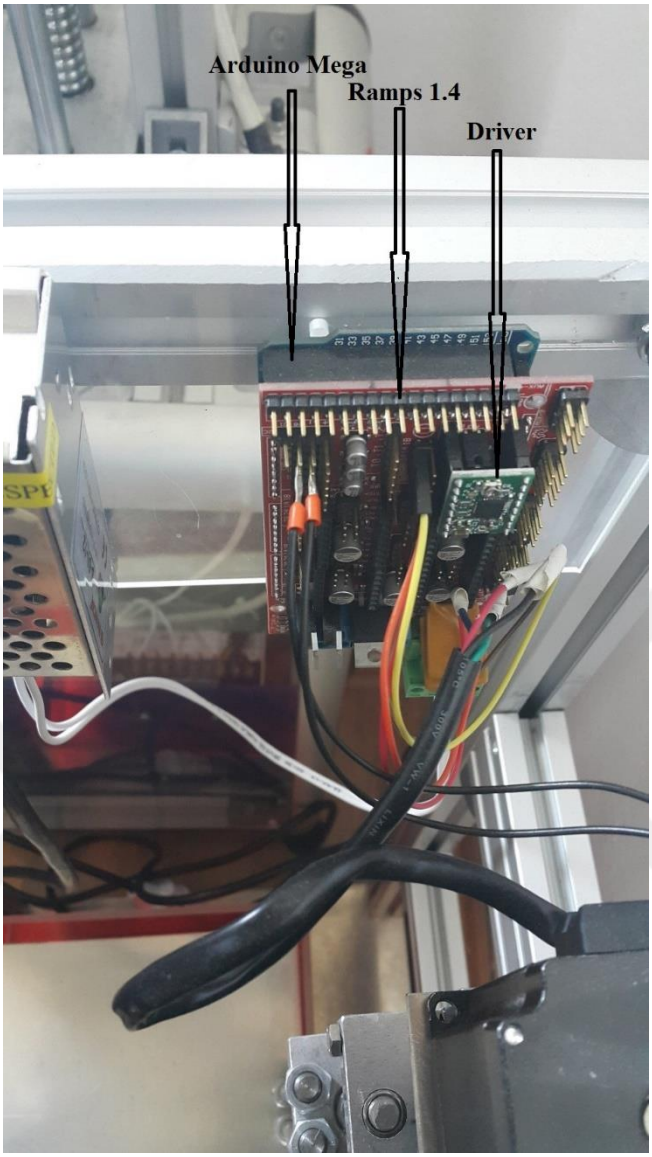


Figure 2.5 Arduino Mega board system integrated with Ramps 1.4

The advantages of this new system over the previous one are as follows:

- Instead of checking the reprogramming before each printing, this operation can be completed in one go, thanks to the program loaded on the circuit board.
- Rather than using 2 separate programs to drive the engine, prepare the 3D model and prepare the G-code, it is much simpler to use by collecting them all in one program (Creation WorkShop).
- No need to write G-code by changing the inputs such as movement direction, distance, size with simple interfaces on the program
- It takes up much less space on the device and increases the usage area.

After the circuit board system was mounted to the device and the motor connection was made, the operating principle of the device and the characteristics of the motor (part forming direction, reference coordinates, motor-screw shaft pitch relationship equation, etc.) were entered into the Arduino interface. In order to determine the reference point of the platform and prevent the nut from overlapping the bed, a control switch was added and the program was entered by connecting it on the circuit board. The motor step has been changed to micro-stepping to reduce vibration and ensure precision in short distance movement.

2.3.3 Configuration and programming

Arduino 0023 software was used for calibration and configuration of the z axis movement (Figure 2.6).

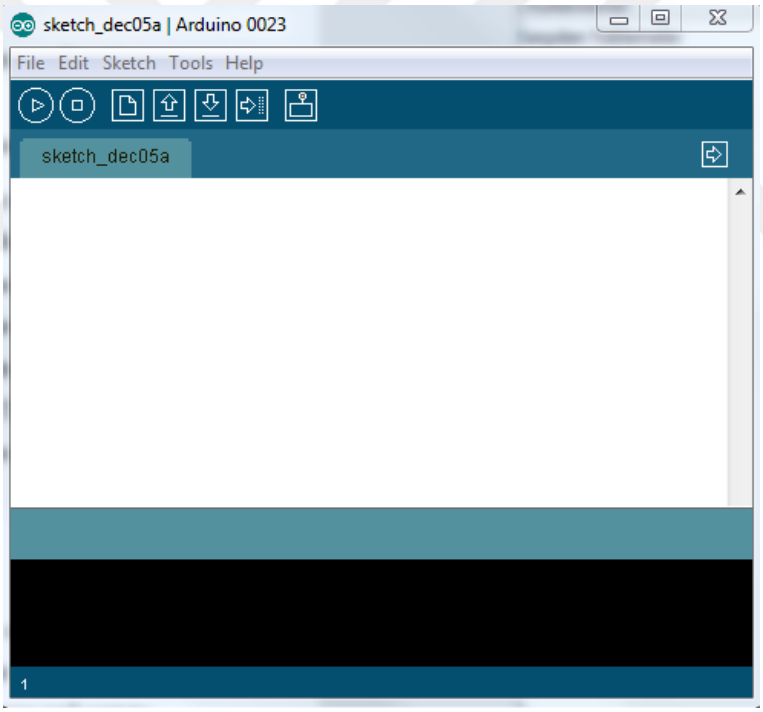


Figure 2.6 Arduino 0023 software

The distance of the movement in the z-axis of the platform with a single rotation of the stepper motor was calculated and processed into the software and sent to the circuit board. The movement of the device in a single axis was specified and the position and on-off information of the safety switch were entered. The configuration page with step formulation is given in Figure 2.7.

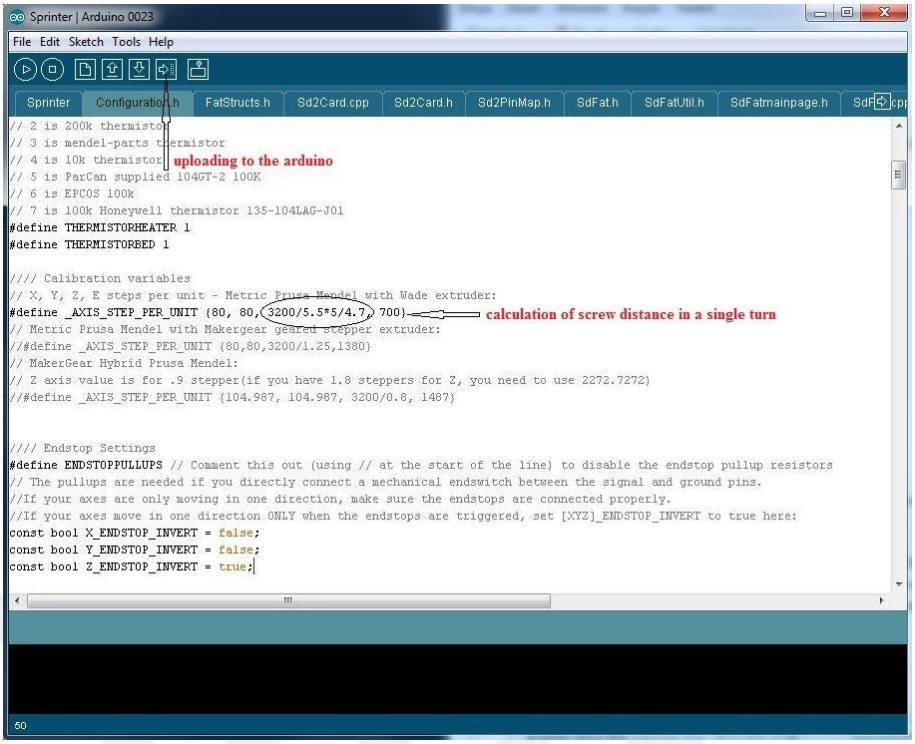


Figure 2.7 Configuration of the arduino

2.3.4 Printer software for computer controlling

CreationWorkshop was used to control the printer because it has an easy-to-use interface and has the ability to run without installation. The image of the part to be printed on the software interface is given in the Figure 2.8. The view of the part in the vat can be examined on the 3D view screen, and object info and slicing operations are also performed with this menu. In addition, when the unit price of the resin to be used is entered into the program, the calculation of the required cost for printing can also be seen.

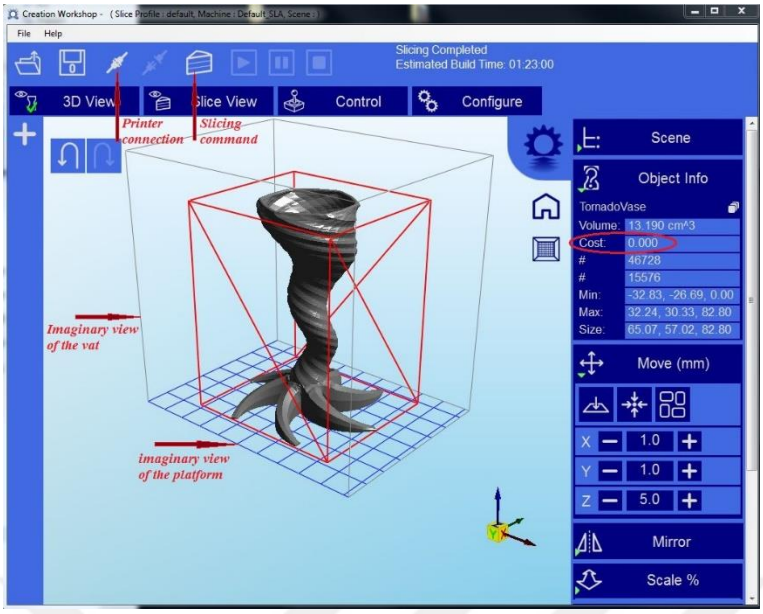


Figure 2.8 Demonstration of the 3D view menu

With the help of the slice view option, after the slicing process is completed, the geometries of the UV light that will be reflected on each layer can be examined and controlled (Figure 2.9).

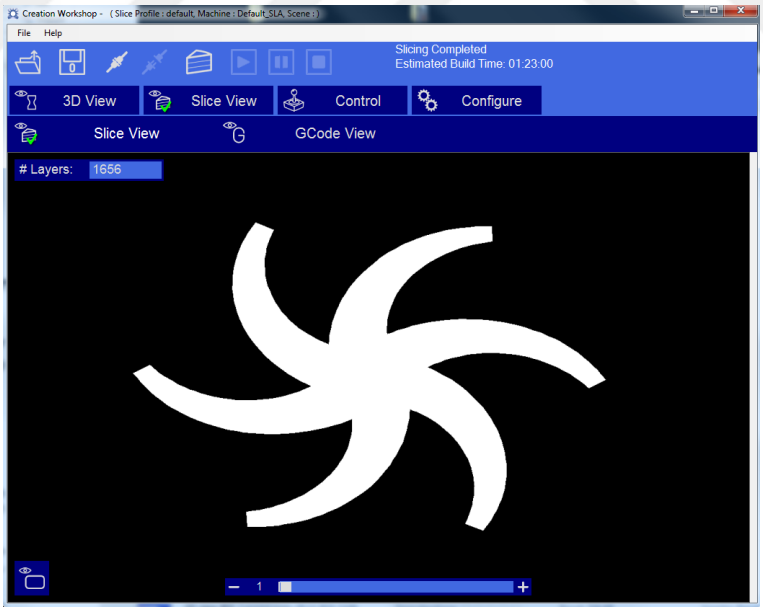


Figure 2.9 Demonstration of the slice view menü

In addition, the production codes to be sent to the device can be checked and changed using the G-code view option (Figure 2.10).

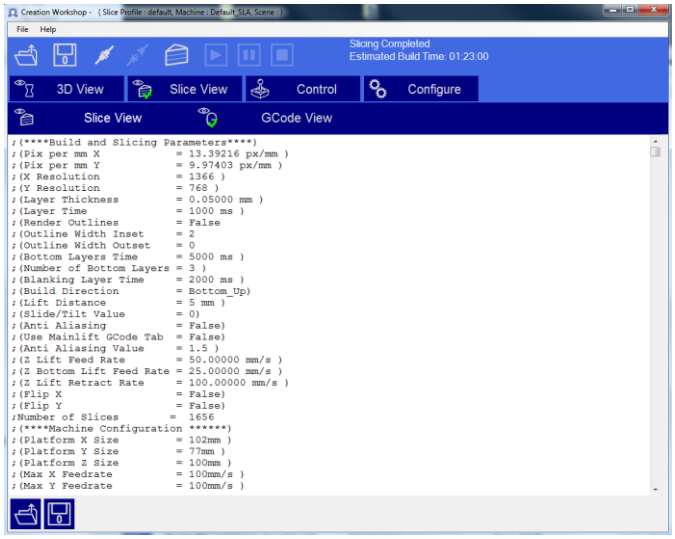


Figure 2.10 Demonstration of the GCode view option

Using the control menu shown in the Figure 2.11, the z axis can be moved manually when necessary and the platform can be sent home.

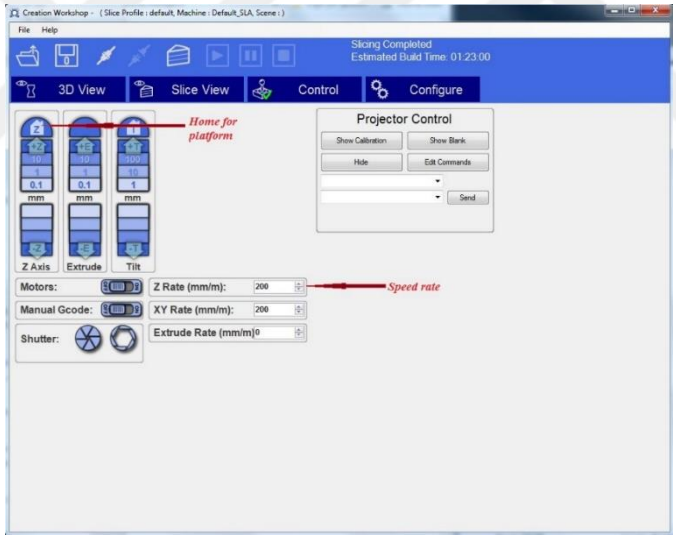


Figure 2.11 Demonstration of the control menu

With the configure machine option in the configure menu, the motion and dimensional settings of the device, port options for the circuit board connection and the projection connection are controlled (Figure 2.12).

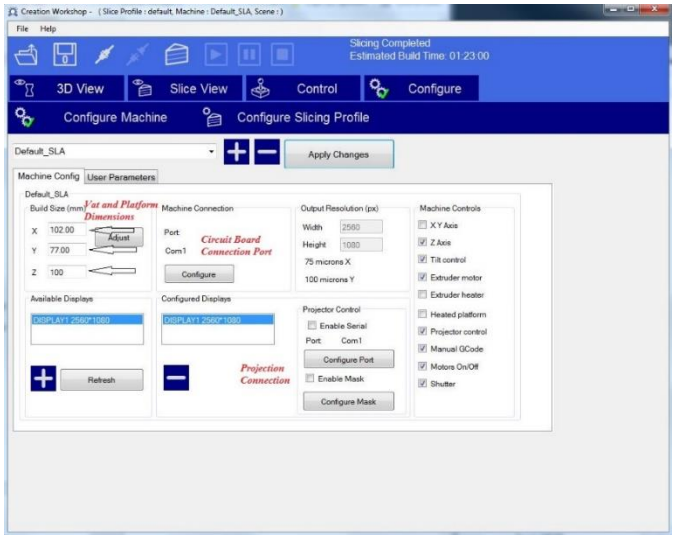


Figure 2.12 Demonstration of the configure machine option

With the configure slicing profile, another option under the configure menu, many adjustments are made such as layer thickness, exposure times, production direction (bottom-up or top-down), z-axis progression and rotation speeds and lifting movement parameters as shown in Figure 2.13. Another important point here is to determine the number of initial layers and the durations to be applied to them when entering the exposure times. The parameters of the starting layers are decisive in terms of the adhesion of the part to the platform and the solidity of the beginning of the part. Finally, the unit price of the resin to be used in production can be added in this option and the material cost of the printing can be seen in the 3D view option.

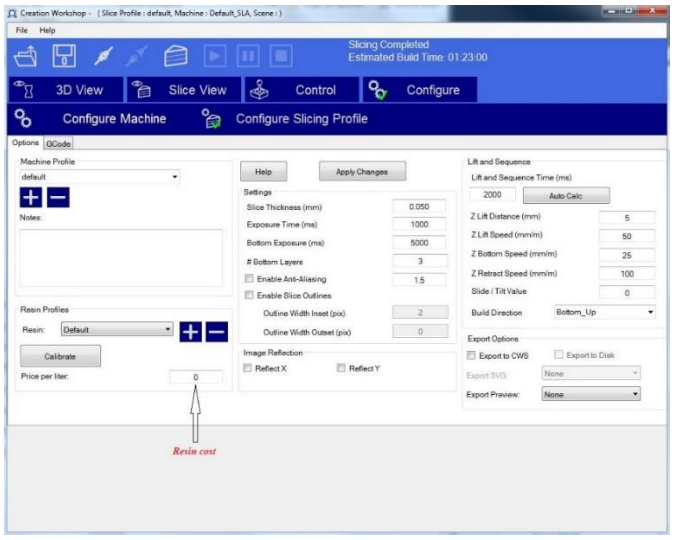


Figure 2.13 Demonstration of the configure slicing profile option

2.4 Synthesizing of the Photocurable Resin

For the synthesis, first of all, commercial resins were examined and their contents were investigated. After the studies for resin production were completed, synthesis was made and the first samples were printed on the device.

2.4.1 Identifying and supplying materials

After the device manufacturing and calibration were completed, researches were started to study for the photocurable resin. It has been determined that epoxy acrylate, reactive solvent and UV photoinitiator are used as resin components in the market and in other studies. In line with the information obtained, a contact was made with SunChemical® company and a sample request was made for Bis-GMA (Bisphenol A glycerolate (1 glycerol/phenol) diacrylate) (Figure 2.14) as epoxy and HDDA (1.6- Hexanediol diacrylate) (Figure 2.15) as reactive solvent. 20 lt Bis-GMA and 10 lt HDDA were provided by the company to be used for research purposes in return for demand.

The part that spent the most effort and time was the detection and supply of the photoinitiator. As mentioned before, the UV wavelength provided by the projector used is 405 nm. Since this wavelength is the least harmful light to human skin and eyes, it is preferred in projectors that are frequently used in daily life. The problem here is that there is no photoinitiator that can be active at the mentioned wavelength in the content of the resins used in the market. For this reason, the limited trade of the photoinitiator in the market makes it difficult to reach. Because in general, the curing area of the devices used in production with UV is closed and there is no contact with humans, so lamps with very low wavelengths are used. The photoinitiators used under these conditions are also unable to cure the resin of our own production. As a result of further research, it has been determined that the brand of the photoinitiator with the desired properties in the Turkish market is IRGACURE® 819 (Phenylbis(2,4,6-trimethylbenzoyl)phosphine oxide) (Figure 2.16). A sample request was made for research purposes by contacting the Turkish branch of BASF, the manufacturer of the material, and 200 gr of the photoinitiator was provided for free of charge.

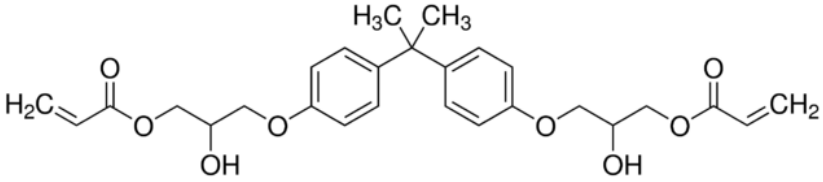


Figure 2.14 Molecular formula of the Bis-GMA (Cas no 4687-94-9)

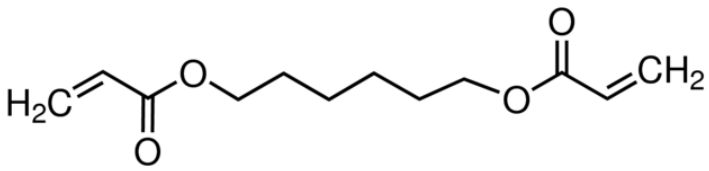


Figure 2.15 Molecular formula of HDDA (Cas no 13048-33-4)

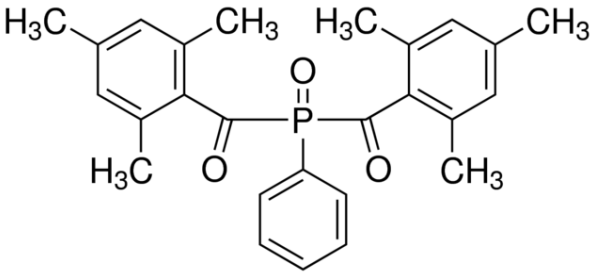


Figure 2.16 Molecular formula of IRGACURE 819 (Cas no 162881-26-7)

2.4.2 Synthesizing the resin

500 ml epoxy acrylate and 500 ml (HDDA) were mixed by a magnetic stirrer at 500 rpm for 20 mins. Following, photo initiator IRGACURE 819® was added to mixture as weight percentage of 0.5% and continued to stirring until getting a limpid outlook (approximately 1 hour). HDDA was used as reactive solvent to decrease resins viscosity due to easy flow on the printing table and easy print with DLP. With UV light, double bonds of phosphorus at photo initiator broken and start curing reaction.

2.5 Test Piece Printing and Revision of the Printer

While no problem was observed in the curing of the resin in the experiments, some errors were detected at the device during production. These errors are as listed below.

- Since the bedding is made at the level of the screw with a single shaft, it has been observed that the platform wobbles while moving along the z-axis during

production, and as a result, fluctuations occur on the side surfaces of the produced part.

- Aluminum 5083 was chosen in the production of the platform because it is more matte than the metals in the inventory. However, it was insufficient to absorb the light coming on it and causes fringes to form in the first layers of the part and gelated aggloremations in the resin in the reserve.
- When the production direction is bottom-up, it is necessary to fill the entire chamber with resin. Since the chamber is designed very large for the produced printer, it is necessary to fill 4 liters of resin for each piece of printing and to empty the remaining resin is too troublesome at the end of the production. In this case, the control of the preliminary and final stages becomes very difficult.

In order to correct these errors, the device was revised and the changes made for the revision are as follows.

- ✓ In order to prevent the wobble that occurred during production, the bearing shafts were doubled to be on both sides of the screw shaft. Later, in order to integrate these bearing shafts into the system, a new part was produced in which the movable screw was also supported. Finally, a new part was designed and produced to fix the motor and mounted on the printer. All of these parts were produced using ABS filament from our own FDM type printer.
- ✓ Teflon coated zinc plate was used instead of aluminum 5083 to prevent reflections on the platform. In order to adapt the platform to the device, the plate was bent from 2 places and made into a z geometry.
- ✓ Instead of the large chamber, 500 pieces of containers with dimensions of 110x150x50 mm were supplied. The bellows test bench was used to adjust the position of the chamber in the z-axis. In this way, it was possible to produce by using lower amounts of resin, and wastage was prevented since the resins to be used in further studies would have a higher cost. In addition, since the chambers are disposable, the cleaning of the gellings formed on the chamber wall due to radiation during production has also come to an end.

It was observed that the lateral surfaces were smooth and the dimensional accuracy was high for the specimens printed after the revision. The final state of the DLP printer after revision is as shown in the Figure 2.17.

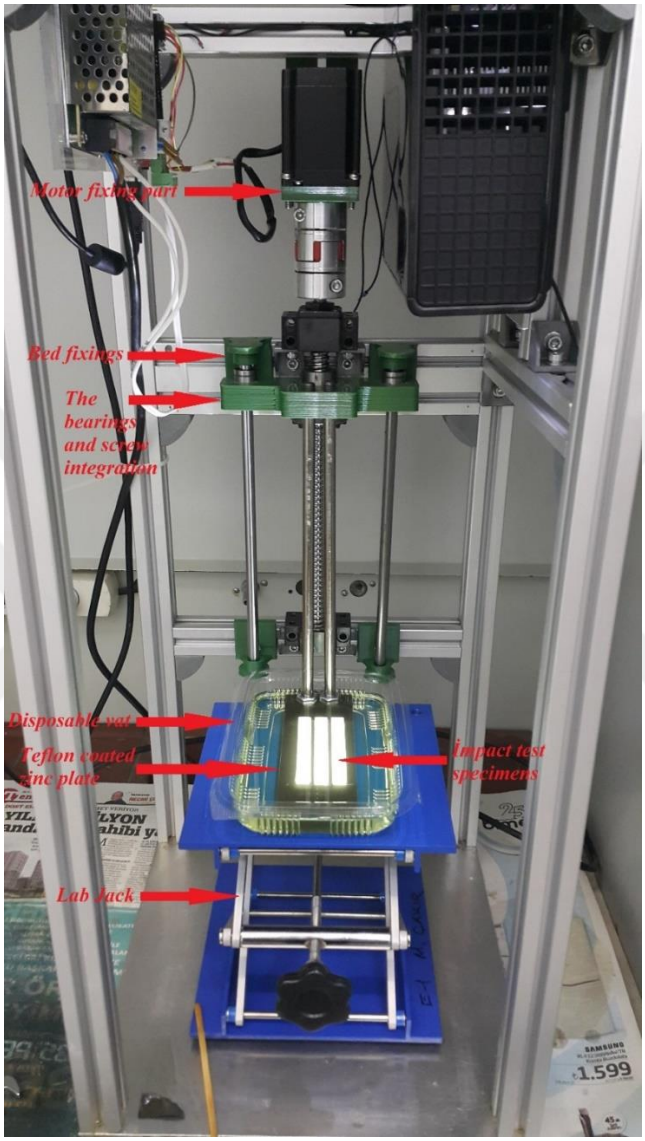


Figure 2.17 Revised DLP printer

2.5.1 Dimensional and surface control of the test specimens

After the last revision of the DLP printer, the geometries and surface roughness of the produced samples were measured to check the accuracy of the programming and calibration and their readiness for printing. Width, length and thickness measurements were made with an electronic caliper for geometric control, while scanning was made using a Mahr® Marsurf PS10 model mobile device for surface roughness. The measuring

range of the device is 350 μm and the scanning path is 1.5 mm. Roughness measurements were made from the lateral surfaces of the impact samples and the top surfaces of the tensile samples. The reason for choosing impact samples for the lateral surfaces is that they consist of more layers since their thickness is 5 mm, and more layers increase the probability of error.

2.6 Nanocomposite Production and Examination Process

After the geometric and surface controls of the device were confirmed to be correct, nanocomposite studies were started. 3-(methacryloyloxy) propyl trimethoxysilane, sulfuric acid (H_2SO_4), phosphoric acid (H_3PO_4), potassium manganate ($KMnO_4$), ethanol (C_2H_5OH), hydrochloric acid (HCl), were supplied from Sigma-Aldrich natural graphite flake supplied from Morgan Advanced Materials Turkey. Epoxy acrylate (Bis-GMA) and reactive solvent (HDDA) were supplied from SunChemical and photoinitiator (IRGACURE 819®) was supplied from BASF Turkey.

2.6.1 Synthesizing graphene oxide and preparing UV curable resin

Graphene oxide was synthesized by Tour method which is an advanced Hummers' method. In the Tour method, a higher yield product is obtained compared to the hummers method. Additionally in contrast to Hummers' method, the Tour method does not generate toxic gas and the temperature is easily controlled. Therefore, this method was chosen for graphene oxide production [120]. For this purpose, 360 ml. H_2SO_4 and 40 mL. H_3PO_4 were combined in 1 liter 3-necked flask and 3 gr. graphite flake and 18 gr. $KMnO_4$ were added after getting a homogenous mixture. The temperature of the reaction was raised over 25-40 ^{0}C because of exothermic case. After 1 hour, reaction temperature was raised to 50 ^{0}C and the reaction was completed by stirring at this temperature over 12 hours by a magnetic stirrer at 200 rpm. Solution was poured on ice which prepared by distillate water after it was cooled down to room temperature. 3 ml. of 30% H_2O_2 was added in solution at iced setting. The mixture was leached by the polyester filter and precipitation was provided with hydro-extraction at 8000 rpm for 30 minutes, solution over mixture was decomposed by discharging. Remained solid was washed with 200 mL ethanol at 3 times repeatedly after the washing process with 200 ml 30% HCl. Ethanol was added again into the mixture and it was leached again with polyester filter. Finally,

the mixture was made hydro-extraction at 8000 rpm in 30 minutes. Flow chart of the process is given at Figure 2.18.

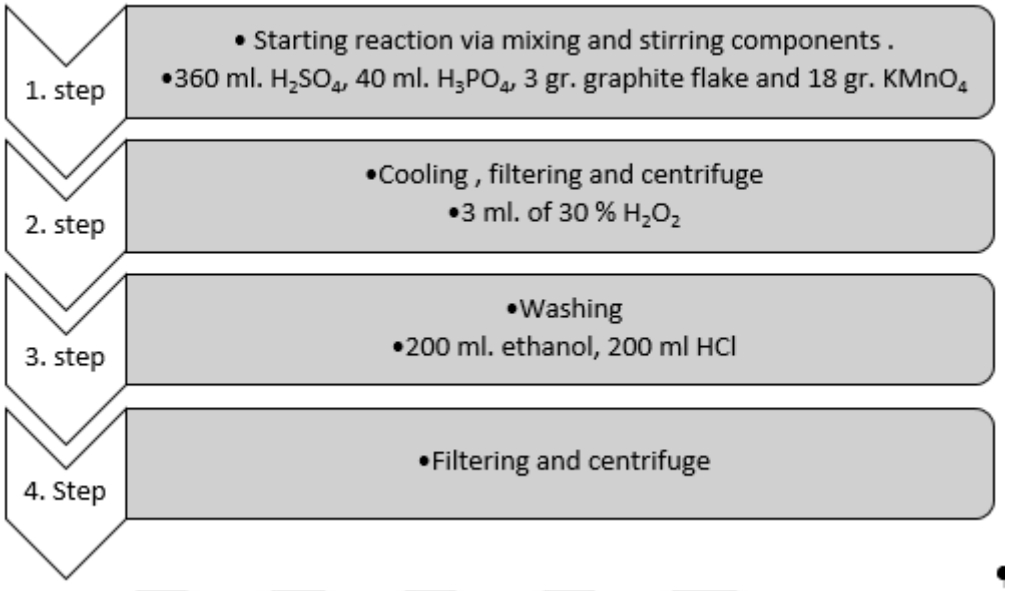


Figure 2.18 Flow chart of graphene oxide synthesizing via Tour method

500 ml Bis-GMA and 500 ml HDDA were mixed by a magnetic stirrer at 500 rpm for 20 mins. Following, photo initiator IRGACURE 819® was added to mixture as weight percentage of 0.5% and continued to stirring until getting a limpid outlook (approximately 1 hour). HDDA was used as reactive solvent to decrease resins viscosity due to easy flow on the printing table and easy print with SLA. With UV light, double bonds of phosphorus at photo initiator broken and start curing reaction.

2.6.2 Surface modification of the graphene oxide nano particles

3-(methacryloyloxy) propyl trimethoxysilane (MEMO) was added into distilled ethanol. PH value was fixed at 4.5 by paratoluen sulphuricacid. Besides stoichiometric ratio “r” was equal to 3 which means distillate water was added at 3 steps. The mixture was stirred first 8 hours at room temperature and then 2 hours at 60 0C. Thereafter mixture was cooled down to room temperature and made hydro-extraction at 5000 rpm. in 25 minutes. Inert 3-(methacryloyloxy)propyl trimethoxysilane was removed by the washing process from modified graphene oxide. The sample was taken and dried into vacuum evaporator at 100 0C over 24 hours. According to this process weight percentages of solid GO nanoparticles at solution were detected. Modified GO was added into mixture that

consisted of 50% Bis-GMA and 50% HDDA with rate of 0.05%, 0.1%, 0.15%, 0.20% and 0.25% weight percentages. UV photo initiator was added to resin and it was made ready for SLA type printing process (Figure 2.19).

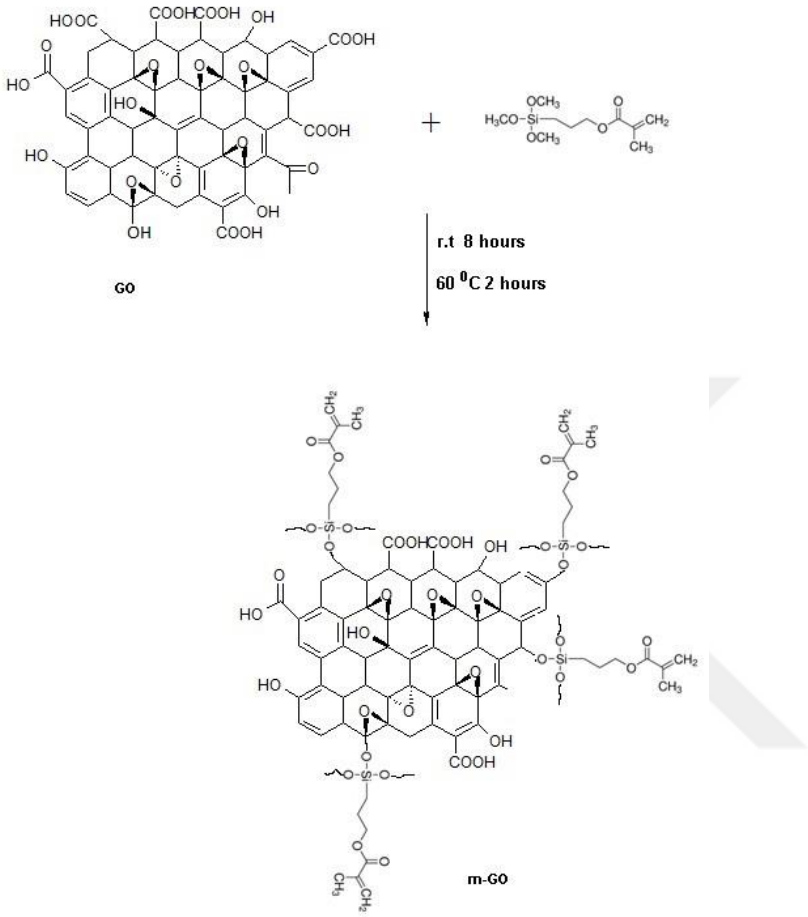


Figure 2.19 Schematic view of surface modification for GO

Surface modification process was applied for GO nanoparticles due to increase acrylate end groups as seen in Figure 2.19. Thus, the bonds between GO and epoxy acrylate formed more smoothly during curing.

2.6.3 3D printing process

3D models of test specimens were designed with SolidWorks by Dassault Systèmes and transferred to the printer by Creation Workshop software. After the printing, specimens were post-cured by Raycon UV System Mercury Lamb Conveyor (speed was 5 min/mm at 150 kV) with a short wavelength (200 nm) to reduce unbound acrylate functional groups and remove free reactive solvent HDDA.

Non-modified GO and surface modified GO nanoparticles were added into UV curable resin with significant rates of weights for printing process. Specimens were printed of 0.1 mm thickness for each layer. Resolution of the image was 1920x1200 and gained from DLP projector. Size of building area was 200x120 mm. The building table was lifted 50 mm down 49.9 mm up at every layer of curing process to get resin properly on model for next layer. Curing time was 7 seconds for first 3 layers at the bottom and 3 seconds for remains. The transparency and brightness which, cannot be obtained with classic moulding techniques, were obtained by this method. Opaque outlook was observed with the same composites of the mixture when moulded in a die at former studies. This difference between them is due to the amorphous and semi-crystalline situation. While the chemical bindings of the chains occur at the same time for molding technique, same bindings occur intermittently in the SLA method. Therefore, polymer chains cannot form regularly in the structure. As known, amorphous materials have better light transmittance than crystalline materials [121]. Some of printed specimens are given in Figure 2.20.



Figure 2.20 Printed tensile and impact tests specimens

2.6.4 Mechanical and morphological investigations

Tensile tests occurred with Shimadzu tensile test machine at 5 mm/min deformation speed. Video extensometer was used to measure elongation. Tensile test specimens were prepared according to ASTM D638-02a type-IV (test specimens for polymer materials) as shown in Figure 2.21. Izod impact test was conducted by Zwick B5114.30 with 5.4 J Izod striker. Hardness tests were made with Zwick model and Shore D type hardness

machine. Standards of hardness are ASTM D2240, DIN 53505 and ISO 868. Tests were repeated three times for each samples and the average of three was calculated.

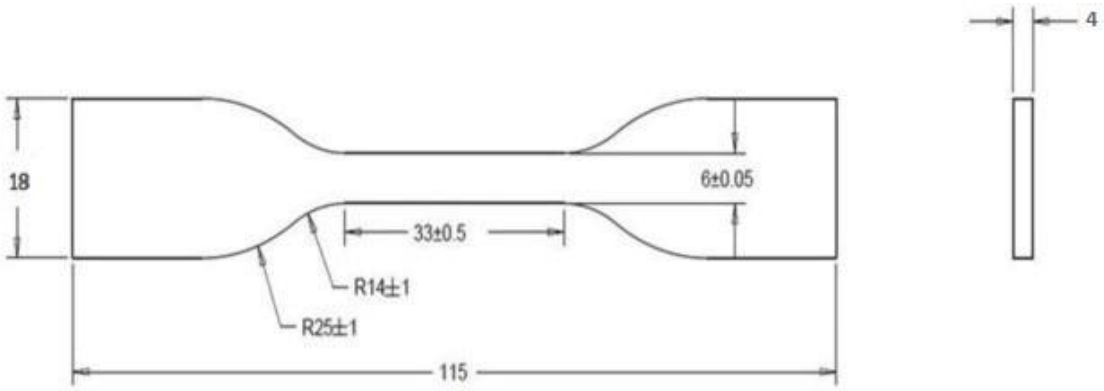


Figure 2.21 Tensile test specimen dimensions (ASTM D638-02a type-IV)

Transform infrared spectroscopies were occurred by FT_IR-4700 type-A model spectroscopy device. Finally, SEM images were get with different zoom rates to view GO nanoparticles distribution at nanocomposite samples. Also, SEM images were captured from fracture surfaces of impact test samples to examine fracture behaviour.

2.7 Synthesizing and Testing of the Biocompatible and Flexible Photopolymer

Three different compositions were tried in order to synthesize the flexible and biocompatible resin and make it suitable for production in a DLP printer OH-Terminated Polybutadiene (Krasol nn22) and Hexamethylene Diisocyanate (Desmodure H) were used as the construction material of the resin in the first 2 studies. However, when the solvents in it were removed at the end of the synthesis, Krasol 2200 had a very dense viscosity like honey, while Desmodure H became a foamy structure. These structures were not dissolved in BisGMA and photocurable resin could not be obtained at the desired viscosity. Finally, in the study with hydroxyl-terminated polydimethylsiloxane, a more fluid and liquid consistency synthesis was obtained and the obtained material was dissolved with a mixture of BisGMA and HDDA and a photoinitiator to obtain a resin. Tensile and impact specimens were produced with DLP printer using the synthesized resin. After examining the morphological features, biocompatibility tests were also performed.

2.7.1 Synthesizing of Krasol nn22

Butadiene (Krasol) was mixed with THF until dissolved in it, respectively, in a three-necked flask. Then, acryloyl chloride was added to the mixture at room temperature with the help of a dropping funnel and mixing was continued. The reaction temperature was increased to 80 °C and mixture was stirred for 3 hours. TEA was used as a catalyst in the reaction. When the synthesis was completed, it was kept at 90 °C for 2 hours using a rotary evaporator to remove THF from the solution. Since the removal was insufficient, the evaporator temperature was increased to 100 °C and the process was continued for 1 more hour. It was determined that the foamy consistency of the solution could not be removed and THF did not disappear. For this reason, it was taken from the evaporator and dried in the oven, and it was kept in the oven at 110 °C for 16 hours for drying. Since the resin obtained as a result of the drying process in the oven has a very high viscosity and honey consistency, it was decided that it was not suitable for use in DLP printers and Desmodure H synthesis was started. The reactions and proses schema are given in the Figure 2.22.

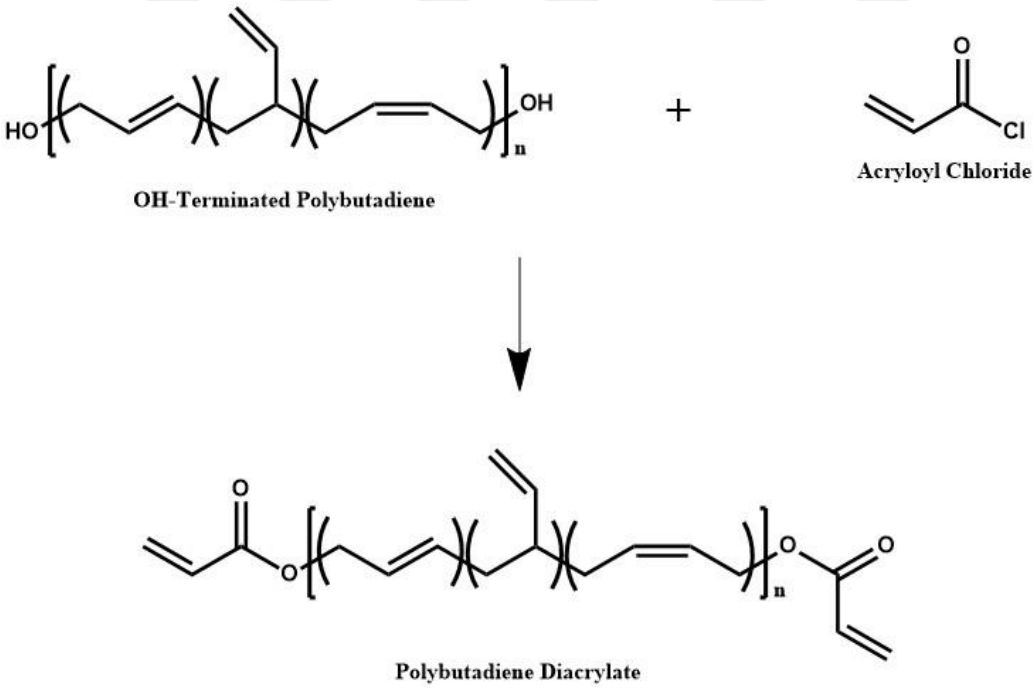


Figure 2.22 Synthesizing reactions of Krasol nn22

2.7.2 Synthesizing of Desmodure H

To initiate the reaction, isocyanate, THF as solvent, and recycler were added to the 250 ml three-necked flask, respectively. Then, nitrogen gas was introduced into the mixture and mixed under an inert atmosphere until a homogeneous solution was obtained. After obtaining a homogeneous image, HEMA was dropped into the solution for 1 hour with the help of a dropping funnel. T-12 (dibutyltindiluent) was used as catalyst in the reaction. The mixture was kept constant at 45°C and stirred for 3 hours. After the synthesis was finished, a rotary evaporator was used to remove THF from the solution. As a result of the foamy structure of the resin obtained after the removal, the synthesis was not found suitable for use in the DLP device, and acrylate functional PDMS synthesis was started. Reactions and prosses are given in Figure 2.23.

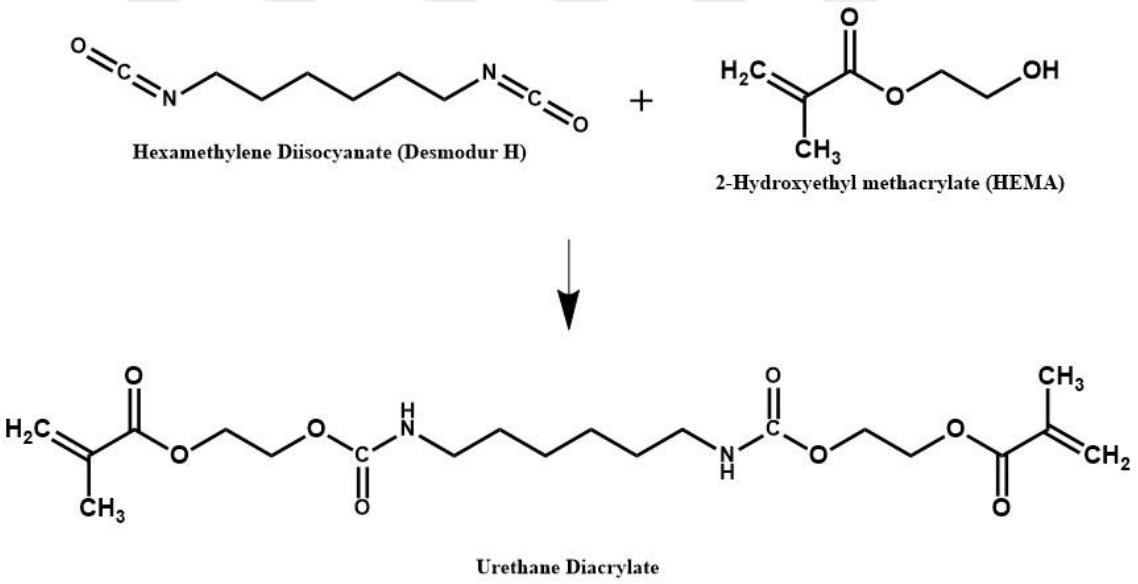


Figure 2.23 Synthesizing reactions of Desmodure H.

2.7.3 Synthesizing of AF-PDMS

HT-PDMS, reactive solvent and 1% rate of weight triethylamine were combined in 1 liter 3-necked flask and dropping funnel contained acryloyl chloride was connected at one neck of the flask for adding to the mixture drop by drop until reaction. Reaction was performed at 80 ^{0}C for 3 hours. Reaction confirmed by FT-IR Spectroscopy (Figure 2.24).

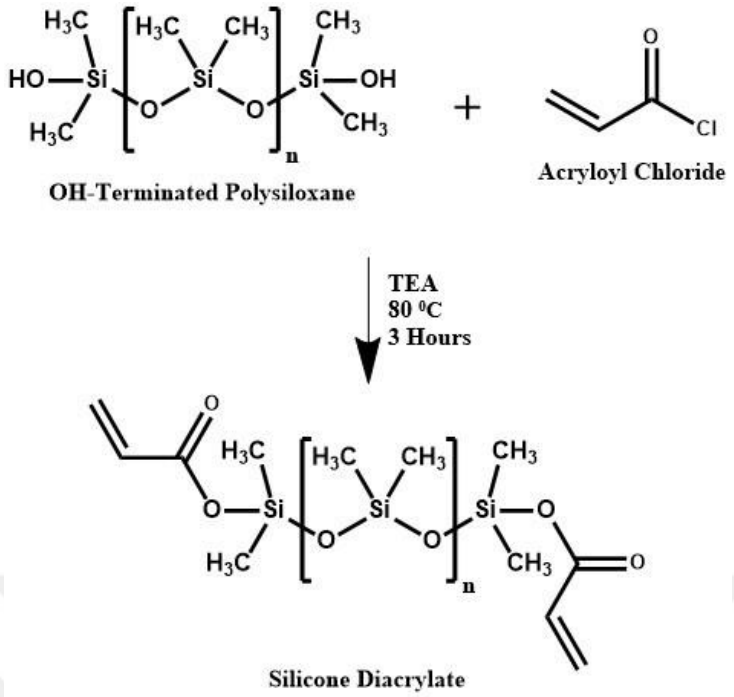


Figure 2.24 Synthesizing reactions of AF-PDMS

Materials used for the synthesizing process of the AF-PDMS based photocurable resin are given below;

- Bisphenol A-glycidyl methacrylate (Bis-GMA): This material also known as "epoxy acrylate" is the main structure of test specimens. Synthesized acrylate functional PDMS was added with different wt% as 20, 40, 60 and 80, into the Bis-GMA/HDDA to prepare UV curable DLP resin. Bis-GMA is a quite rigid material and it has an important usage as dental filling material for this reason [122].
- Hydroxyl-terminated polydimethylsiloxane (Tegomer® H-Si 2315): Hydroxyl-terminated polydimethylsiloxane (HT-PDMS) is the main structure of synthesized acrylate functional PDMS.
- Acryloyl chloride: Acryloyl chloride is reacting with HT-PDMS and turns PDMS to acrylate functional and UV curable.
- Triethylamine (TEA): This is the catalyzer of the reaction between HT-PDMS and Acryloyl chloride.
- Hexanediol diacrylate (HDDA): HDDA is the reactive solvent of the photocurable resin. It was decreased viscosity and also structure soluble and no need to remove from synthesized resin.

- Bis(2,4,6-trimethylbenzoyl)-phenylphosphineoxide (Irgacure® 819): Irgacure® 819 is a versatile photo initiator for radical polymerization of unsaturated resins upon UV light exposure. Single bonds around the phosphor opens with UV light and react to other end groups.

2.7.4 DLP printing of the AF-PDMS test specimens

In this study AF-PDMS were added into UV curable resin which is contained Bis-GMA 50%, HDDA 50% and Irgacure® 819 1%, with significant rates of weights for printing process and specimens were printed of 0.1 mm thickness for each layer. Resolution of the image of UV light was 1920x1200 and gained from DLP projector. Size of building area was 200x120 mm. The building table was lifted 50 mm at every layer curing process to get resin properly on model for next layer.

2.7.5 Mechanical tests of the AF-PDMS

Tensile test, abrasion test and hardness measurement were performed for mechanical characterizations. Tensile tests were occurred with Zwick® model tensile test machine at 5 mm/min deformation speed. Contacted extensometer was used to measure elongation. Tensile test specimens were prepared according to ASTM D638-02a type-IV (test specimens for polymer materials). Hardness tests were made with Zwick® model and Shore hardness tests was performed as a Shore A and Shore D scale. Standards of hardness are ASTM D2240, DIN 53505 and ISO 868. Abrasion tests were occurred by Devotrans® model abrasion test device. Abrasion tests were applied for two different rates of PDMS contained specimens as 20% and 40% due to flexibility of higher rates of PDMS contained samples were obstacle for abrasion. The test was performed at 100, 250 and 500 cycles with a load of 250 grams. Finally density measurement was occurred for all different rates of PDMS contained samples.

2.7.6 Thermal test and FT-IR analysis of the AF-PDMS

Transform infrared spectroscopies were occurred by FT-IR-4700 type-A model spectroscopy device.

Differential Scanning Calorimeter (DSC) analysis was performed for four different samples to investigate the effect of AF-PDMS ratio on glassy transition temperature.

2.8 Biocompatibilitiy Tests

Since one of the aims of the thesis is to produce a flexible implant material, it is very important that the printed parts are biocompatible. Support was received for the aforementioned studies due to the lack of sufficient infrastructure to carry out the tests and the lack of sufficient experience in determining biocompatibility. İstanbul Medical Faculty of the İstanbul University, Physiology Department faculty members supported the tests.

2.8.1 MTT cytotoxicity assay

3T3 mouse embryonic fibroblast cell line was obtained from American Type Culture Collection (ATCC). Cells were cultured in Dulbecco's modified Eagle medium (DMEM, Gibco) with 10% Fetal bovine serum (FBS, Gibco) and 1% penicillin/streptomycin in a humidified 5% CO_2 incubator, maintained at 37ºC. When the cells reached 80% of confluence they were trypsinized with 0.25% Trypsin-EDTA for passaging and seeding each time. The confluent cells were used in cytotoxicity tests.

Firstly, samples are sterilized with UV for 4 hours. Conditioned medium was prepared to understand any possible toxic effect induced by possible ionic leach-out of product from the samples into the medium. For this aim, 5 ml fresh medium was added in tubes with a tested material, which were kept in the incubator. After 3 days the conditioned medium was collected and later used in cytotoxicity tests. MTT assays were performed in 96-well plates. 3T3 cells (about 105cells per well) were seeded with conditioned medium and incubated for 72 hours. Cell viability was measured by determining mitochondrial NADH/NADHP–dependent dehydrogenase activity, which resulted in the cellular conversion of the 3-(4, 5-dimethylthiazol-2-gl)-5-(3-carboxymethoxylphenyl)-2-(4-sulfophenyl-2H) tetrazolium salt into a soluble formazan dye. After 3 days, and 10 µl 3-{4, 5-dimethylthiazol-2yl}-2,5-diphenyl-2H-tetrazolium-bromide (MTT- 5mg/ml-Sigma) solution was added to each well. Cells were incubated at 37ºC for 3-4 h MTT was taken up by active cells and reduced in the mitochondria to an insoluble purple formazan granule [123]. Subsequently, 50 µl of supernatant was discarded, and the precipitated

formazan was dissolved in dimethyl sulfoxide (100 μL per well), and optical density of the solution was evaluated using a microplate spectrophotometer (Kayto RT-210^{0}C) at a wavelength of 570 nm. Used GraphPad Prism to calculate to cell viability.

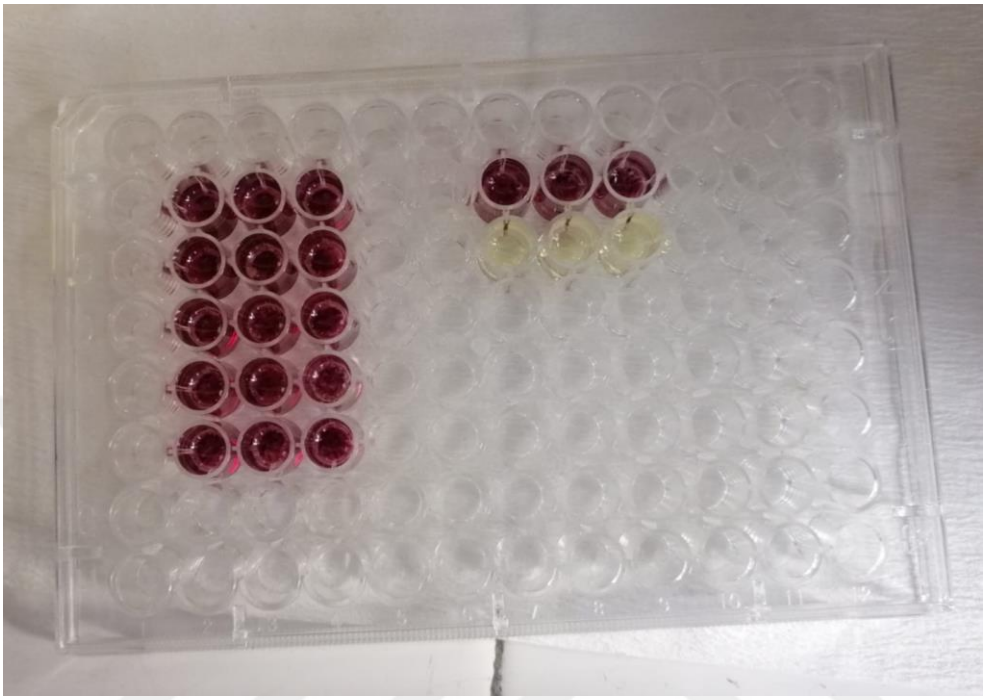


Figure 2.25 Prepared samples for cytotoxicity measurement

2.8.2 SEM protocol

Resin and PDMS materials were sterilized with UV for 4 hours. Samples were placed in 6-well plates. 3T3 cells (about 6x105 cells per well) seeded over this materials with 3 ml DMEM and incubated 24 hours. After the incubation, medium removed and materials washed with PBS (phosphophate buffer solution). Samples fixed with 3% glutaraldehyde solution about 1 ml each well for 1 hour. Then samples washed again with PBS. For the dehidration of samples, its incubated with increased alcohol series (30%, 50%, 70%, 80%, 90%) 10 minutes per step and 30 minutes 96% last step (Figure 2.26). They were dried and samples observed in Scanning Electron Microscope.

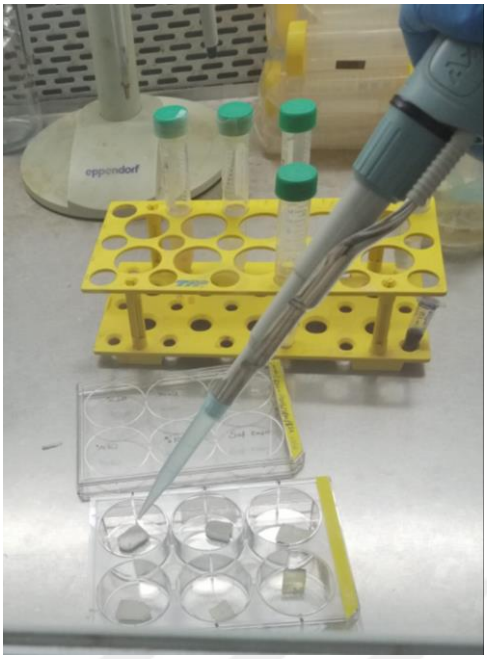


Figure 2.26 The process of seeding cells on samples for SEM images

3 RESULTS AND DISCUSSION

The results were gathered under four main headings. First, after the revision of the printer, the dimensional and surface sensitivities of the printed parts were finalized. Secondly, the mechanical and morphological test results of the composite test specimens were examined. Then, the test results of the parts produced by adding AF-PDMS resin were investigated. Finally, the biocompatibility test results of AF-PDMS added samples were examined.

3.1 Dimensional and Surface Roughness Results of Test Specimens

The measurements for the geometric accuracy control of the device in printing are given in the Figure 3.1. Percentage deviations according to the measurements taken from the tensile samples were calculated as 0.29% in the length of the sample, 0.33% in the width of the heads held by the jaws of the tensile test device, 0.79% in the width of the rupture region and 1.75% in the thickness. The average of the deviations in width and length was determined as 0.47% (Figure 2.21).



Figure 3.1 Dimensions of the tensile specimens after production

The roughness measurement values and graphics taken from the lateral surfaces are given in the Figure 3.2 figure. The average of the R_a (average roughness) value was calculated as 1.015 µm, and the average of the R_z (maximum roughness depth) value was calculated as 3.341 µm.

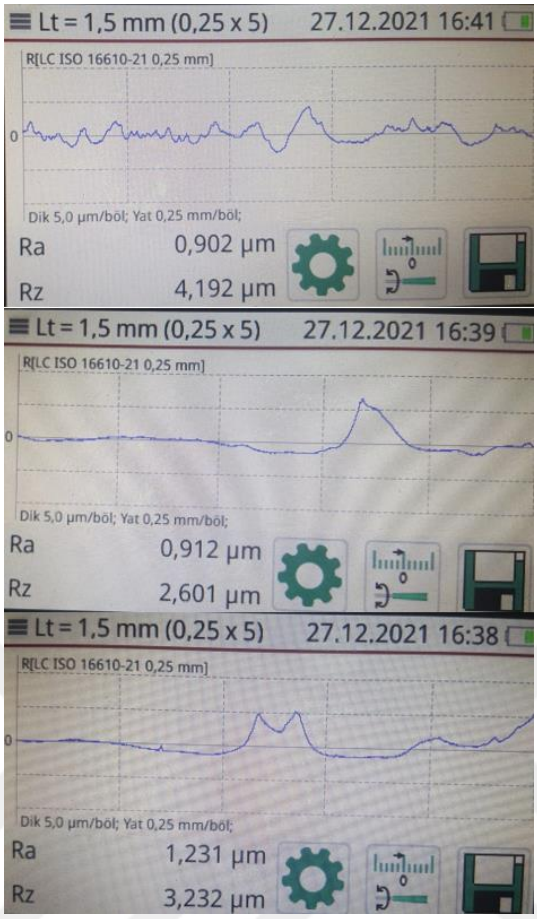


Figure 3.2 Roughness measurement results from the lateral surfaces of impact samples

The roughness values of the upper surface of the tensile specimen were measured as R_a=0.079 µm and R_z=0.360 µm (Figure 3.3).

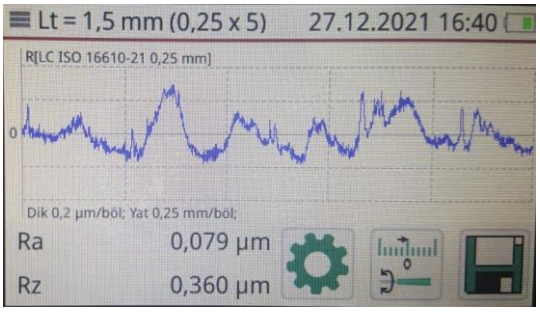


Figure 3.3 The result of the roughness measurement obtained from the upper surface

3.2 Mechanical and Morphological Test Results of Nanocomposite

Tensile tests, impact tests and hardess tests were applied for mechanical properties. FT-IR and SEM analysis were applied for morphological properties.

3.2.1 Tensile test results

When Figure 3.4 and Table 3.1 are examined, for non-modified GO, it is seen that tensile strength is not been directly proportionate to increasing GO ratio. These results do not show similarity with investigations in the literature [124]. Increasing strength and elongation is observed with increasing bond of GO at studies. Usually, strength increment in traditional materials is based on limiting the movement of sliding bands. Therefore, the decrease in the strain results causes an increase in strength [125]. When the tensile results of 5 different specimens are examined, a significant inclination is not discovered at stress values. For example, stress is increased 11% with increasing wt% of GO from 0.05% to 0.1%, but decreased when the wt% of GO value increasing up to 0.15%. Alterations of the stress values are similar with afterwards specimens which are contained higher GO. Strain values show us the same situation with the stress. This circumstance could be explained by the disordered structure of non-modified GO nanoparticles. Because of the disordered structure, non-modified GO particles were not bonded smoothly with polymer resin. Eventually, wt% for non-modified GO particles is lost its importance because of random distribution at strength and strain results. They are not increase or decrease relative to the wt%. Whereas increasing stress and elongation results are gained with increasing weight percentage of surface-modified GO. These results are satisfied in the literature rather than non-modified GO. With increasing surface-modified GO wt% up to 0.25, both stress and strain values are increased remarkably, such as 39% for stress and 153% for strain in comparison with pure resin. The most stunning results are obtained between surface-modified and non-modified GO added nanocomposites by increasing maximum stress up to 73%. In comparison with pure epoxy acrylate specimens, surface modified GO containing nanocomposites are shown higher stress and strain results.

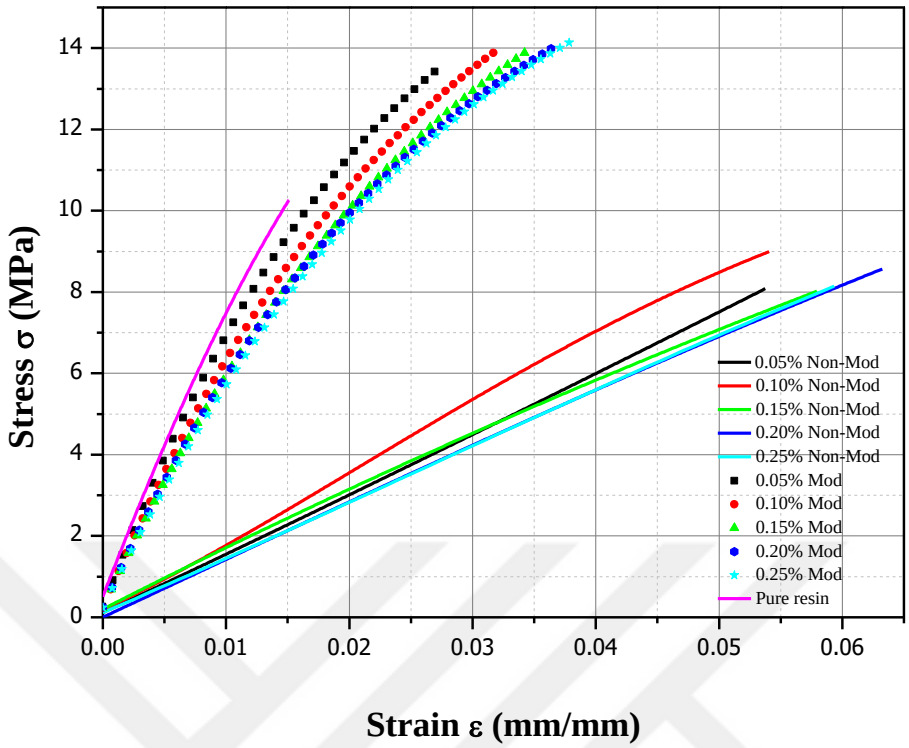


Figure 3.4 Comparison of the tensile test results for surface modified and non-modified GO

The functionality of the surface-modified GO flakes is over 2. Therefore, there is a partial cross-linking in nanocomposites with surface-modified GO. As the crosslinking increases in the structure, the strength values of the material increase. These crosslinking points prevent the polymer chains from slipping on each other and form locking points. Meanwhile samples were hardened and strain values were decreased due to obstructs of these lock-up mechanisms. Moreover, due to surface modification, the smoothness and higher rate linkage of GO particles was caused the correct proportion to be established between the GO rate change of the samples and their mechanical properties. Finally, non-modified GO additive nanocomposites were given irregular results and regardless of the GO wt%, because of the particles with low amount of radical end groups were acted as contaminant in the material and also distrupt the structure of the epoxy acrylate [126, 127].

Table 3.1 The results of the tensile test

	Non-Modified GO		Surface Modified GO	
wt% of GO	**Max. Stress (MPa)**	**Max. Strain (mm/mm)**	**Max. Stress (MPa)**	**Max. Strain (mm/mm)**
Pure	10.26	0.015	10.26	0.015
0.05	8.08	0.053	13.42	0.027
0.10	8.99	0.054	13.94	0.032
0.15	8.02	0.058	13.95	0.034
0.20	8.57	0.063	14.05	0.037
0.25	8.14	0.059	14.24	0.038

3.2.2 Impact and hardness tests results

As seen in the Izod impact test results in Figure 3.5, a decreasing was observed for test results against increasing wt% of GO. The situation of decreasing impact strength according to rising elongation could be explained by the mechanism of sliding GO flakes during deformation [128]. Due to this mechanism, the material is deforming easily but impact strength is low for sudden forces.

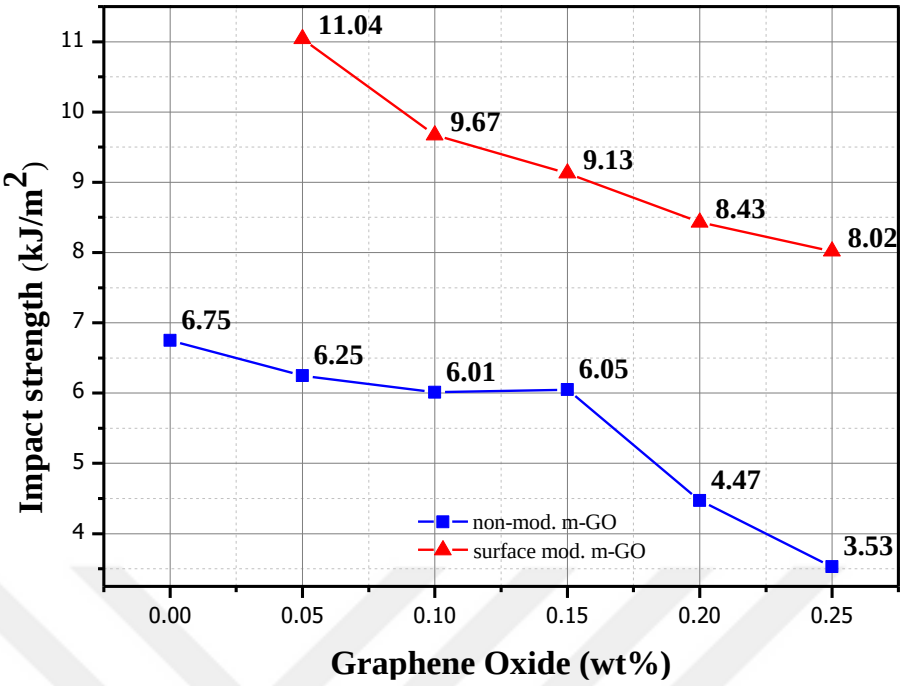


Figure 3.5 Izod impact test results for non-modified and surface modified GO.

Despite of increment on elongation, increasing was obtained with a rising amount of GO in the mixture. Whereas the shore-D hardness value of pure epoxy acrylate was 56.7, including of 0.25% GO epoxy acrylate resins hardness value was raised to 64.3 as seen in Figure 3.6.

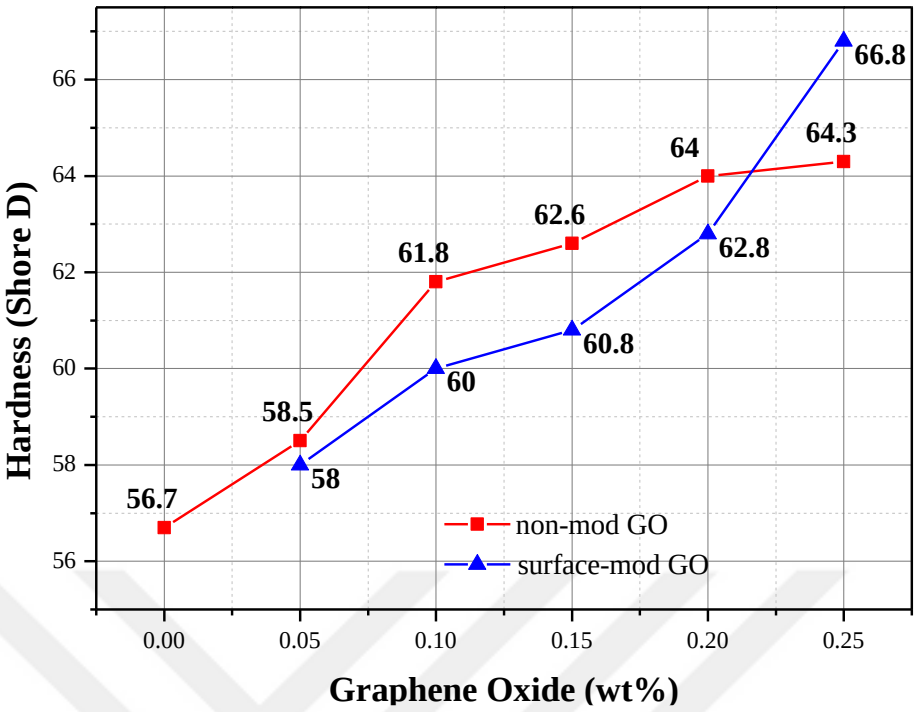


Figure 3.6 Shore D hardness test results for non-modified and surface-modified GO

3.2.3 FT-IR analysis

FT-IR spectra of pure graphene oxide particle and sur-mod Graphene oxide particle are shown in Figure 3.7 and Figure 3.8. In the FT-IR spectrum, it is observed that GO has a strong and broad OH stretching vibration band at 3310 cm^{-1}, carboxyl C=O stretching band at 1737 cm^{-1}, OH deformation vibration band at 1405 cm^{-1} and CO stretching vibration at 1083 cm^{-1} because of extensive oxidation. This results indicate that GO is successfully obtained [129].

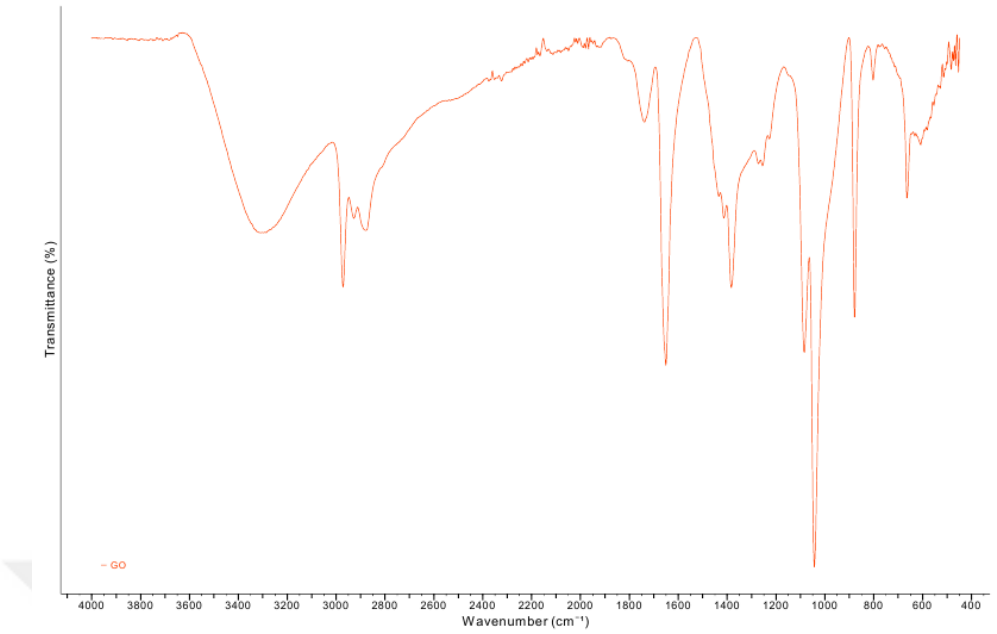


Figure 3.7 Non-modified graphene oxide

After the reaction of GO with MEMO, the prepared m-GO broaden two absorption bands at 2873 cm^{-1} and 2971 cm^{-1} corresponding to the symmetric and asymmetric stretching vibration of CH_2 groups. The absorption bands in the region of 1122 cm^{-1} and 1032 cm^{-1} are attributed to Si-O-Si and Si-O-C stretching vibrations [130].

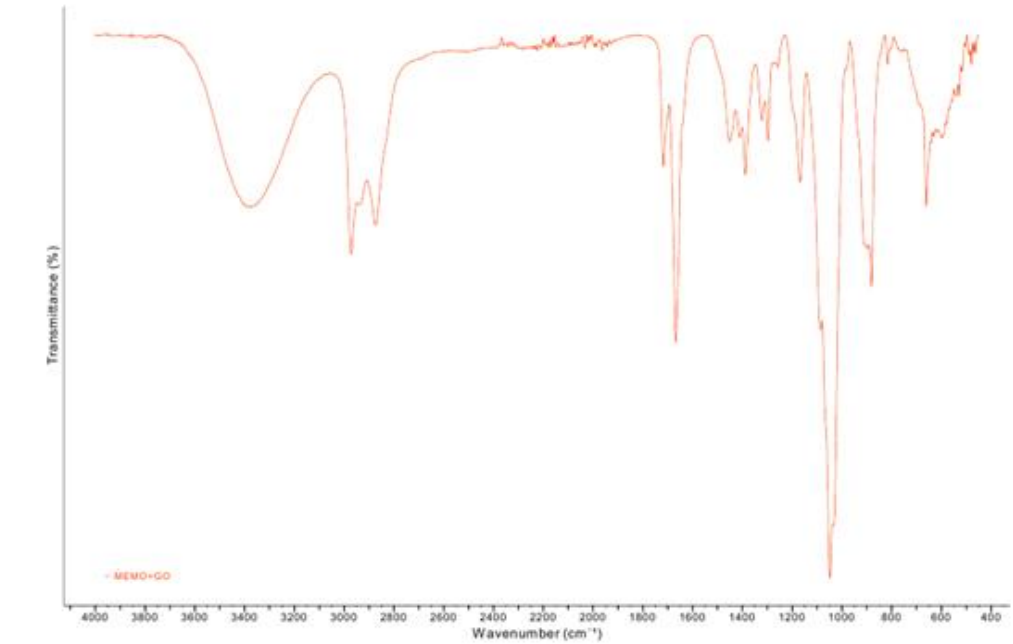


Figure 3.8 Surface modified graphene oxide

Also, the absorption bands around 2957 and 2894 cm^{-1} are attributed to stretching vibrations of alkyl groups (CH_3 and CH_2). The bands close to 1720 and 1637 cm^{-1} are associated to the stretching vibrations of C=O and C=C groups respectively. The absorption bands located at 1320 and 1299 cm^{-1} are assigned to the C−O−C bonds and wagging vibration of CH_3 groups of the MEMO molecule. These indicate that MEMO is successfully bonded to the GO surfaces [131].

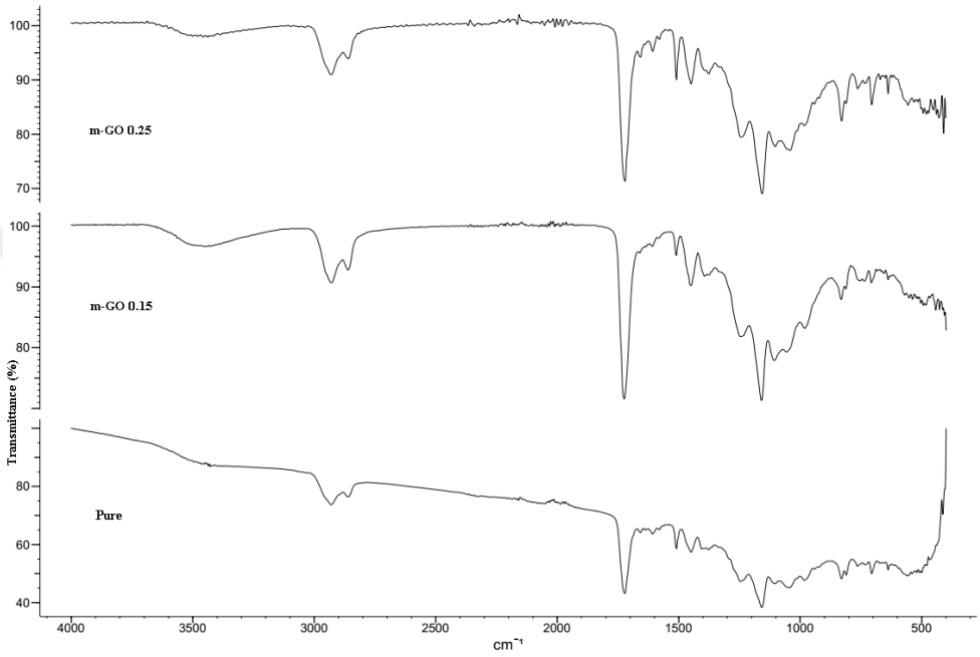


Figure 3.9 FT-IR spectrums of the cured polymers

The FT-IR spectra of two different wt% GO and pure (only BisGMA/HDDA) samples are given in Figure 3.9. Vibrational according to FT-IR spectra bands at 980 and 1450 cm^{-1} that belong to O- CH_3 bending and stretching deformation of MEMO. This band is not seen in pure structure bands. 1724 and 1245 cm^{-1} that are assigned to stretching of C = O groups, 1159 cm^{-1}: C – O stretching band, 1450 cm^{-1}: CH_2 bending band. The absorption bands in the region of 1122 cm^{-1} and 1032 cm^{-1} are attributed to Si-O-Si and Si-O-C stretching vibrations. These Si-O-Si bands are not observed in pure structure [132, 133].

3.2.4 SEM examinations

Scanning electron microscopy (SEM) examinations of test specimens that include two different wt% of surface modified graphene oxide (0.05% and 0.15%) are given in Figure

3.10. Homogeneous distribution is observed at SEM captures and there is no aggregation any surface of the samples. In the images, we can say that the samples do not show brittle fracture that breaks in a straight line. Fracture includes plastic deformation pause lines at nearby brittle regions. As a known plurality of the plastic deformation areas are proof that this material will be fractured without instantaneous ruptures. Image (a) and (b) show us the 0.05% surface-modified GO contained samples with different zoom rates. Intensive plastic deformation areas are seen in these images which are locked instantaneous ruptures. Some of them are circled at (a) and (c). On the other hand when (c) and (d) images, which are photos of 0.15% surface-modified GO contained samples, are examined less plastic deformation areas are observed. Samples containing 0.05% m-GO are more disintegrated, whereas samples containing 1.5% m-GO were not. As the amount of surface-modified GO increases, the number of nano plates increases and leads to an integrated breakage in fracture.

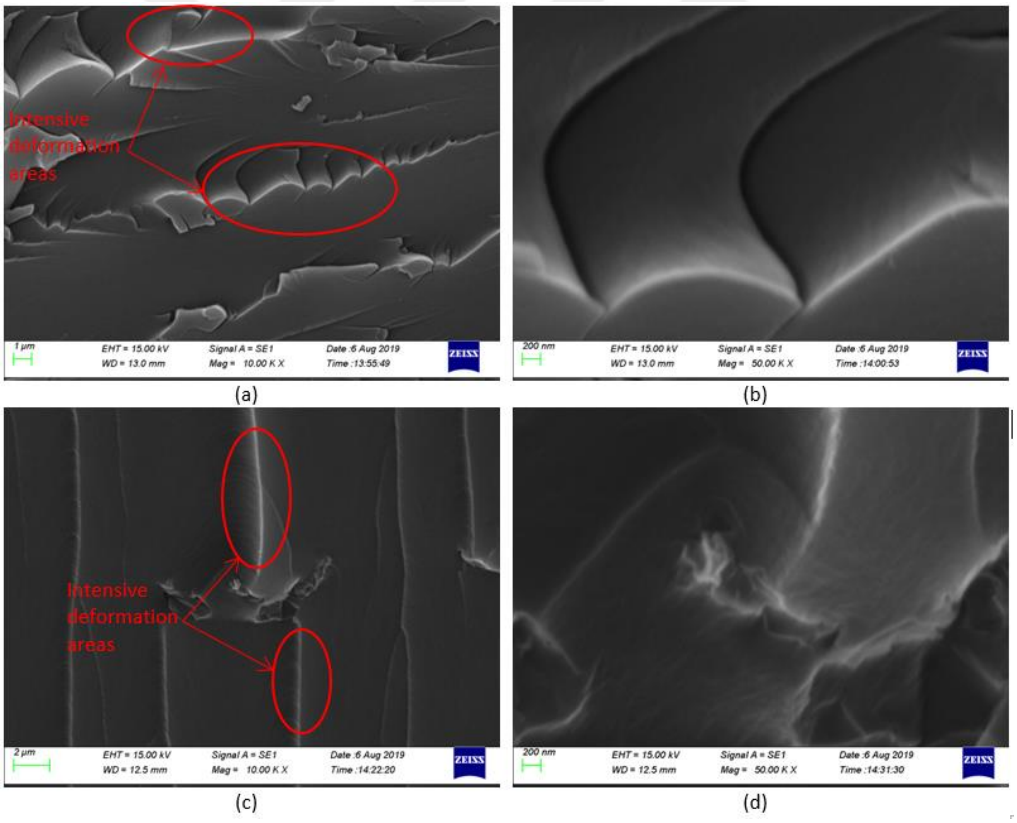


Figure 3.10 SEM images of fracture surfaces for surface modified GO contained nano composites (a) 1000X zoomed images of 0.05% sur-mod GO contained samples (b) 5000X zoomed images of 0.05% sur-mod contained samples (c) 1000X zoomed images of 0.15% sur-mod GO contained

In addition, grain size and distributions of GO nanoparticles in polymer based nanocomposite were shown with SEM shots at Figure 3.11.

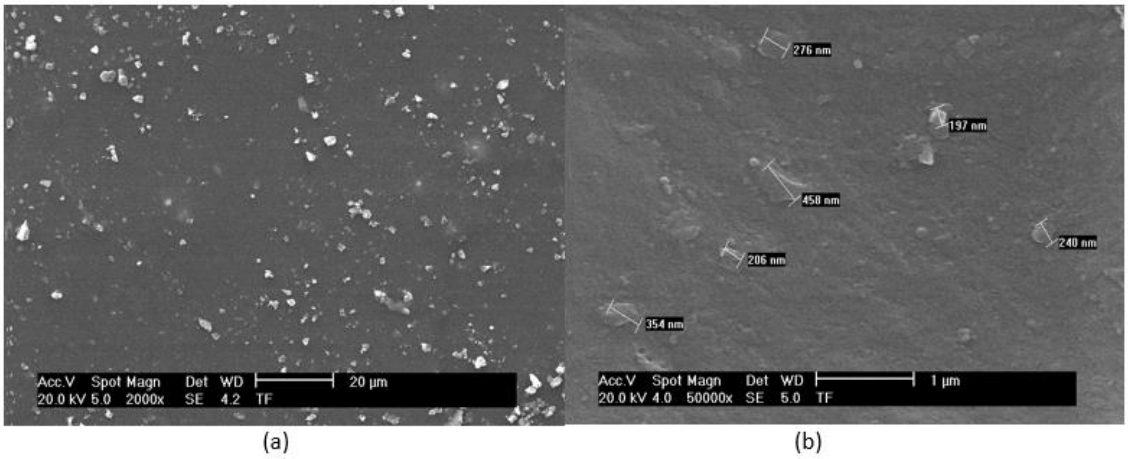


Figure 3.11 Demonstration of grain distributions (a) and size (b) of graphene oxide nano particles with SEM shots.

3.3 Results of the AF-PDMS

Tensile, hardness, density and abrasion tests were occurred for mechanical properties. DSC measurement was apllied for thermal characterizations. FT-IR and SEM analysis are occurred for morphological properties.

3.3.1 Tensile test results

Experiments were performed in three repetitions from each wt% sample and averaged. When the maximum stress values given in the Figure 3.12 were examined, it was observed that a decrease occurred with increasing AF-PDMS wt%. This result can be expected as it is known that AF-PDMS, which is a silicon-based synthesis, has a flexible structure. This result also indicates a mountainous binding of AF-PDMS and BisGMA-HDDA resin. When the results are examined in detail, a striking 98% decrease is observed between pure resin and resin containing 60% AF-PDMS. While this ratio is 42% between 20 wt% and 40 wt%, it is 94% between 40 wt% and 60 wt%. After 60 wt%, it was determined that there was no significant change in stress values as the amount of AF-PDMS increased.

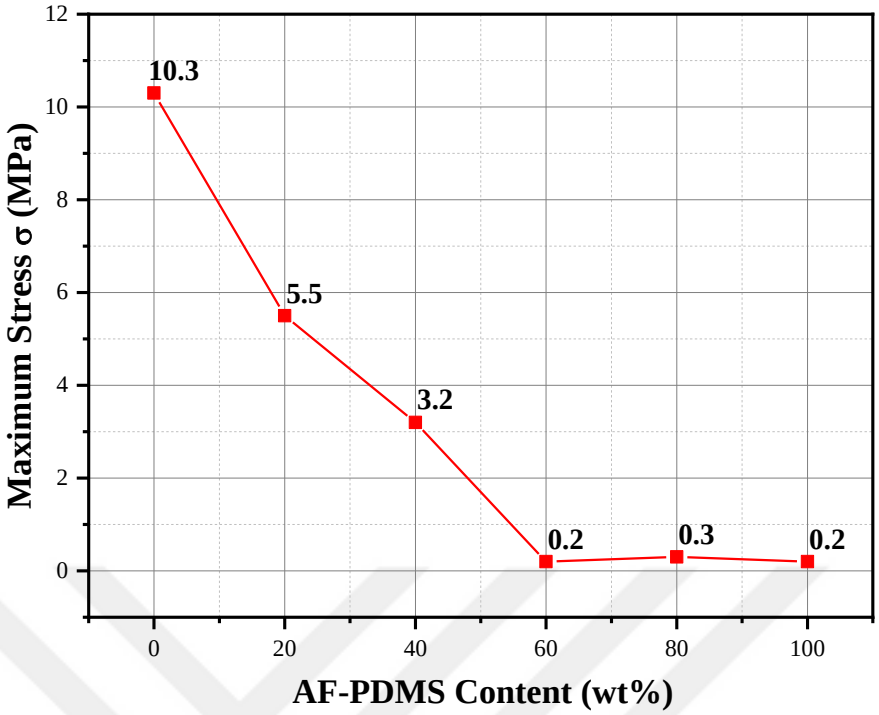


Figure 3.12 Results of the maximum stress vs AF-PDMS content

When Figure 3.13 is examined, it is seen that there is a high increase in strain values with the increasing AF-PDMS ratio. In particular, there is a very high increase like as 27233% between pure resin and pure AF-PDMS. The most striking results are the large ratio-independent differences between pure resin and AF-PDMS mixtures. Although the strain variation among the samples containing AF-PDMS was quite effective, it was obtained lower than the pure material. From 20% to 80% content, the strain value increased by an average of 100% in each AF-PDMS increment step.

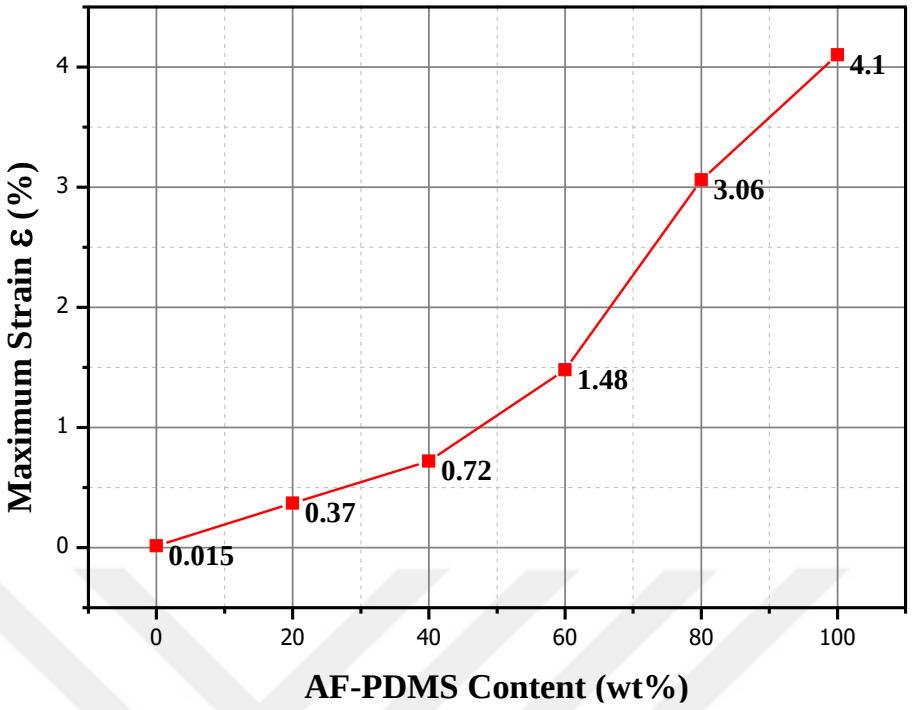


Figure 3.13 Results of the maximum strain vs AF-PDMS content

According to Young's modulus results, the value decreased as the AF-PDMS ratio in the resin increased (Figure 3.14). In other words, according to this result, it is seen that the AF-PDMS ratio increases flexibility. While the value of pure resin formed in the BisGMA/HDDA mixture was 2160 MPa, this value decreased by 99.6% to 0.816 MPa for pure AF-PDMS. While the downward trend is quite high between pure and 60% AF-PDMS content resin, it is observed that it slows down between 60% and pure AF-PDMS.

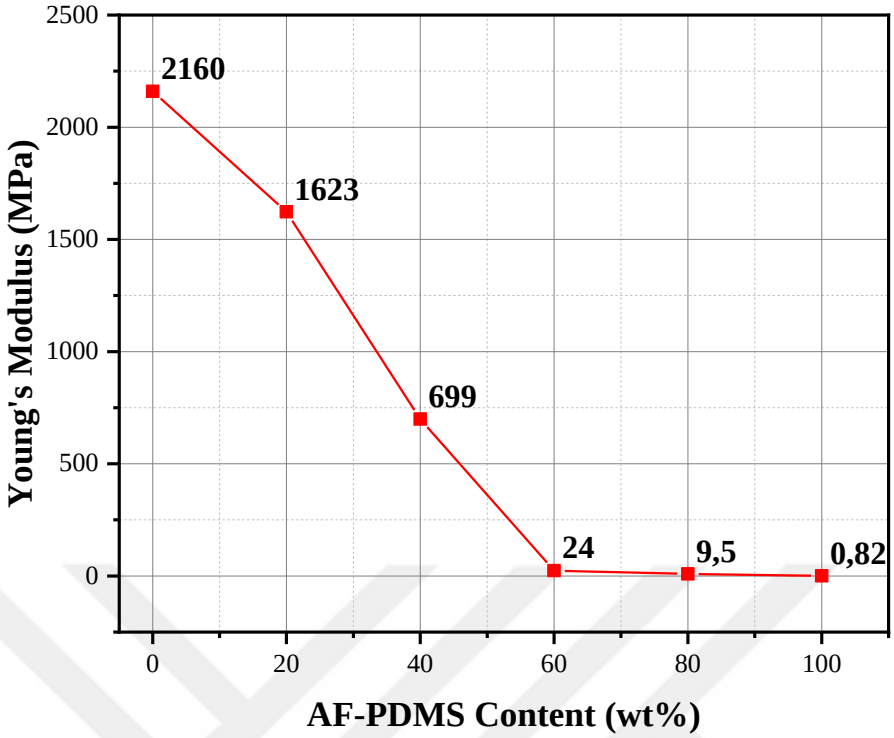


Figure 3.14 Results of the Young's Modulus vs AF-PDMS content

The equivalent of Young's Modulus results in soft tissue value ranges is given in the Figure 3.15. In this case, it was concluded that cartilage, artery, liver tissue, muscle and tendon implant production is possible between pure AF-PDMS and BisGMA. It has been demonstrated that the production of parts with the mechanical properties of the desired implant can be realized with studies carried out at certain intervals. For example, for skin implant, it is possible to achieve the required mechanical properties by changing the variation range of the wt% ratio between 40% and 60% AF-PDMS-containing mixtures.

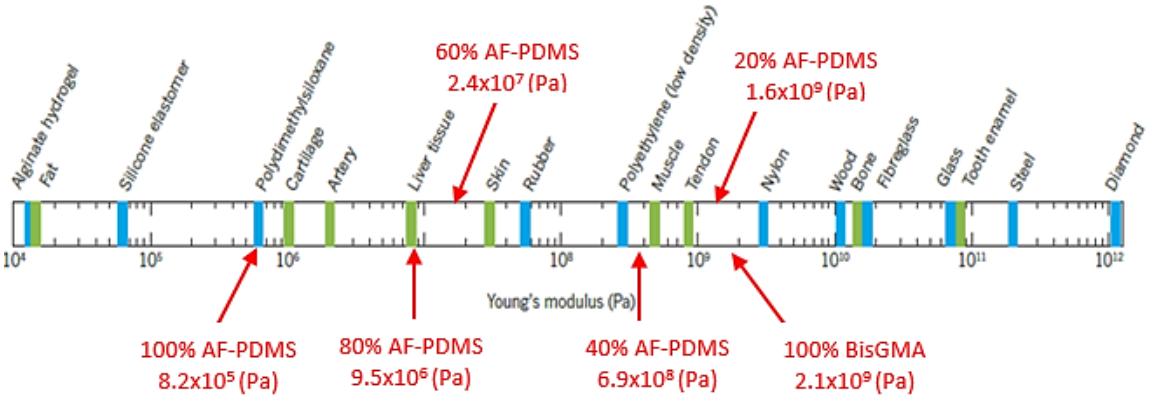


Figure 3.15 Results demonstration on approximate elastic modulus (Young's modulus) of selected engineering and biocompatible materials

3.3.2 Shore a hardness test results

When the hardness test results were examined, it was observed that Shore A values decreased significantly with increasing AF-PDMS wt% (Figure 3.16). This decrease was determined as 66% between pure resin and pure AF-PDMS. The biggest difference in the order of the decrease graph is seen as 43% between the sample containing 40% AF-PDMS and the sample containing 60% AF-PDMS.

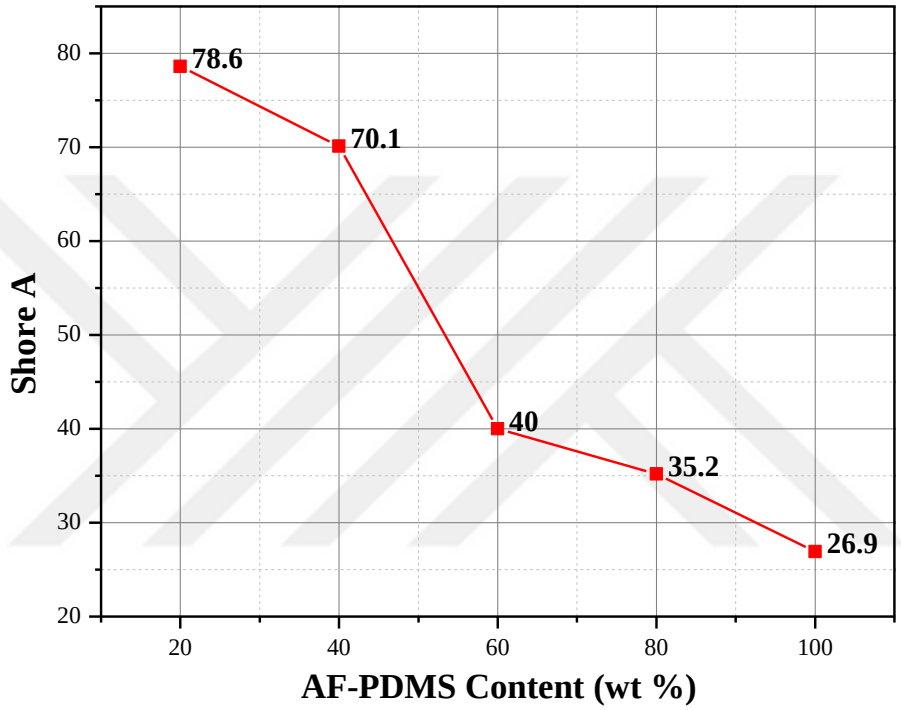


Figure 3.16 Results of the Shore A hardness test

3.3.3 Abrasion test results

The results of the abrasion tests are given in Figure 3.17. When the results are examined, it is seen that there is no remarkable change in the amount of abrasion with the increasing AF-PDMS wt% value. The decrease in weight loss value after abrasion between pure resin and 40% AF-PDMS was determined as 18%. Data could not be obtained from the samples containing 60% or more AF-PDMS, since they are quite flexible and were plastered with abrasive tool during the experiment.

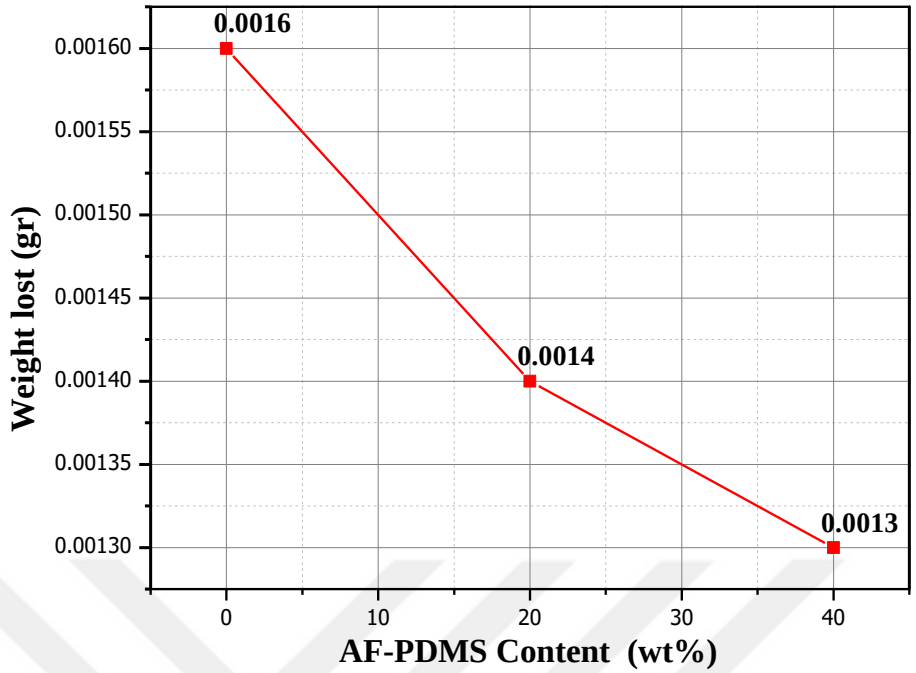


Figure 3.17 Results of the abrasion test

3.3.4 Density measurements

The results of the density measurements are given in Figure 3.18. When the graph is examined, it is seen that the density decreases with increasing AF-PDMS wt%. the decrease between pure resin and pure AF-PDMS was calculated as 20%. It was determined that the decrease in density ranged from 2% to 6% for each 20% increase in AF-PDMS. As a result, it was determined that the amount of AF-PDMS did not cause a remarkable change in the density values.

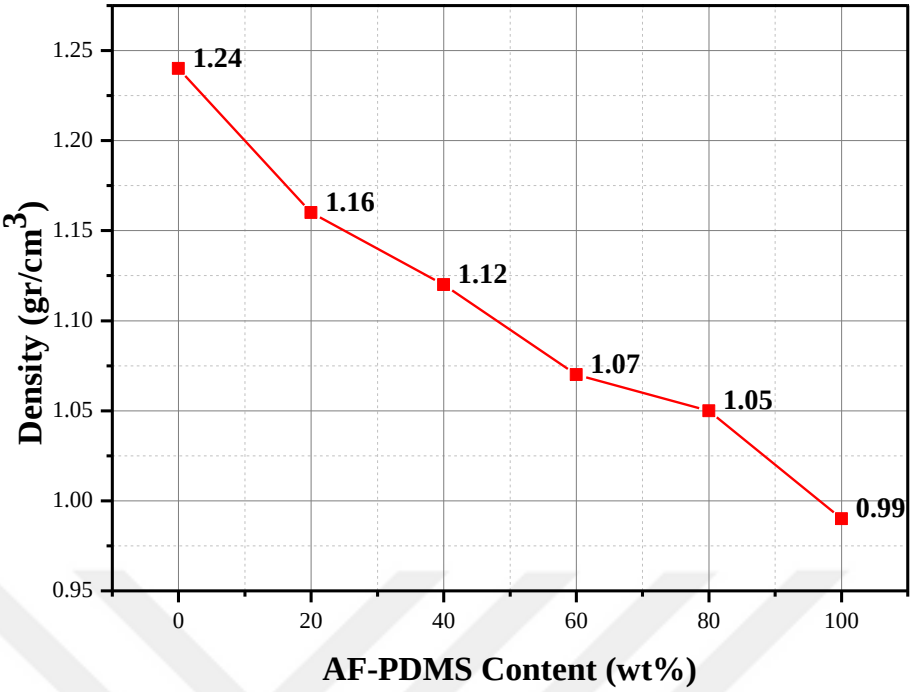


Figure 3.18 Results of the density measurements

3.3.5 Thermal characterizations

Comparison of the DSC results for 20%, 40% and 60% AF-PDMS contained specimens with pure Bis-GMA/HDDA mixture resin are given at Figure 3.19. The results shown as glassy transition temperatures are between 57 ^{0}C and 60 ^{0}C for all three of PDMS contained resins.

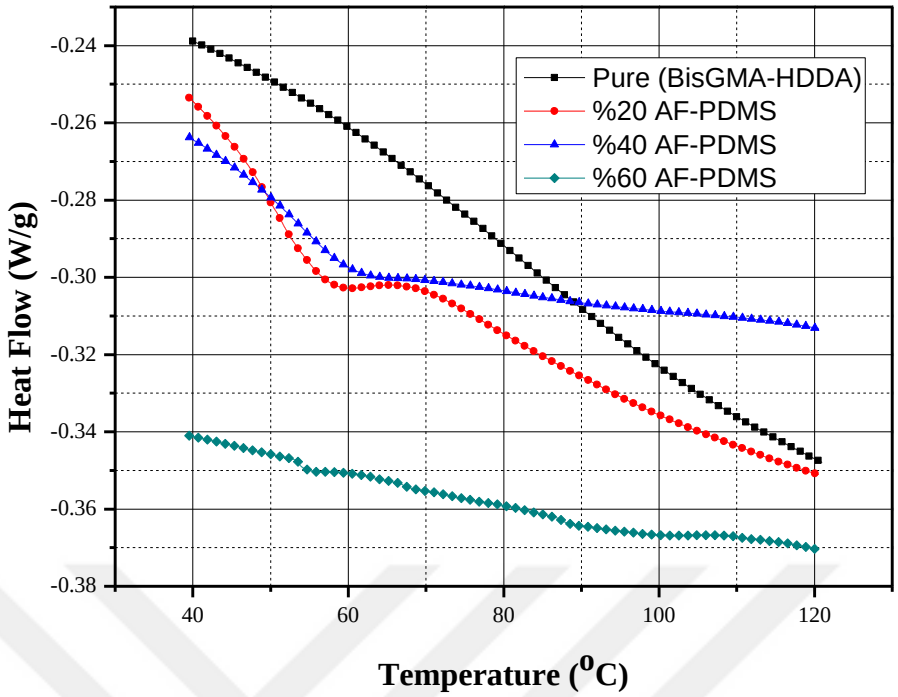


Figure 3.19 Results of the DSC test

3.3.6 FT-IR analysis

Figure 3.20 show that commercially produced acrylate functional PDMS and synthesized acrylate functional PDMS have the same FT-IR spectroscopy pattern. This result proves that AF-PDMS has been synthesized successfully.

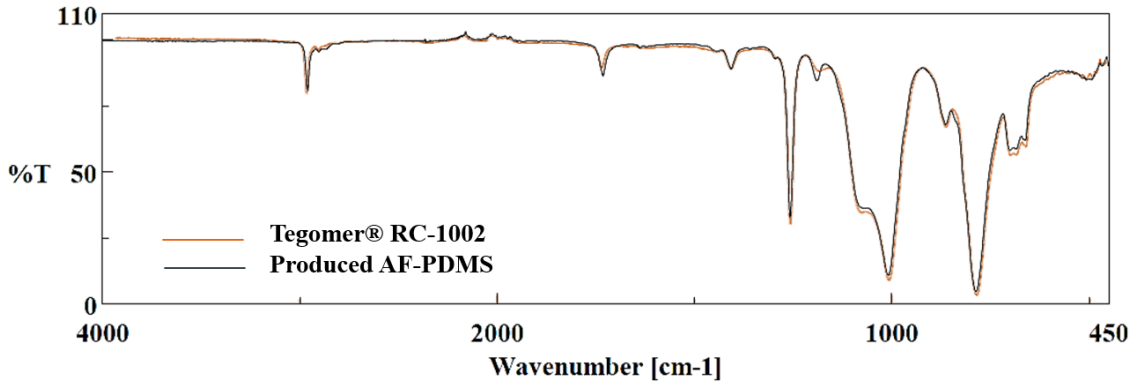


Figure 3.20 FT-IR spectroscopy for AF-PDMS vs Tegomer® RC-1002

3.4 Results of the Biocompatibility Test

As a result of the biocompatibility tests, it was determined that the samples using AF-PDMS, whose both cytotoxicity and SEM outputs were synthesized, were biocompatible.

3.4.1 Cytotoxicity test results

The cytotoxicity of the samples was evaluated by the MTT assay. Pure resin, 20% PDMS, 40% PDMS, 60% PDMS, 80% PDMS and 100% PDMS samples on the 3T3 mouse embryo fibroblasts after 3 days was investigated using indirect contact MTT assay (Figure 3.21). The cytotoxicity tests were indicated and samples have no cytotoxic effect compared to control at 72 h. It was observed that the cell viability on samples which maintained and enhanced the cell growth and viability. After 3 days, the cell growth and viability on all samples increased , respectively. There is no showed cytotoxic effects ($p < 0.05$) compared to control group (3T3).

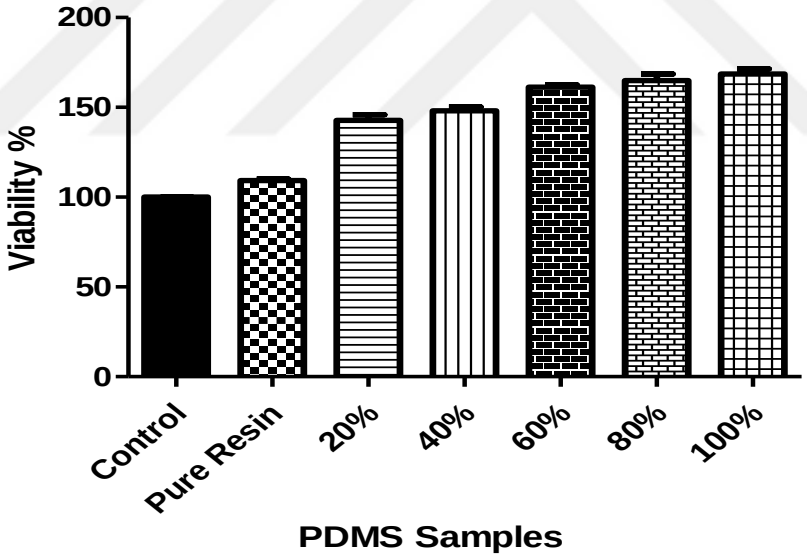


Figure 3.21 Cytotoxicity test results

3.4.2 SEM examinations of the seeded cells

SEM images taken from the sample produced with Pure BisGMA are given in the Figure 3.22. Cell groups and divisions were not observed on the sample at 1000X, which is a distant shot. In closer shots, it was determined that the cells began to adhere to the red marked regions.

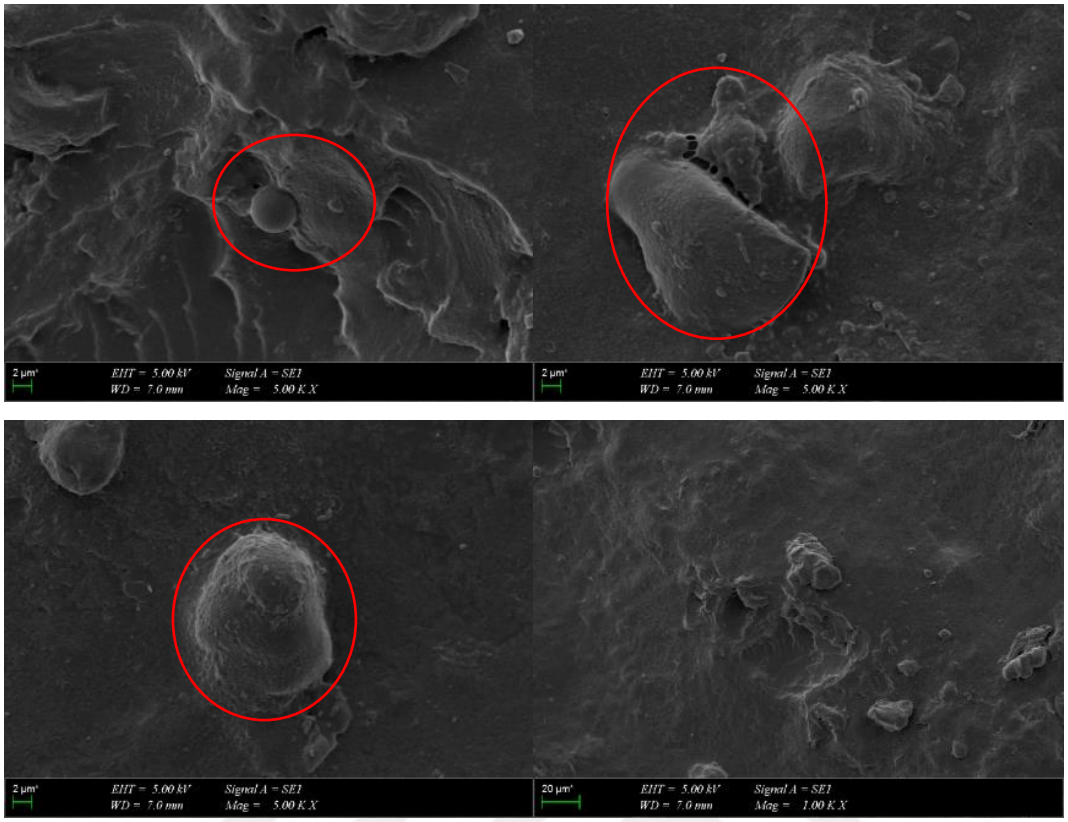


Figure 3.22 SEM images of cell seeded samples: Pure BisGMA

When Figure 3.23 is examined, low-density cell groups were detected on the surface of the piece containing 20 wt% AF-PDMS. Cells in the regions shown in the red circle increased their adhesion by embedding in the material. Although cell groups were seen in this piece, no cell division was found.

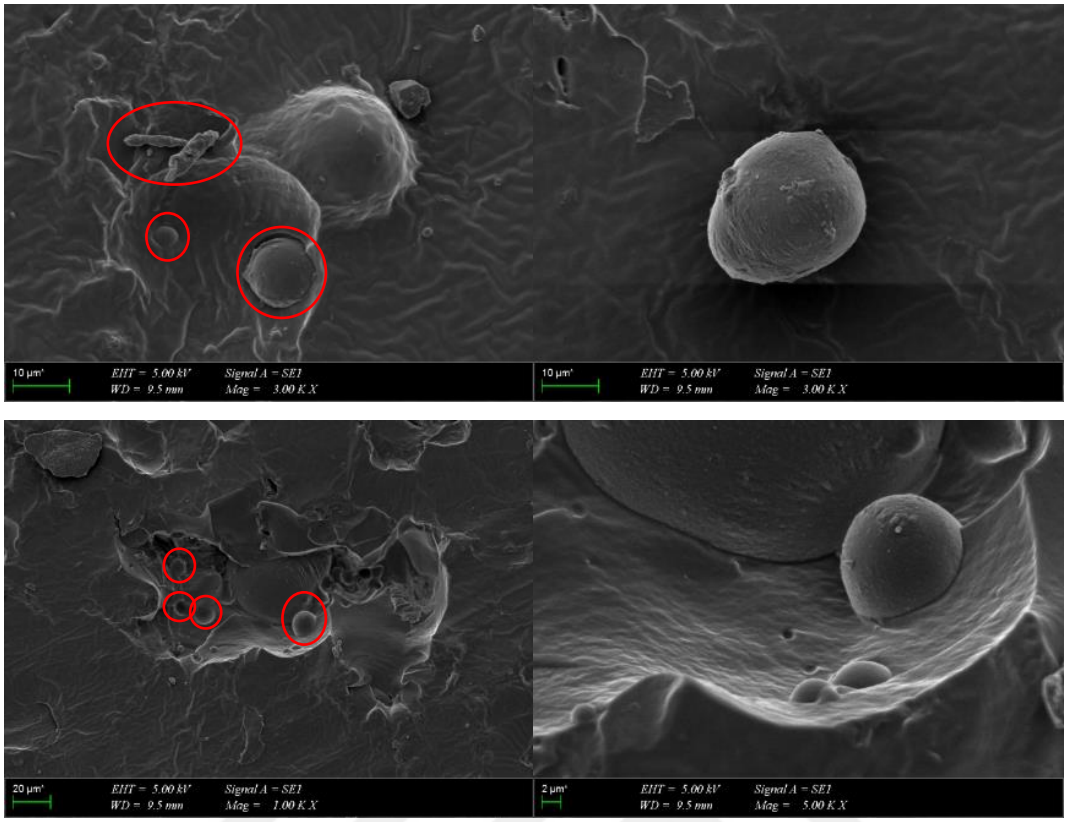


Figure 3.23 SEM images of cell seeded samples: 20 wt% AF-PDMS content

When the SEM images of the samples containing 40% wt of AF-PDMS were examined, it was determined that the amount of cells on the surface increased numerically (Figure 3.24). In the photograph obtained with high zoom-rate, it is seen that the cells are attached with their roots in the piece, as in the previous samples. In addition, the bubbles marked with a blue circle on its surface indicate that the cell has begun to divide.

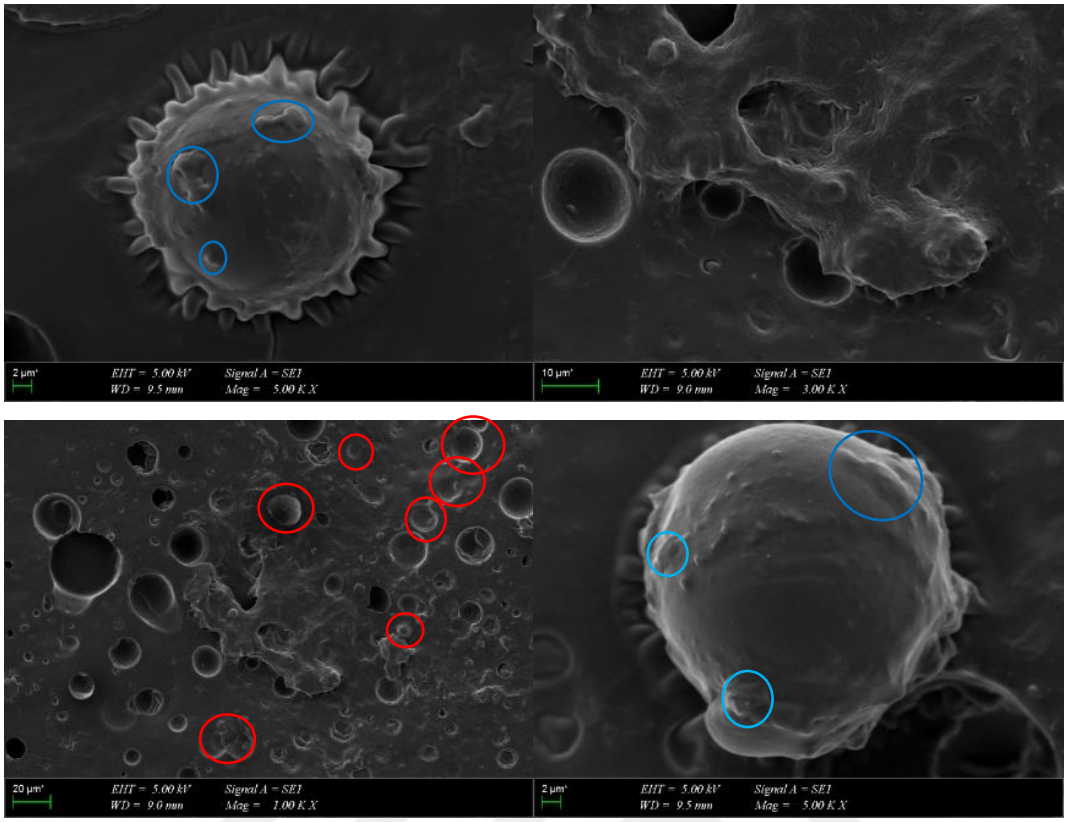


Figure 3.24 SEM images of cell seeded samples: 40 wt% AF-PDMS content

In Figure 3.25, photographs of samples containing 60 wt% AF-PDMS, taken at different zoom-rates, are given. Detected cells and cell groups are circled in red. In the image obtained with a closer shot (5000X), it was determined that cell divisions started in the parts marked with the blue ring, thanks to the bubbles on the surface. In the part marked with a green circle, a cell during division is clearly seen.

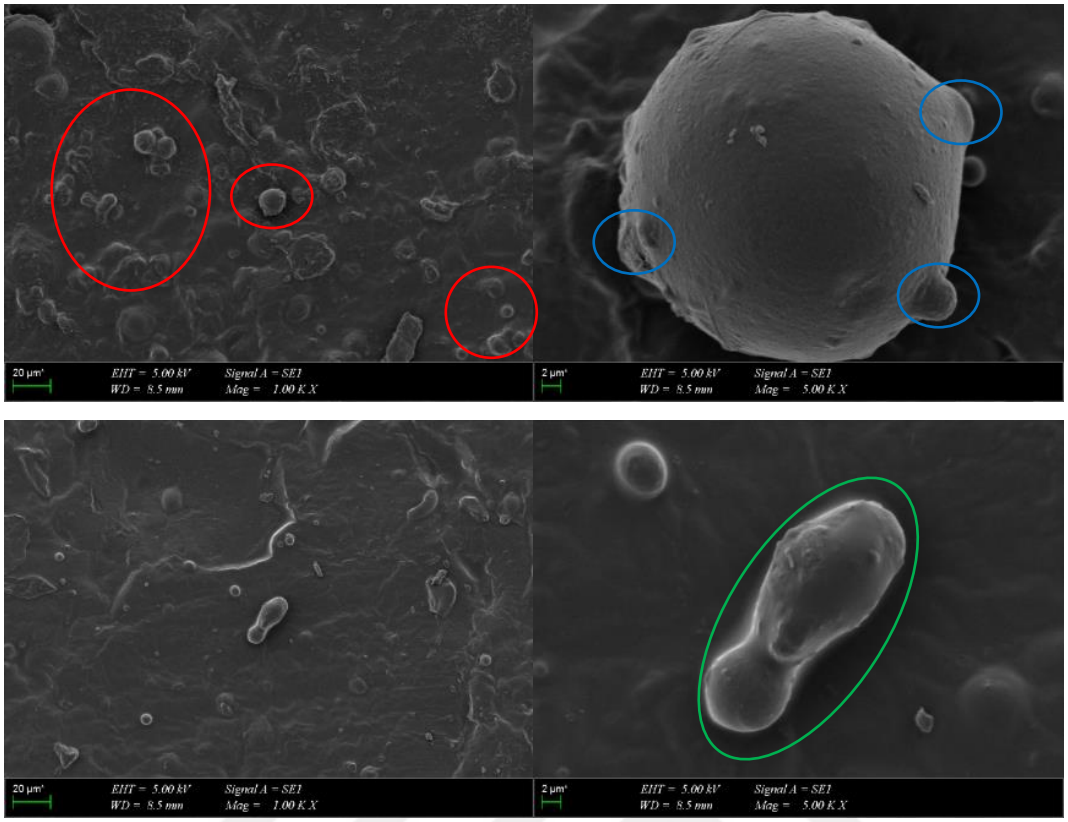


Figure 3.25 SEM images of cell seeded samples: 60 wt% AF-PDMS content

SEM images taken from samples containing 80% AF-PDMS as wt are given in Figure 3.26. In the photograph taken with 100X zoom, a high number of cell groups are seen in the regions marked with the red circle. On the other hand, it is seen that there is a very high number of dividing and proliferating cells. The cells marked with green circles were observed to be quite advanced in terms of division stage, compared to the previous samples.

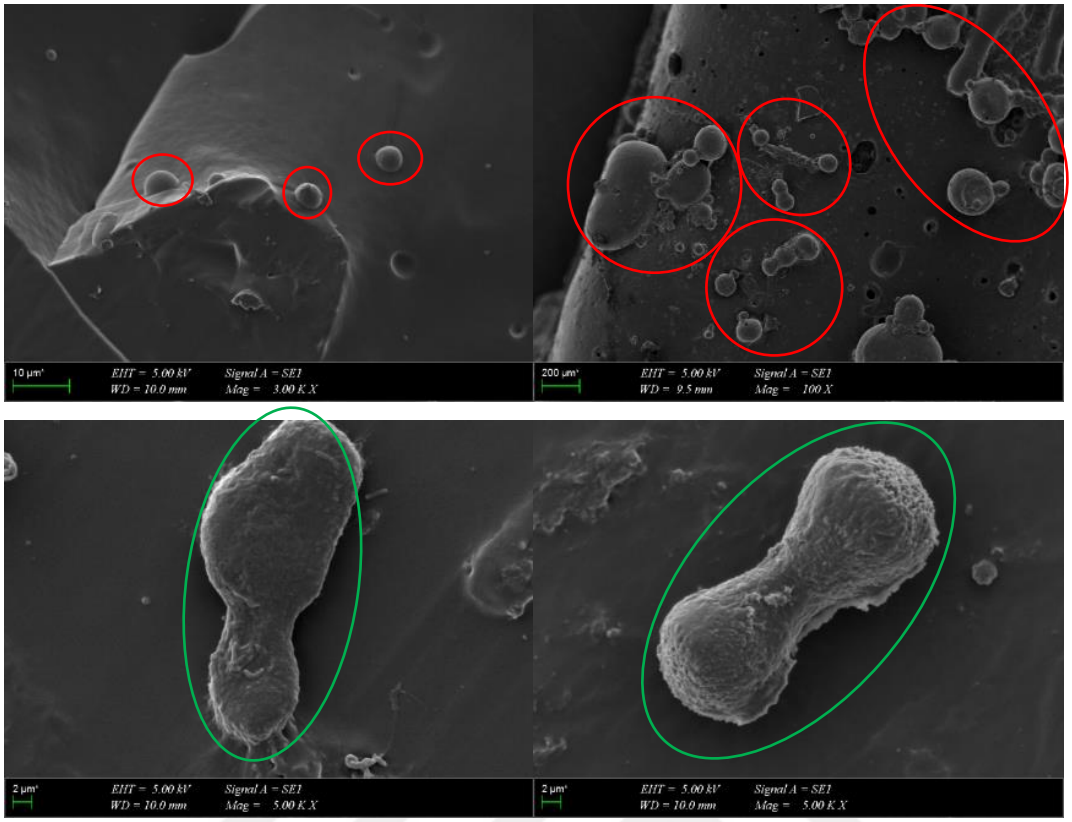


Figure 3.26 SEM images of cell seeded samples: 80 wt% AF-PDMS content

When the images of seeded cells in the samples printed with pure AF-PDMS are examined, divisions that are about to be completed together with dense cell groups are seen. It has been determined that the cells here are colonized.

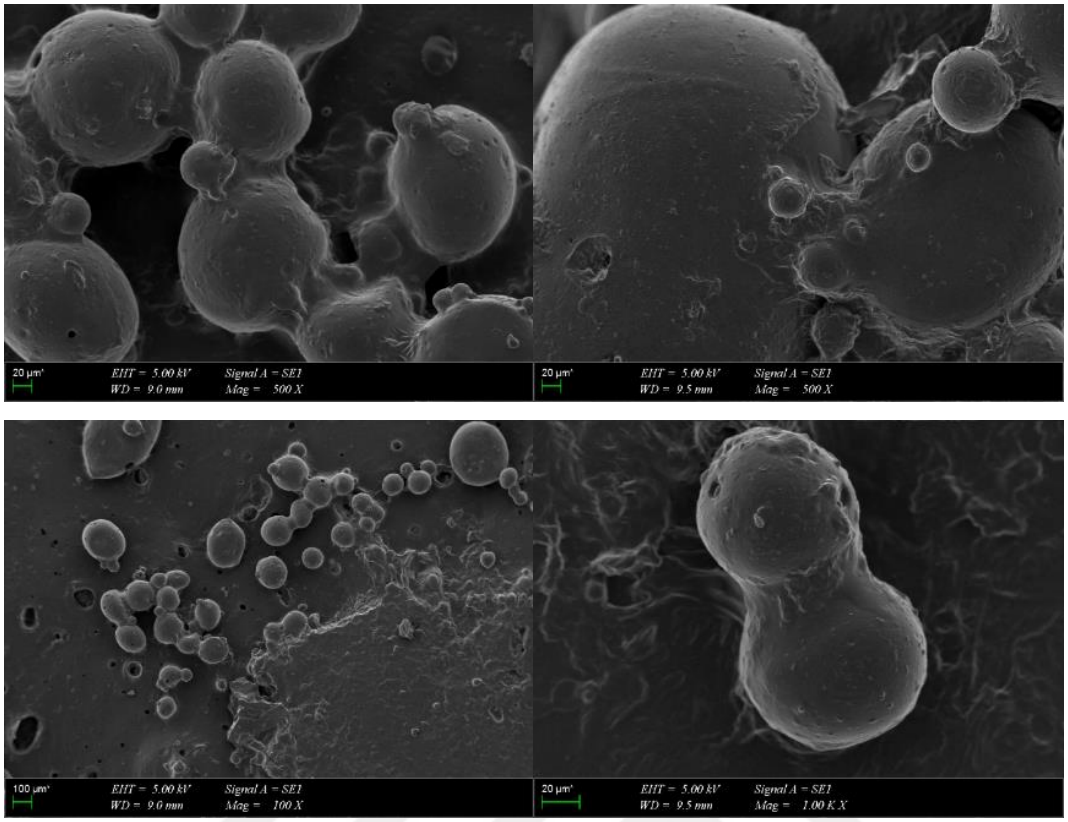


Figure 3.27 SEM images of cell seeded samples: Pure AF-PDMS

In summary, when the SEM images of all samples were evaluated, it was concluded that the cell density and division rates increased with the increasing amount of AF-PDMS.

4 CONCLUSIONS AND RECOMMENDATIONS FOR FUTURE WORKS

4.1 Conclusions

Within the scope of this study, a uniquely designed DLP printer was produced, a unique photocurable resin compatible with the UV source was synthesized, nano-composite work was carried out with this resin, biocompatible photocurable resin was produced, and flexible parts were printed. The produced printer was revised because the resins used in further studies were synthesized in low quantities and were expensive. Then, the production precision was checked by geometrical and surface roughness measurements of the printed test specimens. After verification, nano composite printing was performed and the effects of GO surface modification on mechanical and morphological properties were investigated by tensile, impact, hardness, FT-IR and SEM analyzes. In the next section, 3 different syntheses were prepared for the printing of biocompatible and flexible parts. When the resin obtained in the last experiment with AF-PDMS was compatible with the device, test samples were produced and their mechanical, morphological and thermal characterizations were examined by means of tensile hardness, abrasion, density, FT-IR and DSC tests. For biocompatibility control, cytotoxicity tests and cell seedings were performed. Cell seeded samples were examined by SEM. Obtained results are listed below:

- As a result of the geometric measurements of the samples from the first printing, the average of the percentage deviation rates in width and length was calculated as 0.47%. This ratio shows that the device produces with a very high dimensional accuracy. In the thickness measurement, a deviation of 1.75% was detected. The reason for this higher ratio is the manual determination of the starting point of the z-axis. Although this problem can be neglected when producing test samples, it can be solved by adding a switch connection to the device and assigning z home when printing parts with complex geometry.
- The average of the R_a values, obtained from the lateral surfaces, was calculated as 1.015 μm, and the average of the R_z value was calculated as 3.341 μm. The obtained results show that the surface in the production direction (z axis) is quite

smooth compared to other AM methods such as FDM and SLS. It also confirms that there is no wobbling in the z-direction during printing.

- Although the synthesized resin is suitable for part production with DLP, it was able to reduce the curing times to 5 seconds for the first three layers and to 3 seconds for the next layers. Compared to 2016 purchases, the cost of producing 1 liter of resin has been reduced to 3.78 €, using commercial raw materials and initiators.
- The tensile properties of the synthesized resin showed a remarkable improvement with the addition of sur-mod GO nanoparticles. This improvement is 39% for stress values and 153% for strain values between the pure sample and the sample produced from 0.25% sur-mod GO added resin. This improvement is also supported by the images obtained as a result of SEM analysis. On the other hand, when the impact test results were examined, a similar improvement could not be detected, and a decrease was observed in the impact resistance as the sur-mod GO wt% in the content increased. The explanation for this; While the strong bonds formed by the sur-mod GO particles with the resin under continuous loads increase the strength, the particles slide on each other and show low resistance under sudden loads due to their plate-shaped geometry.
- In addition, the above results were obtained by surface modification of GO nanoparticles. Since the unmodified particles bonded with the resin dispersedly and unevenly, a certain trend could not be obtained in the test results. As a result of the study in this section, both the mechanical properties of the DLP photocurable resin are improved by supporting it with nanoparticles and the positive effects of the surface modification applied to the GO material have been brought to the literature.
- Attempts to use Desmodure H and Krasol nn-22 materials as the main structure of biocompatible resin have been unsuccessful. The foamy and swollen structure resulting from the synthesis of Desmodure H and the high viscosity honey consistency obtained as a result of the synthesis of Krasol nn-22 could not be removed despite the removal of the components, so printing could not be performed on the DLP printer.

- The synthesis of AF-PDMS material was successfully completed and a low viscosity, epoxy-soluble and UV-curable structure was obtained. When the mechanical properties of the samples produced by adding AF-PDMS synthesis at certain wt% ratios to the epoxy resin are examined, it has been determined that AF-PDMS gives flexibility to the structure. Strain values showed a very high increase of 27233% between pure epoxy and pure AF-PDMS. An increase of approximately 100% in strain values was detected in each step wt% AF-PDMS increase from 20%. Based on these results, it has been brought to the literature that the desired flexibility for the implant to be produced can be obtained by changing the AF-PDMS ratios in the content, depending on the place of use of the implant.
- The hardness and wear test results also support the increase in flexibility. Thus, one of the aim of the study, the printing of the flexible implant material with DLP, was realized. Considering the thermal properties examined by the DSC test, the increase in the AF-PDMS ratio did not cause a change in the glass transition temperature. When the FT-IR analyzes were examined, the synthesized AF-PDMS resin had the same content as the commercial resin, and the success of the synthesis was confirmed.
- SEM results show that AF-PDMS ratio and cell numbers are directly proportional, and cell divisions progress with increasing rate. When the photographs were examined, it was determined that cell divisions started in the sample containing 60 wt% AF-PDMS, and it was almost completed in the sample printed with pure AF-PDMS, taking into account that the cells on all samples had equal incubation times. Based on these determinations, it has been brought to the literature that the synthesized AF-PDMS resin is biocompatible and increases the bioactivity of the printed parts as the wt% ratio in BisGMA increases.
- According to the results of cytotoxicity studies, the biocompatibility test demonstrated that resin and PDMS samples have suitable cytocompatibility, and can be recommended for the further development of biomedical applications.

4.2 Recommendations for future works

Based on this study, future researches are listed below:

- With the synthesized biocompatible resin, a flexible organ such as ear, nose, etc., which are scanned three-dimensionally from the human or animal body, can be modeled and produced with a DLP printer. After printing, their mechanical properties can be compared with that of the organ and modified.
- Because the material is so flexible, the modeled part can be 3D printed around a more rigid skeleton, just like the cartilage tissue in the ear and nose.
- The long-term relationship with the living tissue in the body can be examined through the implant production and the live animal integrated experiment.
- Synthesis of Desmodur H and Krasol nn-22 materials can be made suitable for printing with DLP. In this way, flexible and biocompatible products with different mechanical properties can be printed.

REFERENCES

1. Hull CW (1986) Apparatus for production of three-dimensional objects by stereolithography US Patent Specification 4575330 A

2. Crump SS (1991) Fused deposition modeling (FDM): putting rapid back into prototyping. In: The 2nd International Conference on Rapid Prototyping. Dayton, Ohio. pp 354–357

3. Vaupotič B, Brezočnik M, Balič J (2006) Use of PolyJet technology in manufacture of new product. Journal of Achievements in Materials and Manufacturing Engineering 18:4

4. Wong KV, Hernandez A (2012) A Review of Additive Manufacturing. ISRN Mechanical Engineering 2012:1–10. https://doi.org/10.5402/2012/208760

5. Flowers J (2002) Rapid Prototyping in Technology. The Technology Teacher

6. Chua CK, Chou SM, Lin SC, et al (1998) Rapid prototyping assisted surgery planning. Int J Adv Manuf Technol 14:624–630. https://doi.org/10.1007/BF01192281

7. Kruth JP (1991) Material Incress Manufacturing by Rapid Prototyping Techniques. CIRP Annals 40:603–614. https://doi.org/10.1016/S0007-8506(07)61136-6

8. Melchels FPW, Feijen J, Grijpma DW (2010) A review on stereolithography and its applications in biomedical engineering. Biomaterials 31:6121–6130. https://doi.org/10.1016/j.biomaterials.2010.04.050

9. Halloran JW, Tomeckova V, Gentry S, et al (2011) Photopolymerization of powder suspensions for shaping ceramics. Journal of the European Ceramic Society 31:2613–2619. https://doi.org/10.1016/j.jeurceramsoc.2010.12.003

10. Stansbury JW, Idacavage MJ (2016) 3D printing with polymers: Challenges among expanding options and opportunities. Dental Materials 32:54–64. https://doi.org/10.1016/j.dental.2015.09.018

11. Liska R, Schuster M, Inführ R, et al (2007) Photopolymers for rapid prototyping. J Coat Technol Res 4:505–510. https://doi.org/10.1007/s11998-007-9059-3

12. Tesavibul P, Felzmann R, Gruber S, et al (2012) Processing of 45S5 Bioglass® by lithography-based additive manufacturing. Materials Letters 74:81–84. https://doi.org/10.1016/j.matlet.2012.01.019

13. Glenn TP, Webster S, Hollaway RD (2003) Micromirror device package fabrication method

14. Sun C, Fang N, Wu DM, Zhang X (2005) Projection micro-stereolithography using digital micro-mirror dynamic mask. Sensors and Actuators A: Physical 121:113–120. https://doi.org/10.1016/j.sna.2004.12.011

15. Ligon SC, Liska R, Stampfl J, et al (2017) Polymers for 3D Printing and Customized Additive Manufacturing. Chem Rev 117:10212–10290. https://doi.org/10.1021/acs.chemrev.7b00074

16. Felzmann R, Gruber S, Mitteramskogler G, et al (2013) Advanced Engineering Materials 14: Lithography-based additive manufacturing of cellular ceramic structures. Cellular Polymers 32:174–175

17. Singh R (2011) Process capability study of polyjet printing for plastic components. Journal of Mechanical Science and Technology 4:1011–1015. https://doi.org/10.1007/s12206-011-0203-8

18. Petrovic V, Vicente Haro Gonzalez J, Jordá Ferrando O, et al (2011) Additive layered manufacturing: sectors of industrial application shown through case studies. International Journal of Production Research 49:1061–1079. https://doi.org/10.1080/00207540903479786

19. Noorani R (2006) Rapid prototyping: principles and applications. John Wiley & Sons Incorporated

20. Cooper K (2001) Rapid Prototyping Technology: Selection and Application. CRC Press, New York

21. Morvan S, Hochsmann R, Sakamoto M (2005) ProMetal RCT (TM) process for fabrication of complex sand molds and sand cores. Rapid Prototyping 11:1

22. Razavykia A, Brusa E, Delprete C, Yavari R (2020) An Overview of Additive Manufacturing Technologies—A Review to Technical Synthesis in Numerical Study of Selective Laser Melting. Materials 13:. https://doi.org/10.3390/ma13173895

23. Tang H-H, Chiu M-L, Yen H-C (2011) Slurry-based selective laser sintering of polymer-coated ceramic powders to fabricate high strength alumina parts. Journal of the European Ceramic Society 31:1383–1388. https://doi.org/10.1016/j.jeurceramsoc.2011.02.020

24. Salmoria GV, Paggi RA, Lago A, Beal VE (2011) Microstructural and mechanical characterization of PA12/MWCNTs nanocomposite manufactured by selective laser sintering. Polymer Testing 30:611–615. https://doi.org/10.1016/j.polymertesting.2011.04.007

25. Krznar M, Dolinsek S (2010) Selective Laser Sintering Of Composite Materials Technologies. Annals of DAAAM & Proceedings

26. Murr LE, Gaytan SM, Ramirez DA, et al (2012) Metal Fabrication by Additive Manufacturing Using Laser and Electron Beam Melting Technologies. Journal of

Materials Science & Technology 28:1–14. https://doi.org/10.1016/S1005-0302(12)60016-4

27. Semetay C (2007) Laser Engineered Net Shaping (LENS) modeling using welding simulation concepts. Lehigh University

28. Xiong Y (2009) Investigation of the laser engineered net shaping process for nanostructured cermets. University of California, Davis

29. Balla VK, Bose S, Bandyopadhyay A (2008) Processing of Bulk Alumina Ceramics Using Laser Engineered Net Shaping. International Journal of Applied Ceramic Technology 5:234–242. https://doi.org/10.1111/j.1744-7402.2008.02202.x

30. Liao YS, Li HC, Chiu YY (2006) Study of laminated object manufacturing with separately applied heating and pressing. Int J Adv Manuf Technol 27:703–707. https://doi.org/10.1007/s00170-004-2201-9

31. Ersoy K, Çelik B (2019) Utilization of Additive Manufacturing to Produce Tools

32. Lipke DW, Zhang Y, Liu Y, et al (2010) Near net-shape/net-dimension ZrC/W-based composites with complex geometries via rapid prototyping and Displacive Compensation of Porosity. Journal of the European Ceramic Society 30:2265–2277. https://doi.org/10.1016/j.jeurceramsoc.2010.01.011

33. Tan LJ, Zhu W, Zhou K (2020) Recent Progress on Polymer Materials for Additive Manufacturing. Adv Funct Mater 30:2003062. https://doi.org/10.1002/adfm.202003062

34. Kelly BE, Bhattacharya I, Heidari H, et al (2019) Volumetric additive manufacturing via tomographic reconstruction. Science. https://doi.org/10.1126/science.aau7114

35. Mendes-Felipe C, Oliveira J, Etxebarria I, et al (2019) State-of-the-Art and Future Challenges of UV Curable Polymer-Based Smart Materials for Printing Technologies. Advanced Materials Technologies 4:1800618. https://doi.org/10.1002/admt.201800618

36. Decker C (2001) Nguyen Thi Viet T.; Pham Thi H. Polym Int 50:986–997

37. Li L, Lee LJ (2001) Effects of inhibitors and retarders on low temperature free radical crosslinking polymerization between styrene and vinyl ester resin. Polymer Engineering & Science 41:53–65. https://doi.org/10.1002/pen.10708

38. O'Sullivan DJ (1978) Stabilized adhesive and curing compositions

39. Hull CW, Spence ST, Albert DJ, et al (1991) Methods and apparatus for production of three-dimensional objects by stereolithography

40. Zhang X, Jiang XN, Sun C (1999) Micro-stereolithography of polymeric and ceramic microstructures. Sensors and Actuators A: Physical 77:149–156. https://doi.org/10.1016/S0924-4247(99)00189-2

41. Gebhardt A (2003) New demands–new processes. In: Rapid prototyping. Carl Hanser Verlag Munich

42. Boddapati A, Rahane SB, Slopek RP, et al (2011) Gel time prediction of multifunctional acrylates using a kinetics model. Polymer 52:866–873. https://doi.org/10.1016/j.polymer.2010.12.024

43. Green WA (2010) Industrial Photoinitiators: A Technical Guide. CRC Press

44. Ficko M, Drstvenšek I, Brezočnik M, et al (2005) Prediction of total manufacturing costs for stamping tool on the basis of CAD-model of finished product. Journal of Materials Processing Technology 164–165:1327–1335. https://doi.org/10.1016/j.jmatprotec.2005.02.013

45. Leppard DG, Kohler M, Misev L (1995) Photopolymerizable compositions containing an alkylbisacylphosphine oxide

46. Fodran E, Koch M, Menon U (1996) Mechanical and Dimensional Characteristics of Fused Deposition Modeling Build Styles

47. COLLINS G, JR C (1979) Reactions Of Uv Curable Resin Formulations And Neat Multifunctional Acrylates. Ii. Photoinitiated Polymerization Of Neat 1,6-Hexanediol Diacrylate. Reactions Of Uv Curable Resin Formulations And Neat Multifunctional Acrylates Ii Photoinitiated Polymerization Of Neat 1,6-Hexanediol Diacrylate

48. Wayner DDM, Clark KB, Rauk A, et al (1997) C−H Bond Dissociation Energies of Alkyl Amines: Radical Structures and Stabilization Energies. J Am Chem Soc 119:8925–8932. https://doi.org/10.1021/ja971365v

49. Steinmann B (2006) Stereolithographic resins with high temperature and high impact resistance

50. Lee TY, Guymon CA, Jönsson ES, Hoyle CE (2004) The effect of monomer structure on oxygen inhibition of (meth)acrylates photopolymerization. Polymer 45:6155–6162. https://doi.org/10.1016/j.polymer.2004.06.060

51. Cook WD (1993) Photopolymerization kinetics of oligo(ethylene oxide) and oligo(methylene) oxide dimethacrylates. Journal of Polymer Science Part A: Polymer Chemistry 31:1053–1067. https://doi.org/10.1002/pola.1993.080310428

52. Partanen JP (1996) Solid state lasers for stereolithography. ICALEO 1996:E115–E123. https://doi.org/10.2351/1.5059069

53. Smith JM (2002) Method for creating three-dimensional objects by cross-sectional lithography

54. Ganster B, Fischer UK, Moszner N, Liska R (2008) New Photocleavable Structures. Diacylgermane-Based Photoinitiators for Visible Light Curing. Macromolecules 41:2394–2400. https://doi.org/10.1021/ma702418q

55. Murphy EJ, Ansel RE, Krajewski JJ (1990) Method of forming a three-dimensional object by stereolithography and composition therefore

56. Coats AL, Harrison JP, Hay JS, Ramos MJ (2007) Stereolithography resins and methods

57. Modrek B, Parker B, Spence ST (1992) Methods for curing partially polymerized parts

58. Steinmann B, Wolf J-P, Schulthess A, Hunziker M (1997) (Meth)acrylates containing urethane groups

59. Steinmann B, Schulthess A (1999) Liquid, radiation-curable composition, especially for stereolithography

60. Ueda M, Takase K, Kurosawa T (2015) Stereolithography resin compositions and three-dimensional objects made therefrom

61. Kim LU, Kim JW, Kim CK (2006) Effects of Molecular Structure of the Resins on the Volumetric Shrinkage and the Mechanical Strength of Dental Restorative Composites. Biomacromolecules 7:2680–2687. https://doi.org/10.1021/bm060453h

62. Hull CW, Spence ST, Lewis CW, et al (1998) Stereolithographic curl reduction

63. Moraes RR, Garcia JW, Barros MD, et al (2011) Control of polymerization shrinkage and stress in nanogel-modified monomer and composite materials. Dental Materials 27:509–519. https://doi.org/10.1016/j.dental.2011.01.006

64. Patel DK, Sakhaei AH, Layani M, et al (2017) Highly Stretchable and UV Curable Elastomers for Digital Light Processing Based 3D Printing. Advanced Materials 29:1606000. https://doi.org/10.1002/adma.201606000

65. Gul JZ, Yang B-S, Yang YJ, et al (2016) In situUV curable 3D printing of multi-material tri-legged soft bot with spider mimicked multi-step forward dynamic gait. Smart Mater Struct 25:115009. https://doi.org/10.1088/0964-1726/25/11/115009

66. Hsiao S-H, Hsu S (2018) Synthesis and Characterization of Dual Stimuli-Sensitive Biodegradable Polyurethane Soft Hydrogels for 3D Cell-Laden Bioprinting. ACS Appl Mater Interfaces 10:29273–29287. https://doi.org/10.1021/acsami.8b08362

67. Abshirini M, Charara M, Liu Y, et al (2018) 3D Printing of Highly Stretchable Strain Sensors Based on Carbon Nanotube Nanocomposites. Advanced Engineering Materials 20:1800425. https://doi.org/10.1002/adem.201800425

68. Zhao T, Yu R, Li S, et al (2019) Superstretchable and Processable Silicone Elastomers by Digital Light Processing 3D Printing. ACS Appl Mater Interfaces 11:14391–14398. https://doi.org/10.1021/acsami.9b03156

69. Abbasi F, Mirzadeh H, Katbab A-A (2001) Modification of polysiloxane polymers for biomedical applications: a review. Polymer International 50:1279–1287. https://doi.org/10.1002/pi.783

70. Perni S, Piccirillo C, Pratten J, et al (2009) The antimicrobial properties of light-activated polymers containing methylene blue and gold nanoparticles. Biomaterials 30:89–93. https://doi.org/10.1016/j.biomaterials.2008.09.020

71. Bezuidenhout D, Williams DF, Zilla P (2015) Polymeric heart valves for surgical implantation, catheter-based technologies and heart assist devices. Biomaterials 36:6–25. https://doi.org/10.1016/j.biomaterials.2014.09.013

72. Ceseracciu L, Heredia-Guerrero JA, Dante S, et al (2015) Robust and Biodegradable Elastomers Based on Corn Starch and Polydimethylsiloxane (PDMS). ACS Appl Mater Interfaces 7:3742–3753. https://doi.org/10.1021/am508515z

73. Hinton TJ, Hudson A, Pusch K, et al (2016) 3D Printing PDMS Elastomer in a Hydrophilic Support Bath via Freeform Reversible Embedding. ACS Biomater Sci Eng 2:1781–1786. https://doi.org/10.1021/acsbiomaterials.6b00170

74. Kolesky DB, Homan KA, Skylar-Scott MA, Lewis JA (2016) Three-dimensional bioprinting of thick vascularized tissues. PNAS 113:3179–3184. https://doi.org/10.1073/pnas.1521342113

75. Muth JT, Vogt DM, Truby RL, et al (2014) Embedded 3D Printing of Strain Sensors within Highly Stretchable Elastomers. Advanced Materials 26:6307–6312. https://doi.org/10.1002/adma.201400334

76. Bhagat AAS, Jothimuthu P, Papautsky I (2007) Photodefinable polydimethylsiloxane (PDMS) for rapid lab-on-a-chip prototyping. Lab Chip 7:1192–1197. https://doi.org/10.1039/B704946C

77. Sangermano M, Marchi S, Meier P, Kornmann X (2013) UV-activated hydrosilation reaction for silicone polymer crosslinking. Journal of Applied Polymer Science 128:1521–1526. https://doi.org/10.1002/app.38300

78. Martínez Rivas A, Suhard S, Mauzac M, et al (2010) Simplified and direct microchannels fabrication at wafer scale with negative and positive photopolymerizable polydimethylsiloxanes. Microfluid Nanofluid 9:439–446. https://doi.org/10.1007/s10404-009-0560-0

79. Buruiana EC, Jitaru F, Matei A, et al (2012) Influence of UV irradiation and two photon processing on the cinnamate monomers polymerization and formation of hybrid composites with nanosized ZnO. European Polymer Journal 48:1976–1987. https://doi.org/10.1016/j.eurpolymj.2012.09.012

80. Schafer KJ, Hales JM, Balu M, et al (2004) Two-photon absorption cross-sections of common photoinitiators. Journal of Photochemistry and Photobiology A: Chemistry 162:497–502. https://doi.org/10.1016/S1010-6030(03)00394-0

81. Uysal E, Çakir M, Ekici B (2021) Graphene oxide/epoxy acrylate nanocomposite production via SLA and importance of graphene oxide surface modification for mechanical properties. Rapid Prototyping Journal 27:682–691. https://doi.org/10.1108/RPJ-06-2020-0114

82. Wang X, Jiang M, Zhou Z, et al (2017) 3D printing of polymer matrix composites: A review and prospective. Composites Part B: Engineering 110:442–458. https://doi.org/10.1016/j.compositesb.2016.11.034

83. Blok LG, Longana ML, Yu H, Woods BKS (2018) An investigation into 3D printing of fibre reinforced thermoplastic composites. Additive Manufacturing 22:176–186. https://doi.org/10.1016/j.addma.2018.04.039

84. Türk D-A, Brenni F, Zogg M, Meboldt M (2017) Mechanical characterization of 3D printed polymers for fiber reinforced polymers processing. Materials & Design 118:256–265. https://doi.org/10.1016/j.matdes.2017.01.050

85. Deshmukh K, Al-Maadeed KKS andMariam ASA (2020) 3D and 4D Printing of Polymer Nanocomposite Materials

86. Badev A, Abouliatim Y, Chartier T, et al (2011) Photopolymerization kinetics of a polyether acrylate in the presence of ceramic fillers used in stereolithography. Journal of Photochemistry and Photobiology A: Chemistry 222:117–122. https://doi.org/10.1016/j.jphotochem.2011.05.010

87. Sakly A, Kenzari S, Bonina D, et al (2014) A novel quasicrystal-resin composite for stereolithography. Materials & Design (1980-2015) 56:280–285. https://doi.org/10.1016/j.matdes.2013.11.025

88. Zarek M, Layani M, Cooperstein I, et al (2016) 3D Printing of Shape Memory Polymers for Flexible Electronic Devices. Advanced Materials 28:4449–4454. https://doi.org/10.1002/adma.201503132

89. Fantino E, Chiappone A, Calignano F, et al (2016) In Situ Thermal Generation of Silver Nanoparticles in 3D Printed Polymeric Structures. Materials 9:589. https://doi.org/10.3390/ma9070589

90. Graf D, Bermejo A, Martinez L, et al (2017) Polymer-ceramic-composites for 3D inkjet printing. In: MikroSystemTechnik 2017; Congress. pp 1–4

91. Feng Z, Li Y, Xin C, et al (2019) Fabrication of Graphene-Reinforced Nanocomposites with Improved Fracture Toughness in Net Shape for Complex 3D Structures via Digital Light Processing. C 5:25. https://doi.org/10.3390/c5020025

92. O'Brien FJ (2011) Biomaterials & scaffolds for tissue engineering. Materials Today 14:88–95. https://doi.org/10.1016/S1369-7021(11)70058-X

93. Mondschein RJ, Kanitkar A, Williams CB, et al (2017) Polymer structure-property requirements for stereolithographic 3D printing of soft tissue engineering scaffolds. Biomaterials 140:170–188. https://doi.org/10.1016/j.biomaterials.2017.06.005

94. Leigh SJ, Gilbert HTJ, Barker IA, et al (2013) Fabrication of 3-Dimensional Cellular Constructs via Microstereolithography Using a Simple, Three-Component, Poly(Ethylene Glycol) Acrylate-Based System. Biomacromolecules 14:186–192. https://doi.org/10.1021/bm3015736

95. Kim SH, Yeon YK, Lee JM, et al (2018) Precisely printable and biocompatible silk fibroin bioink for digital light processing 3D printing. Nat Commun 9:1620. https://doi.org/10.1038/s41467-018-03759-y

96. Schuster M, Turecek C, Mateos A, et al (2007) Evaluation of Biocompatible Photopolymers II: Further Reactive Diluents. Monatsh Chem 138:261–268. https://doi.org/10.1007/s00706-007-0609-2

97. Chen H, Lee S-Y, Lin Y-M (2020) Synthesis and Formulation of PCL-Based Urethane Acrylates for DLP 3D Printers. Polymers 12:1500. https://doi.org/10.3390/polym12071500

98. Yoshii E (1997) Cytotoxic effects of acrylates and methacrylates: Relationships of monomer structures and cytotoxicity. Journal of Biomedical Materials Research 37:517–524. https://doi.org/10.1002/(SICI)1097-4636(19971215)37:4<517::AID-JBM10>3.0.CO;2-5

99. Popov VK, Evseev AV, Ivanov AL, et al (2004) Laser stereolithography and supercritical fluid processing for custom-designed implant fabrication. Journal of Materials Science: Materials in Medicine 15:123–128. https://doi.org/10.1023/B:JMSM.0000011812.08185.2a

100. Schuster M, Turecek C, Weigel G, et al (2009) Gelatin-based photopolymers for bone replacement materials. Journal of Polymer Science Part A: Polymer Chemistry 47:7078–7089. https://doi.org/10.1002/pola.23747

101. Schmidt M, Merklein M, Bourell D, et al (2017) CIRP annals-manufacturing technology laser based additive manufacturing in industry and academia. CIRP Ann Manuf Technol 66:561–583

102. Murphy SV, Atala A (2014) 3D bioprinting of tissues and organs. Nat Biotechnol 32:773–785. https://doi.org/10.1038/nbt.2958

103. Zhang Z, Wang B, Hui D, et al (2017) 3D bioprinting of soft materials-based regenerative vascular structures and tissues. Composites Part B: Engineering 123:279–291. https://doi.org/10.1016/j.compositesb.2017.05.011

104. Lee Y-B, Polio S, Lee W, et al (2010) Bio-printing of collagen and VEGF-releasing fibrin gel scaffolds for neural stem cell culture. Experimental Neurology 223:645–652. https://doi.org/10.1016/j.expneurol.2010.02.014

105. Kang H-W, Lee SJ, Ko IK, et al (2016) A 3D bioprinting system to produce human-scale tissue constructs with structural integrity. Nat Biotechnol 34:312–319. https://doi.org/10.1038/nbt.3413

106. Rus D, Tolley MT (2015) Design, fabrication and control of soft robots. Nature 521:467–475. https://doi.org/10.1038/nature14543

107. Beck EC, Barragan M, Tadros MH, et al (2016) Approaching the compressive modulus of articular cartilage with a decellularized cartilage-based hydrogel. Acta Biomaterialia 38:94–105. https://doi.org/10.1016/j.actbio.2016.04.019

108. Morgan EF, Unnikrisnan GU, Hussein AI (2018) Bone Mechanical Properties in Healthy and Diseased States. Annual Review of Biomedical Engineering 20:119–143. https://doi.org/10.1146/annurev-bioeng-062117-121139

109. Melchels FPW, Bertoldi K, Gabbrielli R, et al (2010) Mathematically defined tissue engineering scaffold architectures prepared by stereolithography. Biomaterials 31:6909–6916. https://doi.org/10.1016/j.biomaterials.2010.05.068

110. Melchels FPW, Grijpma DW, Feijen J (2008) Properties of porous structures prepared by stereolithography using a polylactide resin. Journal of Controlled Release 132:e71–e73. https://doi.org/10.1016/j.jconrel.2008.09.066

111. Seck TM, Melchels FPW, Feijen J, Grijpma DW (2010) Designed biodegradable hydrogel structures prepared by stereolithography using poly(ethylene glycol)/poly(d,l-lactide)-based resins. Journal of Controlled Release 148:34–41. https://doi.org/10.1016/j.jconrel.2010.07.111

112. Kim K, Dean D, Wallace J, et al (2011) The influence of stereolithographic scaffold architecture and composition on osteogenic signal expression with rat bone marrow stromal cells. Biomaterials 32:3750–3763. https://doi.org/10.1016/j.biomaterials.2011.01.016

113. Lee K-W, Wang S, Fox BC, et al (2007) Poly(propylene fumarate) Bone Tissue Engineering Scaffold Fabrication Using Stereolithography: Effects of Resin Formulations and Laser Parameters. Biomacromolecules 8:1077–1084. https://doi.org/10.1021/bm060834v

114. Luo B, Loh QL, Wong MTC, et al (2014) Bioactivated protein-based porous microcarriers for tissue engineering applications. J Mater Chem B 2:7795–7803. https://doi.org/10.1039/C4TB00846D

115. Wallace G, Wu Y, Kim J-H, et al (2008) Performance characteristics of a polypyrrole modified polydimethylsiloxane (PDMS) membrane based microfluidic pump. Faculty of Science - Papers (Archive) 239–244. https://doi.org/10.1016/j.sna.2008.07.029

116. Lin Y-H, Kang S-W, Wu T-Y (2009) Fabrication of polydimethylsiloxane (PDMS) pulsating heat pipe. Applied Thermal Engineering 29:573–580. https://doi.org/10.1016/j.applthermaleng.2008.03.028

117. Casanova-Moreno J, To J, Yang CWT, et al (2017) Fabricating devices with improved adhesion between PDMS and gold-patterned glass. Sensors and Actuators B: Chemical 246:904–909. https://doi.org/10.1016/j.snb.2017.02.109

118. Tiercelin N, Coquet P, Sauleau R, et al (2006) Polydimethylsiloxane membranes for millimeter-wave planar ultra flexible antennas. J Micromech Microeng 16:2389–2395. https://doi.org/10.1088/0960-1317/16/11/020

119. Sackmann EK, Fulton AL, Beebe DJ (2014) The present and future role of microfluidics in biomedical research. Nature 507:181–189. https://doi.org/10.1038/nature13118

120. Marcano DC, Kosynkin DV, Berlin JM, et al (2010) Improved Synthesis of Graphene Oxide. ACS Nano 4:4806–4814. https://doi.org/10.1021/nn1006368

121. Lin Y, Bilotti E, Bastiaansen CWM, Peijs T (2020) Transparent semi-crystalline polymeric materials and their nanocomposites: A review. Polymer Engineering & Science 60:2351–2376. https://doi.org/10.1002/pen.25489

122. Michelsen VB, Lygre H, Skålevik R, et al (2003) Identification of organic eluates from four polymer-based dental filling materials. European Journal of Oral Sciences 111:263–271. https://doi.org/10.1034/j.1600-0722.2003.00033.x

123. Mosmann T (1983) Rapid colorimetric assay for cellular growth and survival: Application to proliferation and cytotoxicity assays. Journal of Immunological Methods 65:55–63. https://doi.org/10.1016/0022-1759(83)90303-4

124. Wan Y-J, Tang L-C, Gong L-X, et al (2014) Grafting of epoxy chains onto graphene oxide for epoxy composites with improved mechanical and thermal properties. Carbon 69:467–480. https://doi.org/10.1016/j.carbon.2013.12.050

125. Pang JC, Li SX, Wang ZG, Zhang ZF (2013) General relation between tensile strength and fatigue strength of metallic materials. Materials Science and Engineering: A 564:331–341. https://doi.org/10.1016/j.msea.2012.11.103

126. Xiao Y, Zou H, Zhang L, et al (2020) Surface modification of silica nanoparticles by a polyoxyethylene sorbitan and silane coupling agent to prepare high-performance rubber composites. Polymer Testing 81:106195. https://doi.org/10.1016/j.polymertesting.2019.106195

127. Shuai C, Zan J, Yang Y, et al (2020) Surface modification enhances interfacial bonding in PLLA/MgO bone scaffold. Materials Science and Engineering: C 108:110486. https://doi.org/10.1016/j.msec.2019.110486

128. Feng X, Kwon S, Park JY, Salmeron M (2013) Superlubric Sliding of Graphene Nanoflakes on Graphene. ACS Nano 7:1718–1724. https://doi.org/10.1021/nn305722d

129. Çiplak Z, Yildiz N, Çalimli A (2015) Investigation of Graphene/Ag Nanocomposites Synthesis Parameters for Two Different Synthesis Methods. Fullerenes, Nanotubes and Carbon Nanostructures 23:361–370. https://doi.org/10.1080/1536383X.2014.894025

130. Jena KK, Narayan R, Alhassan SM (2017) Highly branched graphene siloxane−polyurethane-urea (PU-urea) hybrid coatings. Progress in Organic Coatings 111:343–353. https://doi.org/10.1016/j.porgcoat.2017.06.020

131. Rodriguez MaA, Liso MJ, Rubio F, et al (1999) Study of the reaction of γ – methacryloxypropyltrimethoxysilane (γ – MPS) with slate surfaces. Journal of Materials Science 34:3867–3873. https://doi.org/10.1023/A:1004666621479

132. Dukali RM, Radović IM, Stojanović DB, et al (2014) Electrospinning of laser dye Rhodamine B-doped poly(methyl methacrylate) nanofibers. Journal of the Serbian Chemical Society 79:867–880

133. ALOthman ZA (2012) Preparation and characterization of alkyl methacrylate capillary monolithic columns. Journal of Saudi Chemical Society 16:271–278. https://doi.org/10.1016/j.jscs.2011.01.010

134. Aznarte Garcia E, Qureshi AJ, Ayranci C (2018) A study on material-process interaction and optimization for VAT-photopolymerization processes. Rapid Prototyping Journal 24:1479–1485. https://doi.org/10.1108/RPJ-10-2017-0195

135. Aznarte E, Ayranci C, Qureshi AJ (2017) Digital light processing (DLP): Anisotropic tensile considerations. In: Solid Freeform Fabrication 2017: Proceedings of the 28th Annual International Solid Freeform Fabrication Symposium-An Additive Manufacturing Conference, SFF. pp 413–425

136. Lee Y-H, Lee J-B, Maeng W-Y, et al (2019) Photocurable ceramic slurry using solid camphor as novel diluent for conventional digital light processing (DLP) process. Journal of the European Ceramic Society 39:4358–4365. https://doi.org/10.1016/j.jeurceramsoc.2019.05.069

137. Lovo JFP, Camargo IL de, Erbereli R, et al (2020) Vat Photopolymerization Additive Manufacturing Resins: Analysis and Case Study. Mat Res 23:. https://doi.org/10.1590/1980-5373-MR-2020-0010

138. Wu Y-L, D'Amato AR, Yan AM, et al (2020) Three-Dimensional Printing of Poly(glycerol sebacate) Acrylate Scaffolds via Digital Light Processing. ACS Appl Bio Mater 3:7575–7588. https://doi.org/10.1021/acsabm.0c00804

139. Peterson GI, Schwartz JJ, Zhang D, et al (2016) Production of Materials with Spatially-Controlled Cross-Link Density via Vat Photopolymerization. ACS Appl Mater Interfaces 8:29037–29043. https://doi.org/10.1021/acsami.6b09768

140. Thrasher CJ, Schwartz JJ, Boydston AJ (2017) Modular Elastomer Photoresins for Digital Light Processing Additive Manufacturing. ACS Appl Mater Interfaces 9:39708–39716. https://doi.org/10.1021/acsami.7b13909

141. Monzón M, Ortega Z, Hernández A, et al (2017) Anisotropy of Photopolymer Parts Made by Digital Light Processing. Materials 10:64. https://doi.org/10.3390/ma10010064

142. He C, Ma C, Li X, et al (2020) Polymer-derived SiOC ceramic lattice with thick struts prepared by digital light processing. Additive Manufacturing 35:101366. https://doi.org/10.1016/j.addma.2020.101366

143. Wu H, Chen P, Yan C, et al (2019) Four-dimensional printing of a novel acrylate-based shape memory polymer using digital light processing. Materials & Design 171:107704. https://doi.org/10.1016/j.matdes.2019.107704

144. Lantean S, Barrera G, Pirri CF, et al (2019) 3D Printing of Magnetoresponsive Polymeric Materials with Tunable Mechanical and Magnetic Properties by Digital Light Processing. Advanced Materials Technologies 4:1900505. https://doi.org/10.1002/admt.201900505

145. Kuang X, Wu J, Chen K, et al (2019) Grayscale digital light processing 3D printing for highly functionally graded materials. Science Advances. https://doi.org/10.1126/sciadv.aav5790

146. Kim DS (Danny), Suriboot J, Shih C-C, et al (2020) Mechanical isotropy and postcure shrinkage of polydimethylsiloxane printed with digital light processing. Rapid Prototyping Journal 26:1447–1452. https://doi.org/10.1108/RPJ-10-2019-0255

147. Kowsari K, Akbari S, Wang D, et al (2018) High-Efficiency High-Resolution Multimaterial Fabrication for Digital Light Processing-Based Three-Dimensional Printing. 3D Printing and Additive Manufacturing 5:185–193. https://doi.org/10.1089/3dp.2018.0004

148. Wang M, Xie C, He R, et al (2019) Polymer-derived silicon nitride ceramics by digital light processing based additive manufacturing. Journal of the American Ceramic Society 102:5117–5126. https://doi.org/10.1111/jace.16389

149. Schmidt J, Altun AA, Schwentenwein M, Colombo P (2019) Complex mullite structures fabricated via digital light processing of a preceramic polysiloxane with active alumina fillers. Journal of the European Ceramic Society 39:1336–1343. https://doi.org/10.1016/j.jeurceramsoc.2018.11.038

150. Mu Q, Wang L, Dunn CK, et al (2017) Digital light processing 3D printing of conductive complex structures. Additive Manufacturing 18:74–83. https://doi.org/10.1016/j.addma.2017.08.011

151. Ge L, Dong L, Wang D, et al (2018) A digital light processing 3D printer for fast and high-precision fabrication of soft pneumatic actuators. Sensors and Actuators A: Physical 273:285–292. https://doi.org/10.1016/j.sna.2018.02.041

152. Liu M, Tang W, Duan W, et al (2019) Digital light processing of lunar regolith structures with high mechanical properties. Ceramics International 45:5829–5836. https://doi.org/10.1016/j.ceramint.2018.12.049

153. Dou R, Tang WZ, Wang L, et al (2019) Sintering of lunar regolith structures fabricated via digital light processing. Ceramics International 45:17210–17215. https://doi.org/10.1016/j.ceramint.2019.05.276

154. Zhang K, He R, Ding G, et al (2020) Digital light processing of 3Y-TZP strengthened ZrO2 ceramics. Materials Science and Engineering: A 774:138768. https://doi.org/10.1016/j.msea.2019.138768

155. Gonzalez G, Chiappone A, Dietliker K, et al (2020) Fabrication and Functionalization of 3D Printed Polydimethylsiloxane-Based Microfluidic Devices Obtained through Digital Light Processing. Advanced Materials Technologies 5:2000374. https://doi.org/10.1002/admt.202000374

156. Xue Y, Qi L, Niu Y, et al (2020) Integration of Electrospray and Digital Light Processing for Freeform Patterning of Porous Microstructures. Advanced Materials Technologies 5:2000578. https://doi.org/10.1002/admt.202000578

157. Lin L, Wu H, Xu Y, et al (2020) Fabrication of dense aluminum nitride ceramics via digital light processing-based stereolithography. Materials Chemistry and Physics 249:122969. https://doi.org/10.1016/j.matchemphys.2020.122969

158. Wang L, Liu X, Wang G, et al (2020) Partially stabilized zirconia moulds fabricated by stereolithographic additive manufacturing via digital light processing. Materials Science and Engineering: A 770:138537. https://doi.org/10.1016/j.msea.2019.138537

159. Kim SG, Song JE, Kim HR (2020) Development of fabrics by digital light processing three-dimensional printing technology and using a polyurethane acrylate photopolymer. Textile Research Journal 90:847–856. https://doi.org/10.1177/0040517519881821

160. Cao B, Boechler N, Boydston AJ (2018) Additive manufacturing with a flex activated mechanophore for nondestructive assessment of mechanochemical reactivity in complex object geometries. Polymer 152:4–8. https://doi.org/10.1016/j.polymer.2018.05.038

161. Shen M, Zhao W, Xing B, et al (2020) Effects of exposure time and printing angle on the curing characteristics and flexural strength of ceramic samples fabricated via digital light processing. Ceramics International 46:24379–24384. https://doi.org/10.1016/j.ceramint.2020.06.220

162. Chen Z, Liu C, Li J, et al (2019) Mechanical properties and microstructures of 3D printed bulk cordierite parts. Ceramics International 45:19257–19267. https://doi.org/10.1016/j.ceramint.2019.06.174

163. Ji Z, Zhang X, Yan C, et al (2019) 3D Printing of Photocuring Elastomers with Excellent Mechanical Strength and Resilience. Macromolecular Rapid Communications 40:1800873. https://doi.org/10.1002/marc.201800873

164. Li F, Ji X, Wu Z, et al (2020) Digital light processing 3D printing of ceramic shell for precision casting. Materials Letters 276:128037. https://doi.org/10.1016/j.matlet.2020.128037

165. Duan W, Li S, Wang G, et al (2020) Thermal conductivities and mechanical properties of AlN ceramics fabricated by three dimensional printing. Journal of the European Ceramic Society 40:3535–3540. https://doi.org/10.1016/j.jeurceramsoc.2020.04.004

166. Steyrer B, Neubauer P, Liska R, Stampfl J (2017) Visible Light Photoinitiator for 3D-Printing of Tough Methacrylate Resins. Materials 10:1445. https://doi.org/10.3390/ma10121445

167. Shen M, Qin W, Xing B, et al (2021) Mechanical properties of 3D printed ceramic cellular materials with triply periodic minimal surface architectures. Journal of the European Ceramic Society 41:1481–1489. https://doi.org/10.1016/j.jeurceramsoc.2020.09.062

168. Cortés A, Sánchez-Romate XF, Jiménez-Suárez A, et al (2020) Mechanical and Strain-Sensing Capabilities of Carbon Nanotube Reinforced Composites by Digital Light Processing 3D Printing Technology. Polymers 12:975. https://doi.org/10.3390/polym12040975

169. Zheng T, Wang W, Sun J, et al (2020) Development and evaluation of Al2O3–ZrO2 composite processed by digital light 3D printing. Ceramics International 46:8682–8688. https://doi.org/10.1016/j.ceramint.2019.12.102

170. Xiao J, Jia Y, Liu D, Cheng H (2020) Three-dimensional printing of SiCN ceramic matrix composites from preceramic polysilazane by digital light processing. Ceramics International 46:25802–25807. https://doi.org/10.1016/j.ceramint.2020.07.061

171. Li S, Zhang Y, Zhao T, et al (2020) Additive manufacturing of SiBCN/Si3N4w composites from preceramic polymers by digital light processing. RSC Adv 10:5681–5689. https://doi.org/10.1039/C9RA09598E

172. Osman RB, van der Veen AJ, Huiberts D, et al (2017) 3D-printing zirconia implants; a dream or a reality? An in-vitro study evaluating the dimensional accuracy, surface topography and mechanical properties of printed zirconia implant and discs. Journal of the Mechanical Behavior of Biomedical Materials 75:521–528. https://doi.org/10.1016/j.jmbbm.2017.08.018

173. González G, Baruffaldi D, Martinengo C, et al (2020) Materials Testing for the Development of Biocompatible Devices through Vat-Polymerization 3D Printing. Nanomaterials 10:1788. https://doi.org/10.3390/nano10091788

174. Xue D, Zhang J, Wang Y, Mei D (2019) Digital Light Processing-Based 3D Printing of Cell-Seeding Hydrogel Scaffolds with Regionally Varied Stiffness. ACS Biomater Sci Eng 5:4825–4833. https://doi.org/10.1021/acsbiomaterials.9b00696

175. Maturi M, Pulignani C, Locatelli E, et al (2020) Phosphorescent bio-based resin for digital light processing (DLP) 3D-printing. Green Chem 22:6212–6224. https://doi.org/10.1039/D0GC01983F

176. Paredes C, Martínez-Vázquez FJ, Elsayed H, et al (2021) Evaluation of direct light processing for the fabrication of bioactive ceramic scaffolds: Effect of pore/strut size on manufacturability and mechanical performance. Journal of the European Ceramic Society 41:892–900. https://doi.org/10.1016/j.jeurceramsoc.2020.09.002

177. Zeng Y, Yan Y, Yan H, et al (2018) 3D printing of hydroxyapatite scaffolds withgood mechanical and biocompatible properties by digital light processing. J Mater Sci 53:6291–6301. https://doi.org/10.1007/s10853-018-1992-2

178. Schmidt J, Elsayed H, Bernardo E, Colombo P (2018) Digital light processing of wollastonite-diopside glass-ceramic complex structures. Journal of the European Ceramic Society 38:4580–4584. https://doi.org/10.1016/j.jeurceramsoc.2018.06.004

179. Krkobabić M, Medarević D, Cvijić S, et al (2019) Hydrophilic excipients in digital light processing (DLP) printing of sustained release tablets: Impact on internal structure and drug dissolution rate. International Journal of Pharmaceutics 572:118790. https://doi.org/10.1016/j.ijpharm.2019.118790

180. Feng C, Zhang K, He R, et al (2020) Additive manufacturing of hydroxyapatite bioceramic scaffolds: Dispersion, digital light processing, sintering, mechanical properties, and biocompatibility. J Adv Ceram 9:360–373. https://doi.org/10.1007/s40145-020-0375-8

181. Wei Y, Zhao D, Cao Q, et al (2020) Stereolithography-Based Additive Manufacturing of High-Performance Osteoinductive Calcium Phosphate Ceramics by a Digital Light-Processing System. ACS Biomater Sci Eng 6:1787–1797. https://doi.org/10.1021/acsbiomaterials.9b01663

182. Elsayed H, Picicco M, Dasan A, et al (2020) Glass powders and reactive silicone binder: Application to digital light processing of bioactive glass-ceramic scaffolds. Ceramics International 46:25299–25305. https://doi.org/10.1016/j.ceramint.2020.06.323

183. Kim J-H, Maeng W-Y, Koh Y-H, Kim H-E (2020) Digital light processing of zirconia prostheses with high strength and translucency for dental applications. Ceramics International 46:28211–28218. https://doi.org/10.1016/j.ceramint.2020.07.321

184. Luo Y, Le Fer G, Dean D, Becker ML (2019) 3D Printing of Poly(propylene fumarate) Oligomers: Evaluation of Resin Viscosity, Printing Characteristics and Mechanical Properties. Biomacromolecules 20:1699–1708. https://doi.org/10.1021/acs.biomac.9b00076

185. Liu Z, Liang H, Shi T, et al (2019) Additive manufacturing of hydroxyapatite bone scaffolds via digital light processing and in vitro compatibility. Ceramics International 45:11079–11086. https://doi.org/10.1016/j.ceramint.2019.02.195

186. Bagheri Saed A, Behravesh AH, Hasannia S, et al (2020) Functionalized poly l-lactic acid synthesis and optimization of process parameters for 3D printing of porous scaffolds via digital light processing (DLP) method. Journal of Manufacturing Processes 56:550–561. https://doi.org/10.1016/j.jmapro.2020.04.076

APPENDICES

A. 1 Printed polymers via DLP process for mechanical applications

Base Material	*Additives and Reinforcements*	*Highlights*	*Improved properties*
PR-48, Autodesk Standard Clear Resin **[134]**	• Nil	• Light wavelength 405 nm • Resolution 50 µm • Layer thickness 10 µm, 25µm, 50 µm • Exposure time 1.6 s, 1.8 s, 2s	• Increase in elastic modulus up to 21.4% • Increase in ultimate tensile strength up to 301% • Increase in ultimate strain up to 347%
PR-48, Autodesk Standard Clear Resin **[135]**	• Nil	• Resolution in X and Y axis 50 µm • Resolution in Z axis 10 µm • Light wavelength 405 µm • Exposure time 1.6 s, 1.8 s, 2 s • Layer thickness 10 µm, 25µm, 50 µm	• Maximum achieved elastic modulus 0.749 ± 0.196 Gpa • Maximum achieved ultimate stress 21.7 ± 6.5 MPa • Maximum achieved ultimate strain 5.8 ± 1.87 %
SUV elastomer polymer resin **[64]**	• Photoinitiator: trimethyl benzoyl diphenyl phosphine oxide (2%) • Monomer: epoxy aliphatic acrylate (EAA) • Crosslinker: aliphatic urethane diacrylate (AUD) • Isobornyl acrylate (33% wt)	• Light Range 400-800 nm • Layer thickness 100 µm • Exposure time 10 s	• Increase in young's modulus up to 625% (0.58-4.21 MPa) • Increase in toughness from 1x106 – 50x106 j/m^3
Calcium phosphate (CaP) **[136]**	• Camphor	• Exposure time 18 s • Layer thickness 200 µm	• Flexural strength 87 ± 2.8 MPa • Reduction in viscosity 2.17 ± 0.3 mPa.s • Decrease in shrinkage up to 20.1 ± 0.61 % • Relative density up to 97.1 ± 0.02 % • Increase in compressive strength up to 233%
Commercial photocurable acrylate based resins **[137]**	• Acrylic monomers • Oligomers • Photoinitiators • Inorganic additives	• Wavelength 405 nm LED light source • Layer thickness 50 µm • Resolution in X and Y axis 62.5 µm • Resolution in Z axis 12.5 µm	• Maximum achieved tensile strength 53 MPa • Maximum achieved compressive strength 110 MPa • Maximum achieved flexural strength 79 MPa • Maximum achieved hardness 82.3 Shore D
Ebercryl 8413 (Allnex) **[138]**	• Monomers cyclic trimethylo-propane for-mal acrylate and 2(((butylamino)carbonyl)oxy) ethyl acrylate • Photoinitiator: phosphine oxide (TPO)	• Light wavelength 405 nm • Light intensity 3.68 mW/cm^2 • Layer thickness 100 µm	• Maximum achieved tensile strength 10 MPa • Maximum achieved elastic modulus 10 MPa • Maximum achieved elongation 365 %

Photoresin G+ Yellow **[139]**	• Nil	• Layer height 0.1 mm • Exposure time 12 s • Bottom exposure time 12 s • Lift speed 60 mm/min • Z retract speed 100 mm/min • Intensity range between 50 klx to200 klx	• Maximum achieved elastic modulus 63.29 MPa • Maximum achieved offset compressive strength 2.88 MPa • Maximum achieved strain-to-break 0.097 mm/mm
Bis(propylacrylamide)poly (dimethylsiloxane) **[140]**	• Photoinitiator: Irgacure 819 (0.25 wt% • Toluene (5%)	• Light intensity 80 klx • Layer cure time	• Maximum achieved elongation 472%
VisiJet® FTX Green **[141]**	Monomers: • Triethylenglycol diacrylate • Tricyclodecane dimethanol diacrylate Photoinitiator: • Phenyl oxide bis (2,4,6-trimethylbenzoyl) phosphine	• Layer thickness, 0.33 mm • Vertical build speed 14 mm/h • Average irradiance time per layer 8.3 s • Wavelength 315-400 nm	• Increase in tensile modulus up to 40% • Increase in ultimate flexural strength from 41%-77% • Maximum achieved compressive strength 3.45 MPa
Epoxy silicone resin (EPS resin, SH-023-7) (0-30 wt%) **[142]**	• Catalyst trimethylamine • Moderator: p-Methoxyphenol (MEHQ) • Additive: Hydroxyl silicone oil (HPMS) • Photoinitiator: et hyl phenyl (2,4,6-trimethylbenzoyl) phosphonate (TPOL)(1 wt%)	• Wavelength 405 nm • Layer thickness: 50 µm • Exposure time: 4 s per layer • UV light energy intensity: 3.2 mW/cm^2	• Maximum achieved compressive strength 3.45 MPa
Acrylate-based photosensitive resins **[143]**	• Photoinitiator: 2,4,6-trimethylbenzoyldiphenyl phosphine oxide (TPO) • Monomer: tert-Butyl acrylate (tBA) • Crosslinker: 1,6-hexanediol diacrylate (HDDA)	• Power density is 1250-1450 µW/cm^2 • UV light wavelength 405 nm • Layer thickness 50 µm • Exposure time 30 s	• Maximum Tg achieved at 50% wt concentration 76.3 ^{0}C • Increase in storage modulus to 59%
Urethane acrylate resin Ebercyl 8232 (Eb) **[144]**	• Fe_3O_4 nanofillers	• Layer thickness 20 µm • Exposure time 20 s • Intensity 10 mW/cm^2 • UV post-curing for 10 min	• Glass transition temperature Tg – 10.7 ^{0}C • Maximum elastic modulus 7 MPa
Bisphenol A ethoxylate diacrylate (BPADA) **[145]**	• Photoinitiator: Irgacure 819 (07.7 wt%) • Photo-absorber Sudan I (0.07 wt%) • Poly(propylene glycol) bis(2-aminopropyl ether) (7 wt%) • Glycidyl methacrylate (23 wt%) • N-butyl acrylate (8 wt%)	• Exposure time 20 s • Layer thickness 60 µm • Light resource wavelength 385 nm	• Increase in young's modulus from 1.4 MPa to 1.2 GPa • Glass transition temperature Tg rane from 14 to 68 ^{0}C
Methacrylated PDMS-macromer **[146]**	• Photoinitiator: 2,4,6-tirmethylbenzoyldi-phenylphosphinate (TPOL)	• X-Y resolution 50 µm • Layer thickness 25 µm • Exposure time 10 s • Power density 100 W/m^2 • Power level 52%	• Maximum achieved elastic modulus in Y direction 0.96 MPa • Maximum achieved elongation in Z direction 66.37%

		• Peeling speed 0.0625 mm/s	• Maximum achieved UTS in Z direction 0.49 MPa
3DM-ABS, VeroClear, VeroWhite, TangoPlus and VeroBlack **[147]**	• Nil	• Pixel size 15 µm • Light wavelength 405 nm • Layer thickness 25 µm • High-speed translational stages 400 mm/s	• Maximum achieved young's modulus by VeroBlack 129,9 MPa, by TangoPlus 0.4 MPa and by their composite 1.1 MPa
Polysilazane (PSZ) **[148]**	• Binder: Commercial acrylic resin (Formlabs INC, USA) • Photoinitator: 2,4,6-trimethylbenzoyldiphenyl phosphine oxide (3 %wt) • Initiator: snipharm Chemical Reagent	• 3D printer resolution: 25-50 µm • Layer thickness 25 µm • Exposure time 15 s • Wavelength 405 nm • Pyropolis temperature 1200, 1400 and 1600 ^{0}C	• Maximum achieved compressive strength 65.5 MPa and 5.12 MPa • Maximum achieved elastic modulus 768.5 MPa and 2.1 MPa • Linear shrinkage 27.63 % • Relative density 88.43 %
highly acrylated, liquid photocurable polysiloxane **[149]**	• dispersing agent: (0.24 wt% phosphoric acid polyester) • Photoinitiator: (Lithoz GmbH, Austria) (0.2 wt%) • Photoabsorber: azo dye (0.06 wt%)	• wavelength (455–465 nm) • layer thickness 25 µm • exposure time 6 s UV lamp (Intensity~20 mW/cm2) • Sintering temperature range 1200–1400 ◦C	• Maximum achieved compressive strength 1.8 ± 0.3 MPa • Total porosity 90 vol%
acrylic based photocurable resin (Are3d-dlp405) **[150]**	• multi-walled carbon nanotubes (MWCNTs)	• layer thickness 50 µm • exposure time 40 s • 0.3 wt% loading of MWCNT	• Increase in ultimate tensile strength up to 21% • Increase in young's modulus up to 45% • Decrease in elongation at break up to 10%
Tangoplus FLX 930(photo absorber and the resin as 3:1000) **[151]**	• Photo absorber: Rhodamine B (Acros Organics)	• Bottom-up DLP 3D printer • Resolution 50 µm • Layer thickness 87.5 µm • ultraviolet (UV) light source wavelength 385 nm • light intensity 60% of the brightness • exposure time 4 s	• Maximum achieved elongation at break 170%–220% • Increase in Maximum achieved ultimate strain up to 246%
CLRS-2, photocurable resins **[152]**	• zirconium oxide (500 g) • isopropanol (150 g) • high density polyethylene (HDPE)	• layer thickness (25 µm, 50 µm, 100 µm) • exposure time of (30 s, 60 s, 150 s) • Ultraviolet light source with pea wavelength 405 nm • sintering temperature 1150 ◦C	• Maximum achieved compressive strength (2 µm) 428.1 ± 39.7 MPa (25% enhancement) • Maximum achieved flexural strength (25 µn 129.5 ± 13.6 MPa (116% improvement)
Commercial photocurable acrylic resin (material details were confidential) was **[153]**	• lunar regolith simulant CLRS-2 (70 wt%) solid loading	• Layer thickness 50 µm • Sintering temperatures 1100 ◦C and 1150 ◦C	• Maximum achieved compressive strength 312.2 MPa • Maximum achieved flexural strength 74.1 MPa • Maximum achieved hardness 822HV

Monoclinic ZrO2 (m-ZrO2) with solid loading of 50 vol% **[154]**	• 3Y-TZP (7.5% vol) • Monomers:1,6Hexanedioldiacrylate and 1,1,1-Trimethylol propane triacrylate • Photoinitiator: TPO	• UV light (Wavelength:405 nm) • Intensity: 6000 µw/cm2 • Exposure time: 5 s	• Maximum achieved flexural strength 306.53 MPa • Linear shrinkage < 20% • Relative density 96.40%
acrylate-polydimethylsiloxane (PDMS) **[155]**	• Oligomer: TRAD (0.6 wt%) • Photoinitiator: BAPO-Si (0.6 wt%) • dyeing agent: Methacrylate group (DR1-MA) (0.1 wt%)	• light intensity 10 mW/ cm2 • UV light wavelength 405 nm • layer thickness 50 µm • exposure time 10 s	• Maximum ultimate tensile strength 1.5 MPa • Maximum achieved young's modulus 0.70 MPa
Sylgard 184 polydimethyl siloxane (PDMS) pre-polymer **[156]**	• S1813 particles	• UV dose 495 J cm-2 • Layer thickness 28 ± 3 µm	• Maximum achieved young's modulus 8.19 MPa • Maximum achieved hardness 2.81 MPa
Ceramic powders (AlN and Y2O3) **[157]**	• Dispersant: KOS110 • Sinitering additive: MgO • Photoinitiator: Phe- nylbis (2,4,6-trimethylbenzoyl) phosphine oxide • ethoxylated pentaerythritol tetraacrylate • 1,6-hexanediol diacrylate • di-functional aliphatic urethane acrylate • octanol • poly- ethylene glycol	• Layer thickness 50 µm • UV light (Wavelength: 405 nm) • exposure energy 105 mJ/ cm2	• Maximum achieved flexural strength 398 MPa • Maximum achieved hardness 10.47 GPa • Sintered density 99%
multifunctional acrylate monomers **[158]**	• Partially stabilized zirconia (PSZ) • Photoinitiator: Irgacure 819 having 2 wt% of the resin • Dispersant: amine (3 wt% of the ceramic powder)	• Layer thickness 25 µm • Exposure time 3 s • Sintering temperature 1480 ◦C • Light intensity 90 mW/ cm2 • wavelength LED light 405 nm	• Maximum achieved flexural strength 803.7 MPa • Maximum achieved young's modulus 203.4 GPa
polyurethane acrylate photopolymer **[159]**	• acrylate oligomer (10%, 20%, 30%, and 40% (v/ v))	• Exposure time (8, 10, 12,14, 16,18, and 20 s) • Optimal exposure time 14 s • Layer thickness (50, 100, and 200 mm) • Optimal layer thickness 100 mm • Optimal concentration of acrylate oligomer 10%v/ v • UV light-emitting diode (LED) (405 nm)	• Maximum tensile strength at optimal concentrations and process parameters • Maximum elongation at optimal concentrations and process parameters
2-hydroxyethyl acrylate (HEA) (98.52 wt%) **[160]**	• Photoinitiator: Irgacure 819 (0.49 wt%) • light absorbers: oxanorbornadiene-dimethacrylate (OND-DMA, 0.99 wt%), and Nile Red (0.01 wt%)	• curing time 5–11 s	• Maximum achieved strain range 156–188%

3 mol% yttrium-stabilized zirconia (3Y-TZP) suspension **[161]**	• Nil	• Sintering temperature 1550 ◦C • exposure time (2 s,3 s,4 s, 5 s, … 14 s) • layer thickness 30–120 µm • wavelength of the UV light 405 nm	• Maximum achieved flexural strength 580 MPa, at 13 s • Maximum achieved flexural strength 506 MPa, at 0 ◦
Cordierite powder (40% of slurry volume) **[162]**	• Diluent/monomer TMPTA (80% of premix volume) • Diluent/monomer HDDA (20% of premix volume) • Surfactant KH-570 (2% of slurry weight) • Dispersant disperbyk-111 (5% of slurry weight) • Photoinitiator TPO (2% of premix weight)	• particle size (D50 =7.41 µm, 3 µm and 0.35 µm) • Layer thickness (25, 50, and 200 µm) • exposure time (2 s, 3 s, and 4 s) • optimum layer thickness 50 µm • optimum exposure time= 3 s • optimum particle0.35 µm	• maximum achieved elastic modulus 90 GPa • maximum achieved hardness 6 GPa • maximum achieved compressive strength 46.3 MPa
polyethylene glycolAcryl@PEG4000 (having 33 wt% 1122TF) **[163]**	• Diluent: 2-hydroxyethyl methacrylate (HEMA) • Photoinitiator: Irgacure 819 (3%) • polymerization inhibitor Orasol dye (0.05%) • Acryl@PEG4000	• Layer thickness 108.2 µm	• Maximum achieved tensile strength 17.2 MPa • Maximum achieved residual strain 19.0% under 150% strain • Optimal elongation at break 245.0% • Maximum achieved elastic modulus 333.4 MPa • Excellent resilience (recover to 90.85% after 30 min under the 200% strain)
Shrinkagecalcined kaolin powdersolid loading of 45 vol% **[164]**	• Monomer: Polyethylene glycol diacrylate (45% vol) • Crosslinker: 3, 3-dimethylacrylic acid (8%vol) • Photoinitiator: 2,4,6-trimethylbenzoyl-diphenyl phosphate oxide (2%vol)	• layer thickness 95 µm • sintering temperature 1200 ◦C	• Maximum achieved transverse rupture strength 9.98 MPa • Maximum achieved porosity 24.5%
Photosensitive resin **[165]**	• AlN and Y2O3 powder having mass ratio of 95:5 • and solid loading of 55%vol	• sinterimg temperature from 1780 ◦C to 1845 ◦C • debinding temperature 500 ◦C • layer thickness of 25 µm	• Increase in flexural strength up to 90% • Maximum achieved bending strength 265 ± 20 MPa • Total porosity 4% • Maximum achieved thermal conductivity 155 W/(m·K)
Methacrylate Resins **[166]**	• Photoinitiators: (Ivocerin, BAPO, and TPO-L)	• layer thickness 50 µm • exposure time 40 s • light wavelength 405 nm	• maximum achieved yield strength 41 MPa (for TPO-L at 1.18 wt% concentration)
photosiensitive resin **[167]**	• Zirconia (solid loading of 50% vol)	• layer thickness 50 µm • sintering temperature 1550 C	• Maximum achieved compressive strength 105 MPa • Maximum achieved elastic modulus 5352.7 MPa (for IWP)

A. 2 Photopolymers produced by DLP printer for biomedical appliacations

Base Material	*Additice and Reinforcements*	*Highlights*	*Properties Improved*
Yttria tetragonal stabilized zirconia (Y-TZP) **[172]**	• Pigment • Al2O3 (≤ 0.1–0.4 wt%) • SiO2 (≤ 0.02 wt%) • Fe2O3 (≤ 0.01 wt%) • Na2O (≤0,06 wt%)	• layer thickness 30 µm • sintering temperature 1500 ◦C	• Maximum achieved flexural strength 943.26 MPa at 0 ◦ • Maximum achieved characteristic strength 1006.6 MPa • Obtained density 99.9% Maximum achieved tensile
glycidyl methacrylate (GMA) **[95]**	• Photoinitiator: LAP (0.2% w/v)	• Wavelength 365 nm • light intensity of 3.5 mWcm-2 • exposure time 3 s • thickness 2 mm • optimum Sil-MA hydrogel concentration 30%	• Maximum achieved compressive stress 910 KPa • Increase in compressive strain up to 80% • Increase in breaking elongation up to 124% • Increased stiffness > 4 kPa
PCL-based polyurethane acrylates m-PUA530, m-PUA800 and m-PUA1000 **[97]**	• polyethylene glycol (600) diacrylate (PEG600DA) • polypropylene glycol (PPG, Mn 450) • 3% w/w diphenyl (2,4,6-trimethylbenzoyl) phosphine oxide (TPO)	• layer thickness 50 µm • exposure time 4 s • base layer curing time 5 s • Wavelength 405 nm	Mechanical properties of pure resins m-PUA530, m-PUA800 and m-PUA1000 • Maximum achieved compressive strength of 256.52 MPa, 186.38 MPa and 127.66 MPa • Maximum achieved compressive modulus 34.43 MPa, 19.82 MPa and 16.29 MPa Mechanical properties of resins with addition of additives • Maximum compressive strength range 6.8–23.4 MPa • Maximum achieved compressive modulus 5.4–18.3 MPa
Monomers: • polyethylene glycol diacrylate • 1,6-hexanediol diacrylate • bisphenol A ethoxylate diacrylate **[173]**	• Photoinitiator: phosphine oxide-based compound (BAPO)	• LED light source wavelength (405 nm) • XY pixel resolution 50 µm • Light density of 20mW/cm^2 • Layer thickness 50 µm	• Maximum achieved dtorage modulus around 10^6 GPa
poly- (ethylene glycol) diacrylate (PEGDA) **[174]**	• Photoinitiator: lithium phenyl- 2,4,6-trimethylben- zoyiposphinate (LAP)	• exposure times (3.1, 3.5, and 3.9 s) • ultraviolet (UV) light source wavelength 405 nm • Layer thickness 50 µm • Printing resolution characterized 10 µm.	• Maximum achieved elastic modulus at different times 2950kPa, 3140kPa, and 3410 kPa • Maximum achieved ultimate stress at different times 6.7 kPa, 7.9 kPa, and 11.5 kPa • Maximum achieved compression strain 25%

Poly(1,3-propanediyl-co-glyceryl) itoconate-co-vanilatte (PPGIV) **[175]**	• bis(2-(methacryloyloxyethyl) itaconate (BHI) (24%) • tris(2-(methacryloyloxyethyl) citrate (THC) (240025) (24%) • initiators (1.5 wt%) • terminator (2.0 wt%) • dyes (0.01 wt%)	• tuneable z resolution up to 20 µm • exposure time range 3–5 s • x-y nominal printing resolution of 50 µm	• Maximum achieved tensile strength 5.4 MPa • Maximum achieved tensile modulus 61 MPa • Maximum achieved elongation at break 18% • Maximum achieved flexural modulus 350 MPa • Maximum achieved flexural strength 12.6 MPa
acrylic resin (FTD Standard Blend 3D Printing resin, Fun To Do, Alkmaar, The Netherland) **[176]**	• Commercial powders β-TCP (particle size 2.36 µm) • Pigment: (Poinsettia, Squires Kitchen)	• layer thickness 25 µm • exposure time 0.3 s • wavelength range of 400–500 nm • intensity 10 mW/cm2	• Maximum achieved compressive strength 22 ± 4 MPa
DSM's SomosO` WaterShed XC 11122 **[177]**	• Hydroxyapatite powder (10, 20, 30, 40, 45 wt%)	• Optimum concentration of HA powder 30%wt • layer height 0.05 mm	• Maximum achieved compressive strength 12.8 MPa
acrylated polymer resin (tri-propylene glycol diacrylate) resin **[178]**	• Glass: wollastonite-diopside having ~52 mol% wollastonite (CaO·SiO2) and 48 mol% diopside (CaO·MgO·2SiO2)	• exposure time 1.5 s • sintering temperature 1100 ◦C • Layer thickness 100 ụm	• Total achieved porosity 83% vol • Maximum achieved mechanical strength 3.2 MPa • Maximum observed linear shrinkage 25%
polyethylene glycol diacrylate (PEGDA) **[179]**	• Photoinitiator: diphenyl (2,4,6-trimethylbenzoyl) phosphine oxide (DPPO) • poly(ethylene glycol) 400 (PEG 400) • sodium chloride (NaCl) • mannitol	• layer thickness 0.1 mm • exposure time 100 s • blank time 1.5 s • settle time 1.5 s	• Maximum achieved tensile strength > 1.7 MPa
hydroxyapatite (HA) **[180]**	Monomer resins • 1,6-hexanediol diacrylate (HDDA • 2-hydroxyethyl methacrylate (HEMA) • trimethylolpropane triacrylate (TMPTA) Photoinitiator: • diphenyl (2,4,6-trimethyl- benzoyl) phosphine oxide (TPO) dispersant: • Solsperse 17000	• Sintering temperatureS (1200, 1250, and 1300 ℃) • Optimum concentration of • dispersant 2 wt% • Optimum solid loading 50 wt% • Optimum sinitering temperature 1250 ℃ • Wavelength 405 nm • intensity 8000 µW/cm2 • layer thickness 25 µm • exposure time 8 s	• Maximum achieved compression strength 16.9 MPa • Maximum achieved flexural strength 18.3 MPa • Shrinkage rate 15.3%
CaP powder **[181]**	• Monomer: 1,6-Hexanediol diacrylate • Photoinitiator: Phenyl bis(2,4,6-trimethylbenzoyl)- phosphine oxide • Surfactants: stearic acid, oleic acid, sebacic acid, and monoalcohol ethoxylate phosphate (MAEP)	• layer thickness 50 µm • exposure time 8 s • exposure intensity (10.14 mW/ cm2 • optimum susfactant MEAP (concentration 5.0% and 60 wt • %. solid loading)	• Increase in compressive strength up to 151% • Reduction in porosity up to 12%

acrylate resin (in form of oligomeric precursors, RF Resin – HT) **[182]**	• Non-photocurable liquid silicone (H62C) (59 wt% solid loading)	• layer thickness 50 µm • exposure time 5 s	• Maximum achieved compressive strength 2.2 MPa
Zirconia powder, Yttria-stabilized zirconia (Zpex4) **[183]**	• Monomer: 1,6-hexanediol diacrylate (HDDA) • Diluent: decalin • Dispersant: DISPERBYK180 • Photoinitiator: TPO	• UV power ~16 mW • peak wavelength ~405 nm • exposure time range (2 s - 30 s)	• Maximum achieved flexural strength 831 ± 74 MPa • high optical transmittance of 30 (± 1.2) %
Poly (propylene fumarate) (PPF) **[184]**	• Diluent: iethyl fumarate (DEF) • Photoinitiators: phenylbis (2,4,6 trimethylbenzoyl) phosphine oxide (BAPO) and Irgacure • radical scavenger: oxybenzone (HMB)	• layer thickness 50 µm • exposure time 120 s	• maximum achieved elastic modulus 199 MPa at 2.0 kDa • maximum achieved strain range 15%–25%
Hydroxyapatite (HA) **[185]**	• Dispersant: liquid sodium polyacrylate	• print speed 20 mm/s • Layer thickness 100 µm • exposure intensity 10000 µW/cm2 • exposure time 4 s	• maximum achieved compressive strength 15.25 MPa • maximum achieved compressive modulus 0.97 GPa • maximum achieved bending strength 41.3 MPa • total porosity 49.8%
Poly L-lactic acid (PLLA) having 56 wt% **[186]**	• cross- linker: 20 wt% TMPTMA • non-reactive diluent: 20 wt% N-methyl pyrrolidone (NMP) • photoinitiator: TPO (4 wt%) • orange dye	• layer thickness 50 µm • exposure time range 30–70 s • light intensity 0.8 mJ/cm2 • optimum dye concentration 0.025 wt% • optimum exposure time 70 s	• Maximum achieved compressive strength 2.2 MPa